

**Tide-induced Coastal and Estuarine Suspended Sediment
Transport and Equilibrium Morphology Formation**

Dissertation

zur Erlangung des

Doktorgrades der Naturwissenschaften

im Fachbereich Geowissenschaften

der Universität Bremen

vorgelegt von

Qian Yu

Bremen, Mai 2011

Tag des Kolloquiums:

18. Juli 2011

Gutachter:

1. Prof. Dr. Burghard W. Flemming

2. Prof. Dr. Katrin Huhn

Prüfer:

1. Prof. Dr. Dierk Hebbeln

2. Prof. Dr. Tobias Mörz

Acknowledgements

I would like to deeply thank my advisor, Prof. Dr. Burghard W. Flemming, for his continuous support, guidance and encouragement on my research presented in this dissertation. He has provided me with the freedom and means to explore the complex but charming coastal and estuarine systems. His constant enthusiasm inspired me to make greater efforts. He also told me “carry on regardless” to encourage me to pursue my dream.

I wish to thank all the staff of the Senckenberg Institute and the administrative group of the Bremen International Graduate School for Marine Sciences (GLOMAR) for their cooperation and assistance. Special acknowledgements for their help and discussions are due to Prof. Dr. Dierk Hebbeln, Dr. Alexander Bartholomä, Dr. Christian Winter, Dr. Verner B. Ernsten, Dr. Adam Kubicki, Dr. Chang Soo Son, and Dr. Li Wang. Thanks are due to the Coastal Laboratory at Nanjing University, including Prof. Dr. Shu Gao, Prof. Dr. Yaping Wang, Dr. Yang Yang, Yunwei Wang.

As I would not have been able to carry out my research without financial support, I am grateful to the Chinese Scholarship Committee (CSC) for providing a generous scholarship. Senckenberg Institute is acknowledged for providing the working space and facilities, and occasional travelling funds. GLOMAR is acknowledged for organizing lectures, seminars and providing travelling funds to attend international conferences. I would like to express my sincerest gratitude for this support.

Summary

The tide acts on coastal and estuarine systems, amongst others by inducing (1) sediment transport and, as a consequence, (2) morphological change.

In tidal environments the response of suspended sediment concentration (SSC) to the current velocity is not instantaneous, the SSC lagging behind the velocity (phase lag), and the amplitude of SSC variation decreasing with height above the bed (amplitude attenuation). In order to quantitatively describe this phenomenon, a one-dimensional (1D) vertical advection–diffusion equation of SSC is derived analytically for uniform unsteady tidal flow by defining a concentration boundary condition using a constant vertical eddy diffusivity and sediment settling velocity. The solution, in simple and straightforward terms, shows that the vertical phase lag increases linearly with the height above the bed, while the amplitude of the SSC variation decreases exponentially with the height. The lag of sediment movement or “diffusion/settling lag” is the mechanism generating the phase lag effect.

In coastal and estuarine waters, depth-averaged suspended sediment concentration (DASSC) at a fixed observation site has two sources: local resuspension and advection along a horizontal gradient. The empirical decomposition method can separate the horizontal residual suspended sediment flux (HRF) into several terms, e.g., Eulerian flux, Stokes’ drift, and tidal pumping. A simple depth-averaged 1D model is solved analytically for an observational site to explore the determinants of the forcing factors comprising residual, M2 and M4 current velocities, mean and M2 water depths, and the DASSC gradient relative to the tidal variations of DASSC and HRF. Through the solutions, the relative contributions of local resuspension and advection are clarified, the empirical decomposition terms having clear physical explanations. The solutions are applied to fit and explain the observations at a fixed station in a macro-tidal channel located along the Jiangsu Coast, China.

Tidal basins can be characterized by two major morphological elements: tidal

channels and tidal flats. Some scale-dependent empirical relations have been suggested based on observations in tidal basins of the Dutch and German coast. Thus, the channel area and volume are proportional to the 1.5 power of the basin area and tidal prism, respectively, whereas the relative channel area and the ratio between channel volume and tidal prism are both proportional to the square root of basin area. The coefficients before the power in these relations are of the order of 10^{-5} . In order to provide physical explanations for these relations, a theoretical model and a two-dimensional horizontal numerical model are developed. They result in the same type of scaling relationships and the same order of coefficients, and the morphological response of changing grain size and tidal amplitude can be successfully predicted.

Hypsometry is the distribution of volume or horizontal surface area with respect to elevation. Some observations show contradictory scale-dependent characteristics of tidal flat hypsometries in back-barrier tidal basin environments, and traditional theory explains the flattening hypsometry by relating concave-up hypsometries in low tidal range basins to the dominating influence of wind waves rather than tidal currents. In order to investigate these two problems, two series of two-dimensional depth-averaged (2DH) numerical modelling exercises were carried out. The results show that, large basin areas and low tidal ranges favour strong concave-up hypsometries, whereas small basin areas and high tidal ranges favour less concave-up hypsometries. In addition to the traditional theory, the flattening of hypsometric profile shapes can therefore also be interpreted as a response to the relative area of intertidal areas or channels in the tidal basins, and that strong concave-up hypsometries are formed which are associated with relatively large areas of low tidal flats and small areas of high tidal flats. As basins with large areas and low tidal ranges have large relative channel areas, this results in pronounced concave-up hypsometries, and vice versa.

The Qiantangjiang Estuary (the outer part being known as Hangzhou Bay) located on the east coast of China is a large funnel-shaped, tide-dominated and well-mixed estuary. The estuarine morphology is characterized by a large sand bar having a total

length of 125 km and an elevation of 10 m above the average depth of the adjacent seabed. In order to investigate the physical processes governing the formation of this morphological feature, 2DH process-based morphodynamic modeling was carried out. The model simulated a 6,000-year period, the output showing the development of a sand bar that reached equilibrium within about 3,000 years. The general shape, size and position of the modeled sand bar are consistent with the observations. A series of sensitivity analyses suggest that the estuarine convergence rate, sediment supply, and river discharge are the main controlling factors of sand bar formation. Similar to other large funnel-shaped, tide-dominated estuaries of the world, a sufficient supply of fine cohesionless sediment (derived from the adjacent Changjiang Estuary), a large river discharge, and a strong shoreline convergence rate have shaped the large sand bar in the Qiangtangjiang Estuary.

Contents

Acknowledgements	I
Summary	III
1. General Introduction	
1.1. Rationale and scope	3
1.1.1. Tide-induced suspended sediment transport.....	4
1.1.2. Tide-induced equilibrium morphology.....	6
1.2. Methods.....	8
1.2.1. Empirical modeling	9
1.2.2. Analytical modeling	9
1.2.3. Numerical modeling.....	10
1.3. Validation	11
1.4. Individual studies	12
2. Tide-induced Vertical Suspended Sediment Concentration Profiles: Phase Lag and Amplitude Attenuation	
Abstract	15
2.1. Introduction.....	15
2.2. Analytical solution	17
2.3. Validation	24
2.4. Discussion	27
2.5. Conclusions.....	29
3. Tide-induced Suspended Sediment Transport: Depth-averaged Concentrations and Horizontal Residual Fluxes	
Abstract	31
3.1. Introduction.....	31
3.2. Analytical solution	35
3.3. Observations and Applications.....	42
3.4. Discussion	49

3.4.1. Influence of advection.....	49
3.4.2. Influence of the deposition coefficient.....	51
3.4.3. Applicable scope of the solution	53
3.5. Conclusions.....	54
Appendix 3A. Interpretation of eight harmonic terms in the solution of DASSC	55
Appendix 3B. Interpretation of the terms F1 to F5 in the solution of HRF	56

4. Scale-dependent Characteristics of Equilibrium Morphology of Tidal Basins along the Dutch-German North Sea Coast

Abstract.....	59
4.1. Introduction.....	59
4.2. Study area.....	62
4.3. Empirical model.....	63
4.4. Theoretical model.....	66
4.5. Numerical model.....	70
4.5.1. Methods and Setting.....	70
4.5.2. Results.....	73
4.5.3. Sensitivity analysis.....	77
4.6. Discussion.....	78
4.6.1. Comparison of empirical, theoretical and numerical modeling results	78
4.6.2. The mechanisms of the formation of scale-dependent morphology.....	80
4.6.3. Applications to morphological changes induced by reclamation and sea level rise	82
4.7. Conclusions.....	83

5. Modelling the Equilibrium Hypsometry of Back-barrier Tidal Flats in the German Wadden Sea (southern North Sea)

Abstract.....	85
5.1. Introduction.....	86
5.2. Study area.....	88
5.3. Methods.....	89
5.3.1. Model description.....	89
5.3.2. Model setting.....	90
5.3.3. Data processing	94
5.4. Results.....	95
5.4.1. Equilibrium state examinations	95

5.4.2. Scale effects	96
5.4.3. Tidal range effect.....	99
5.5. Discussion.....	101
5.5.1. Comparison with observations	101
5.5.2. Basin scale and tidal range control on the tidal flat hypsometry.....	103
5.6. Conclusions.....	107
6. Modeling the Formation of a Sand Bar within a Large Funnel-shaped, Tide-dominated Estuary: Qiantangjiang Estuary, China	
Abstract.....	109
6.1. Introduction.....	110
6.2. Study area.....	115
6.3. Methods.....	119
6.3.1. Model description.....	119
6.3.2. Model setting.....	121
6.3.3. Sensitivity analysis.....	125
6.4. Results.....	127
6.4.1. Reference case R.....	127
6.4.2. Sensitivity analysis.....	134
6.5. Discussion	136
6.5.1. Comparison with the Qiantangjiang Estuary.....	136
6.5.2. Comparison with other numerical modeling results and other large funnel-shaped tide-dominated estuaries	139
6.5.3. The unique position of the Qiantangjiang Estuary within the general framework of estuarine morphology	143
6.6. Conclusions.....	146
7. Concluding Remarks and Perspectives	
7.1. Tide-induced suspended sediment transport	149
7.2. Tide-induced equilibrium morphology	149
References	153

There, twice in every twenty-four hours, the ocean's vast tide sweeps in a flood over a large stretch of land and hides Nature's everlasting controversy about whether this region belongs to the land or to the sea. There these wretched peoples occupy high ground, or man-made platforms constructed above the level of the highest tide they experience; they live in huts built on the site so chosen and are like sailors in ships when the waters cover the surrounding land, but when the tide has receded they are like shipwrecked victims.

Pliny the Elder (23-79)

'Naturalis historia', 16.2-3

(Translated by John Healy)

1. General Introduction

1.1. Rationale and scope

The tide rises, the tide falls. This cyclical force acts on coastal and estuarine systems, amongst others inducing (1) sediment transport and, as a consequence, (2) morphological change. This constant change has aroused the curiosity of man for thousands of years (e.g. Pliny the Elder, ca. 45 AD; Dou, ca. 762-779 AD). In modern times, this former curiosity has given way to purposeful investigation as an existential need because some 60% of humankind today lives within 50 km of the coast (Pernetta, 1994). This is putting enormous pressure on coastal systems and their natural resources and, in the context of climate change and the predicted acceleration in sea-level rise (Parry et al., 2007), the associated environmental problems are expected to increase with time. In addition, new and perhaps unforeseen problems will emerge that will require responsible action if the effects of natural hazards are to be mitigated and social disasters avoided. Responsible action, however, requires a sound understanding of the issues at hand. In a geological context, this means a thorough understanding of the physical processes governing sediment transport and resulting morphological change. The present dissertation attempts to contribute towards such understanding, in particular by the application of modern modeling techniques to unravel some hitherto unresolved issues.

Understanding the behavior of suspended sediment dynamics in tidal systems is vital for morphological, environmental and ecological reasons (Prandle, 1997; Dyer, 1997). In a morph-sedimentary context, two key issues are considered here, namely a) the manner in which suspended sediment concentration (SSC) is achieved in the water column, and b) the horizontal residual flux (HRF) of this suspended sediment. The former plays an important role in the mobilization and diffusion/advection of suspended sediment, besides also absorbing and scattering light, and hence influencing biological production (Tian et al., 2009), whereas the latter is essential in

determining the fate of the sediment and its associated contaminants (Jay et al., 1997).

Two important morphological elements are studied here: tidal basins and tide-dominated estuaries. They are of importance for economic reasons, e.g., by providing natural harbors, inland waterways, recreational areas, and land resources, but also for ecological and environmental reasons (e.g., as habitats for marine invertebrates, fish, and birds) (Reise, 2001). Due to the impacts of sea-level rise (SLR) resulting from global warming (IPCC, 2007) and of human activity (e.g. land reclamation, harbor construction), a thorough understanding of the characteristics of tidal basin morphology is essential in order to predict morphodynamic responses to these changes and to make appropriate management decisions (e.g., Flemming and Bartholomä, 1997; FitzGerald et al., 2008).

1.1.1. Tide-induced suspended sediment transport

The tide-induced behavior of suspended sediment dynamics in coastal and estuarine systems is complicated and undoubtedly three-dimensional. However, as a first step, this three-dimensional (3D) behavior can be partly represented by two kinds of one-dimensional (1D) projections: 1D vertical profiles and 1D horizontal streams.

In tide-induced vertical SSC profiles, two important features have been recognized: vertical phase lag and amplitude attenuation. Field observations have shown that the response of SSC to current velocity or bed shear stress is not instantaneous, there being a phase lag of the SSC behind the velocity (Joseph, 1954; Allen, 1974; Ellis et al. 2004; Souza et al. 2004). These observations have confirmed that this phase lag increases with height above the seabed. On the other hand, the phase-lag effect can be represented as a “hysteresis loop” by plotting SSC time-series measurements against current velocity (Davis 1977; Kostaschuk et al. 1989; West and Sangodoyin, 1991; Whitehouse 1995; van der Ham and Winterwerp 2001; van de Kreeke and Hibma 2005; Murphy and Voulgaris 2006). At the same velocities, SSCs are usually higher in decelerating currents than in accelerating currents, this being represented by a counter-clockwise loop. However, as demonstrated by Schubel (1968) and Souza et al.

(2004), not only the phase lag but also the amplitude of SSC variation decreases with height above the bed. This decreasing amplitude in SSC is known as the ‘amplitude attenuation’, in analogy to the gradual loss in the intensity of propagating signals in physics. Therefore, in order to interpret vertical SSC profiles correctly, the physical nature of these two features must be properly understood.

In horizontal area projections, SSC is generally represented by depth-averaged suspended sediment concentrations (DASSC). In regions dominated by the M2 tide and its overtide, field data analysis showed that most of the DASSC variance is at the M2 and M4 frequencies (Sternberg, 1985; van de Kreeke et al., 1997; Guezennec et al., 1999; van de Kreeke and Hibma, 2005). Weeks et al. (1993) established a conceptual model to distinguish the contributions of two potential sources of suspended sediment: localized sediment resuspension and horizontal advection. They related the former to the M4 DASSC variation, and the latter to the M2 DASSC variation. This concept has been widely used to separate the contributions of advection and resuspension from the observed SSC series (Jago and Jones, 1998; Ellis et al., 2004; Jago et al., 2006; Krivtsov et al., 2008). However, if more factors than just these act on the system, e.g., also residual and M4 tidal currents, then the problem arises as how to specify the interaction of the different forcing factors in order to evaluate their individual contributions to tidal SSC variation.

Field measurements of SSC and current velocity can be converted to suspended sediment flux. Suspended sediment flux, here called HRF, averaged over a tidal cycle can be empirically decomposed into several terms, each being related to some physical process, e.g., Eulerian flux, Stokes’ drift, tidal pumping. This decomposition method has been applied widely to study sediment flux patterns (Uncles et al., 1985a, b; Su and Wang, 1986; Uncles and Stephen, 1993; Pino Q et al., 1994; Li and Chen, 1998; Wu et al., 2001; Ganju et al., 2005). However, the precise quantitative contributions of the various forcing factors are not at all clear. For example, the tidal pumping terms are commonly represented by the phase differences between the DASSC, the depth-averaged velocity, and the tidal elevation. This approach neglects

the fact that the DASSC is also affected by other forcing factors, including residual and tidal currents, tidal elevation per se, and horizontal advection. A more comprehensive approach therefore requires a direct representation of the tidal pumping terms by all original forcing factors. As a consequence, the question remains of how to apply the physical basis of each case to the method of decomposition.

1.1.2. Tide-induced equilibrium morphology

The present study concerned itself with the equilibrium morphology of two major coastal systems: back-barrier tidal basins and large funnel-shaped, tide-dominated estuaries. The former is represented by the Wadden Sea located in the southern North Sea, the latter by the Qiangtangjiang Estuary in China, both being typical examples of their particular kind.

In the case of back-barrier tidal basins, two issues are investigated. Firstly, several scale-dependent characteristics of equilibrium morphology are interpreted. From a planimetric point of view, the most striking feature of tidal basin morphology is that it consists of two major elements, namely channels and tidal flats (van Dongeren and de Vriend, 1994), where channels are defined as the area below the mean low-water level (MLW), and tidal flats comprise the area between MLW and the mean high-water level (MHW). From a volumetric point of view, tidal basins can be characterized by two volumes, namely the channel volume and the tidal prism, the two being defined as the product of the channel area and the mean channel depth below mean sea level and as the volume of water draining from the basin at ebb tide, respectively.

It has been found that the ratio between the channel area and the basin area is proportional to the square root of the basin area (Renger and Partenscky, 1974), and that the channel volume is proportional to the 1.5 power of the tidal prism (Eysink, 1990). The coefficients before the power in these relations are of the order of 10^{-5} .

These empirical relationships raise a number of questions. Why are there power-law relations? Why are the powers 1.5 and 0.5 so prominent? And why are the values of the coefficients before the power in the order of 10^{-5} ? To answer these questions, the

physics behind the morphology must be understood.

The second focus is on the equilibrium hypsometry of back-barrier tidal flats. Hypsometry is the distribution of volume or horizontal surface area with respect to elevation. It provides a concise and quantitative method to characterize and understand the morphological characteristics of the Earth's surface (Strahler, 1952; Emery, 1979; Walcott and Summerfield, 2008). Hypsometry applied to tidal basins and tidal flats has been shown to be a sensitive morphological parameter, being not only related to hydrodynamics and morphodynamics (Boon and Byrne, 1981; Eiser and Kjerfve, 1986; Marciano et al., 2005; Toffolon and Crosato, 2007; Moore et al., 2009), but of also being useful in ecological and environmental contexts (Kirby, 2000; Oertel, 2001; Sanderson and Coade, 2010).

However, there are still some unknown aspects about tidal basin and tidal flat hypsometry. A first problem concerns scale effects. Renger and Partenscky (1974) suggested that the hypsometry of German Wadden Sea tidal basins (southern North Sea) was scale-dependent for the volume hypsometry. On the other hand, comparing two American tidal basins, Boon (1975) and Boon and Byrne (1981) suggested that area hypsometry was scale-independent. The second problem concerns the influence of tidal range. Traditional theory explains the flattening hypsometry in German Wadden Sea tidal basins by relating concave-up hypsometries in low tidal range basins to the dominating influence of wind waves rather than tidal currents (Dieckmann et al., 1987; Friedrichs and Aubrey, 1996). However, the question whether tidal processes alone could generate the observed responses of the hypsometric shapes to the tidal ranges has never been answered.

As a consequence, two problems of back-barrier tidal basin hypsometry have been investigated: (1) Is hypsometry scale-dependent or scale-independent? (2) How is basin hypsometry influenced by tidal range (mean tidal current strength)?

In the case of large funnel-shaped, tide-dominated estuaries, the question arises as to why such estuaries are commonly characterized by large longitudinal sand bars. The

Qiangtangjiang Estuary (QE) on the east coast of China is a case in point. It is characterized by a large equilibrium sand bar that forms a bulge defined by the laterally averaged longitudinal bed profile relative to the straight, uniformly sloping bed trend. Chen et al. (1964) and Chien et al. (1964) have provided a conceptual interpretation of the formation of the sand bar, but their concept has to date not been verified by more quantitative investigations of these processes in combination with the influence of associated forcing factors such as sediment supply, river discharge, and estuary shape. This problem also applies to most other large tide-dominated estuaries and, in particular, also to the generalized estuarine facies model (Dalrymple et al., 1992; Dalrymple and Choi, 2007). In addition, little work has been carried out on the quantification of how the bars scale with the different forcing factors in the various estuaries (Bhattacharya, 2003).

Therefore, the following questions may be raised in connection with the QE: Focusing on the estuarine longitudinal bed profile, (1) how can the formation process of the large sand bar in the QE be quantitatively reconstructed, and (2), in comparison with other large tide-dominated estuaries, how can the effects of estuarine convergence, sediment supply and river discharge be evaluated in terms of the generalized estuarine morphological model?

1.2. Methods

The questions outlined above have been investigated by means of empirical, analytical and numerical models. Each of these has particular advantages in helping to reveal the nature of system behavior.

Empirical models (conceptual models) are based on observations rather than on mathematical relationships, but they provide clear physical descriptions of the system concerned. On this basis, the physical appearances of the systems can be generalized and the resulting empirical relationships can be used for prediction. Although the governing processes are not revealed, they are a first essential step for further

theoretical analysis through analytical and numerical models (Kleinhans, 2010).

Analytical models are based on the direct solution of mathematical equations, which describe the system evolution. Through analytical solutions it is easy to obtain generic understandings and physical insights into the systems (Officer, 1976; Prandle, 2004). However, because of difficulties in mathematical expressions, such models can only be applied to idealized and highly simplified situations, which – to a certain degree – prevent wider implementations.

With increasing complexity, numerical models offer more information on system evolution, although they are generically not easily understood compared to analytical models (Dronkers, 2005). Due to the advantages in interpreting field observations and analyzing the sensitivity to different parameters, numerical modeling is considered to be a useful tool for the study of the sediment dynamics and morphodynamics of coastal systems (de Swart and Zimmerman, 2009).

1.2.1. Empirical modeling

The observational data from the tidal basins of the North Frisian Wadden Sea in Schleswig-Holstein (located along the northern part of the German North Sea coast) (Hofstede, 2002) were used to induce empirical scale-dependent relationships of equilibrium morphology. This issue is investigated in greater detail in Chapter 4.

1.2.2. Analytical modeling

Analytical modeling has been applied to three case studies. In Chapters 2 and 3 the 1D vertical suspended sediment advection-diffusivity equation and the 1D depth-averaged suspended sediment transport equation are solved, respectively. With certain acceptable simplifications, the solutions have relatively simple forms and can thus be easily applied to interpret available field observations. In Chapter 4, a simple analytical deduction is suggested that provides a generic understanding of the empirical scale-dependent relationships of equilibrium morphology.

1.2.3. Numerical modeling

Because of the complicated morphodynamic behavior of depositional systems, e.g., longitudinal estuarine sand bars, when analysing two-dimensional (2D) plan shapes, numerical modeling is an obvious choice. In this context a 2DH process-based morphodynamic model (Delft3D software package) was used. Delft3D has been widely applied and validated in different coastal environments to simulate longterm morphodynamic changes on different time scales (e.g., Tonnon et al., 2007; Edmonds and Slingerland, 2010; Geleynse et al., 2010), including tidal basins of the Wadden Sea region (Marciano et al., 2005; Dastgheib et al., 2008; Dissanayake et al., 2009; van der Wegen et al., 2010), and tide-dominated well-mixed estuaries (Hibma et al., 2003a; van der Wegen and Roelvink, 2008; van der Wegen et al., 2008; Xie et al., 2009).

One important advantage in longterm morphodynamic modeling is the invention of the "online" approach to save calculation time. It speeds up bed adjustments by multiplying the bed sediment flux in each time step by a morphological scaling factor (MF). This method, which was originally suggested by Roelvink (2006), was subsequently successfully applied in longterm morphological modeling using MFs typically in the order of 100 or multiples thereof. Thus, Dastgheib et al. (2008) used an MF of 300, van der Wegen and Roelvink (2008) and van der Wegen et al. (2008) an MF of 400, whereas Edmonds and Slingerland (2010) used an MF of 175.

In Chapters 4 and 5 the results of the numerical modeling of the morphological evolution of back-barrier tidal basins in the course of 60 years are presented. The results show that, within this period, a final equilibrium is approached. This is reflected in the ratio of the channel area to the basin area, in the ratio of channel volume to the tidal prism, and in the hypsometry of the tidal flats in the basins.

In the final chapter (Chapter 6), the evolution of the longitudinal sand bar in the Qiangtangjiang Estuary was investigated by numerical modeling covering a period of 6,000 years. In this case, an equilibrium sand-bar shape was attained after 3,000 years

starting from a uniformly sloping estuarine channel bed.

It is emphasized here that the geometries of the modeling domains were schematized rather than using the real geometries of the study areas. In Chapters 4 and 5 a rectangular domain to schematize the back-barrier tidal basins is used, whereas in Chapter 6 the estuarine geometry is schematized by exponentially converging shorelines. The reason for choosing schematized domains is that they are more suitable for generalized representations of the overall character of similar kinds of systems than would have been possible from a particular site-specific situation. The numerical modeling approach has been simplified to the extent that only key processes and configurations were considered from which the first-order dynamics could be extracted and anomalous and idiosyncratic situations could be identified (Paola, 2011).

1.3. Validation

Both the analytical solutions and the numerical modeling results need convincing validations based on observations. In Chapters 2 and 3 the published observational data of Souza et al. (2004) and field observations from a tidal channel along the Jiangsu coast, China, are employed respectively, to support the analytical solutions. In both cases the current velocity and SSC were measured by ADCPs (acoustic Doppler current and back-scatter profilers). In Chapter 4, which deals with the empirical model, the results from the analytical model and the numerical model were inter-compared, all having been found to converge in the same direction. The model in Chapter 5 was validated by the empirical relationships established from observations in German and Dutch Wadden Sea regions by Renger and Partensky (1974), Dieckmann (1985), Dieckmann et al. (1987) and Eysink (1993). The numerical modelling results in Chapter 6 were not only confirmed by the evolutionary history, final equilibrium morphological state, and the recent response to human activities in the QE (Chen et al., 1964; Chien et al., 1964; Guo et al., 2009), but also in comparison with other

numerical modeling results on the same system (Todeschini et al., 2008) and on other large funnel-shaped tide-dominated estuaries (Amos, 1978; Harris, 1988; Dalrymple et al., 1990; Chauhan et al., 2006; Ramaswamy et al., 2007).

1.4. Individual studies

The main results of the study are presented in five manuscripts that are reproduced below in the form of individual chapters.

Chapter 2: Yu, Q., Flemming, B.W., Gao, S..

Tide-induced vertical suspended sediment concentration profiles: phase lag and amplitude attenuation.

(published in Ocean Dynamics, doi: 10.1007/s10236-010-0335-x)

A one-dimensional vertical advection–diffusion equation of SSC is derived analytically for uniform unsteady tidal flow by defining a concentration boundary condition using a constant vertical eddy diffusivity and sediment settling velocity. The solution, in simple and straightforward terms, shows that the vertical phase lag increases linearly with height above the bed, whereas the amplitude of the SSC variation decreases exponentially with height.

Chapter 3: Yu, Q., Wang, Y., Flemming, B.W., Gao, S..

Tide-induced suspended sediment transport: depth-averaged concentrations and horizontal residual fluxes.

(submitted to Continental Shelf Research)

A simple depth-averaged 1D model is solved analytically for a particular point to explore the effect of the forcing factors of residual, M2 and M4 current velocities, mean and M2 water depth, and DASSC gradient on the tidal variations of DASSC and

HRF. Through the solutions, the relative contributions of local resuspension and advection on DASSC are clarified, and the empirical decomposition terms of HRF are shown to have clear physical explanations.

Chapter 4: Yu, Q., Wang, Y., Flemming, B.W., Gao, S..

Scale-dependent Characteristics of Equilibrium Morphology of Tidal Basins along the Dutch-German North Sea Coast.

(submitted to the Journal of Geophysical Research)

The scale-dependent relationships between channel area and basin area, and between channel volume and tidal prism are investigated by means of empirical, theoretical (analytical), and numerical models. The results illustrate that the relations all follow similar power law relationships. The morphological response of changing grain size and tidal amplitude is successfully predicted by the theoretical model.

Chapter 5: Yu, Q., Wang, Y., Flemming, B.W., Gao, S..

Modelling the Equilibrium Hypsometry of Back-barrier Tidal Flats in the German Wadden Sea (southern North Sea).

(published in Continental Shelf Research, doi: 10.1016/j.csr.2011.05.011)

Two series of numerical modeling exercises were carried out using schematized rectangular back-barrier tidal basins roughly corresponding to the tidal basins found in the German Wadden Sea. The results show that, in the equilibrium states of tidal basins, large basin areas and low tidal ranges favor strong concave-up hypsometries, whereas small basin areas and high tidal ranges favor less concave-up hypsometries. This is interpreted to be a response to the relative area of intertidal areas or channels in the tidal basins.

Chapter 6: Yu, Q., Wang, Y., Gao, S., Flemming, B.W..

Modeling the formation of a sand bar within a large funnel-shaped, tide-dominated estuary: Qiantangjiang estuary, China.

(submitted to Marine Geology)

2DH process-based morphodynamic modeling (Delft3D) was carried out for a 6,000-year period on a schematized funnel-shaped domain based on the dimensions of the Qiantangjiang Estuary. The output shows the development of a sand bar that reaches equilibrium within about 3,000 years, its general shape, size and position being consistent with observations. A series of sensitivity analyses suggest that the estuarine convergence rate, sediment supply, and river discharge are the main controlling factors of sand bar formation.

2. Tide-induced Vertical Suspended Sediment Concentration Profiles: Phase Lag and Amplitude Attenuation

Abstract

In tidal environments the response of suspended sediment concentration (SSC) to the current velocity is not instantaneous, the SSC lagging behind the velocity (phase lag), and the amplitude of SSC variation decreasing with height above the bed (amplitude attenuation). In order to quantitatively describe this phenomenon, a one-dimensional vertical advection–diffusion equation of SSC is derived analytically for uniform unsteady tidal flow by defining a concentration boundary condition using a constant vertical eddy diffusivity and sediment settling velocity. The solution, in simple and straightforward terms, shows that the vertical phase lag increases linearly with the height above the bed, while the amplitude of the SSC variation decreases exponentially with the height. The relationship between the SSC and the normalized current velocity can be represented by an ellipse or a line, depending on the phase lag. The lag of sediment movement or “diffusion/settling lag” is the mechanism generating the phase lag effect. Field observations used for validation show that the theoretically predicted and the observed curves of the vertical SSC phase lag and amplitude attenuation show reasonable agreement. The procedure proposed in this paper substantially simplifies the modeling of suspended matter transport in tidal flows.

2.1. Introduction

Tidal systems have, amongst others, been investigated with respect to their suspended sediment dynamics and budgets because these play important roles in morphologic change, contaminant transport, and biogeochemical processes. From field observations it has long been known that, in tidal environments, the response of suspended sediment concentration (SSC) to the current velocity, or the bed shear

stress, is not instantaneous, and that there is a phase lag of the SSC behind the velocity (for a summary of observations before the 1970s cf. Allen (1974)). These observations have confirmed that the lag increases with height above the seabed (Joseph, 1954; Ellis et al. 2004; Souza et al. 2004). For example, measurements in the southern North Sea off the isle of Texel (Joseph 1954) recorded time lags of between 0 (near the bottom) and 3 hours (near the surface). On the other hand, this phase lag effect can be represented as a “hysteresis loop” by plotting SSC time-series measurements against current velocity (Davis 1977; Kostaschuk et al. 1989; West and Sangodoyin, 1991; Whitehouse 1995; van der Ham and Winterwerp 2001; van de Kreeke and Hibma 2005; Murphy and Voulgaris 2006). At the same velocities, SSCs are usually higher in decelerating currents than in accelerating currents, this being represented by an anticlockwise loop. However, as demonstrated by Schubel (1968) and Souza et al. (2004), not only the phase difference but also the amplitude of the SSC variation decreases with height above the bed. In the present contribution, we call the decreasing amplitude in SSC the ‘amplitude attenuation’, in analogy to the definition of the gradual loss in the intensity of propagating signals in physics.

The quantitative interpretation of the phase lag of SSC behind velocity, and the amplitude attenuation of SSC variation, is based on the evolution of vertical SSC profiles. These represent a balance between upward turbulent diffusion and downward settling of sediment particles. Because in uniform and steady flow conditions the duration of these two processes can be estimated by h^2/K_s and h/W_s , respectively, the relative importance of these two discrete processes of dispersion and settlement can be scaled by $W_s h/K_s$, including the sediment vertical eddy diffusivity K_s and the sediment setting velocity W_s , and also the water depth h (Prandle 1997). The classic formulation introduced by Rouse (1937) for uniform and steady flow conditions is:

$$\frac{C_z}{C_a} = \left(\frac{h-z}{z} \frac{a}{h-a} \right)^{W_s / \beta \kappa u_*} \quad (2.1)$$

where C_z is the SSC at height z relative to that of C_a at the reference height a .

However, in the case of reversing unsteady tidal flows, the application of the Rouse formulation is questionable. Because of their inherent complexity, tidal SSC profiles are generally estimated using a variety of numerical approaches (e.g., Wang et al. 2005; Stanev et al. 2007; van der Molen et al. 2009). In some cases, analytical solutions for uniform unsteady flows were achieved by using advanced mathematical tools (Davis 1977; Smith 1977; Lavelle et al. 1984; Prandle 1997; Jung et al. 2004), but these are relatively complex and hence difficult to implement in practice.

With the development of new field observation instrumentation, especially the application of ADCPs (acoustic Doppler current and back-scatter profilers), the continuous measurement of vertical SSC profiles has become the state of the art (e.g., Holdaway et al. 1999; Souza et al. 2004). As a consequence, excellent SSC data are today available for the investigation of phase lag and the amplitude attenuation phenomena in coastal SSC profiles. However, several key parameters, e.g., the sediment settling velocity and the amplitude calibration from the ADCP back-scatter to real SSC, are still uncertain (e.g., Bartholomä et al. 2009).

In the present paper, tide-induced vertical SSC profiles were derived analytically for uniform unsteady flow by defining a concentration boundary condition (Dirichlet boundary condition; cf. Sanford and Halka 1993) in order to obtain a simpler and more straightforward solution and to allow the phase lag and amplitude attenuation to be quantitatively expressed in simple formulae. After validating the results on the basis of the data of Souza et al. (2004), the mechanism, limitations and applications of the derived solution are discussed.

2.2. Analytical solution

The mathematical expression of the one-dimensional vertical (1D_v) sediment advection-diffusivity model is:

$$\frac{\partial C}{\partial t} = W_s \frac{\partial C}{\partial z} + K_s \frac{\partial^2 C}{\partial z^2} \quad (2.2)$$

where C is the SSC, which is a function of the time (t) and the distance above the seabed (z), and W_s and K_s are sediment settling velocity and sediment vertical eddy diffusivity, respectively. For the sake of simplicity, K_s is assumed to be constant over time and space in tidal environments (Prandle 1997; Jung et al. 2004).

The standard practice in research on non-cohesive suspended sediment transport is to specify a bottom concentration boundary condition (a reference concentration) for eq. (2.2) (Dyer 1986). This boundary condition ($z = 0$) is here defined as an arbitrary function of time $f(t)$, which, if it converges, can be transformed to a summation of a trigonometric Fourier series:

$$C(0, t) = f(t) = N_0 + \sum_{i=1} N_i \cos(\omega_i t + \phi_i) \quad \omega_i \neq 0 \quad (2.3)$$

The analytical solution of eq. (2.2) using the boundary condition defined in eq. (2.3) can then be obtained from:

$$C(z, t) = N_0 \exp\left(-\frac{W_s}{K_s} z\right) + \sum_{i=1} N_i \exp\left(-a_i \frac{W_s}{K_s} z\right) \cos\left(\omega_i t + \phi_i - b_i \frac{W_s}{K_s} z\right)$$

$$a_i = (1 + \sqrt{1 + 4b_i^2}) / 2 \quad (2.4)$$

$$b_i = \left(\frac{1 + \sqrt{1 + 16\omega_i^2 K_s^2 / W_s^4}}{8}\right)^{0.5}$$

In eq. (2.4), if $4\omega_i K_s / W_s^2 \gg 1$ or $\ll 1$, coefficients a_i and b_i will reduce to:

$$\text{Conditions (A): } a_i = 0.5 + b_i = 0.5 + \frac{1}{W_s} \sqrt{\frac{\omega_i K_s}{2}} \quad b_i = \frac{1}{W_s} \sqrt{\frac{\omega_i K_s}{2}} \quad \text{if } \frac{4\omega_i K_s}{W_s^2} \gg 1 \quad (2.5)$$

$$\text{Conditions (B): } a_i = \frac{1}{2}(1 + \sqrt{2}) = 1.207 \quad b_i = 0.5 \quad \text{if } \frac{4\omega_i K_s}{W_s^2} \ll 1$$

The reference concentration can be calculated in terms of the bed concentration C_0 and the normalized excess shear stress s (Smith and Mclean 1977) as:

$$C(0, t) = C_0 \gamma s / (1 + \gamma s) \quad (2.6)$$

$$s = (\tau - \tau_{cr}) / \tau_{cr}$$

where τ and τ_{cr} are the shear stress and critical shear stress, respectively, and γ is an

empirical constant with the range of 10^{-3} ~ 10^{-5} (Smith and McLean 1977; Hill et al. 1988; Drake and Cacchione 1989). By transforming eq. (2.6) to the format of eq. (2.3), the temporal and spatial evolution of SSC can be resolved by eq. (2.4). This would be a general solution for arbitrary parameters.

In a simple case with a low value of (γs), eq. (2.6) reduces to $C(0, t) = C_0 \gamma s$. The shear stress, $\tau = \rho C_D u^2$, can be determined using the vertical mean velocity u with a constant drag coefficient C_D , and if τ is sufficiently larger than τ_{cr} , eq. (2.6) can be reduced to $C(0, t) = \beta C_0 \gamma \rho C_D u^2 / \tau_{cr}$ as a first order harmonic approximation with a constant β which is less than 1. For a simple M₂ tidal current, u is assumed to be:

$$u = U \cos \omega t \quad (2.7)$$

where U is the tidal current amplitude, and ω is the semi-diurnal constituent (M₂).

On this basis, the boundary condition can finally be simplified to:

$$C(0, t) = \frac{\beta C_0 \gamma C_D U^2}{2\tau_{cr}} (1 + \cos 2\omega t) = N(1 + \cos 2\omega t) \quad N = \frac{\beta C_0 \gamma C_D U^2}{2\tau_{cr}} \quad (8)$$

where the solution of $C(z, t)$ can be easily obtained using eq. (2.4):

$$C(z, t) = N \exp\left(-\frac{W_s}{K_s} z\right) + N \exp\left(-a \frac{W_s}{K_s} z\right) \cos\left(2\omega t - b \frac{W_s}{K_s} z\right) \quad (2.9)$$

$$a = (1 + \sqrt{1 + 4b^2}) / 2$$

$$b = \left(\frac{1 + \sqrt{1 + 64\omega^2 K_s^2 / W_s^4}}{8}\right)^{0.5}$$

Equation (9) shows that the SSC profile has a time-independent, exponentially decreasing term (the first term of RHS of eq. (2.9)) and an M₄ quarter-diurnal variation term (the second term of RHS of eq. (2.9)). The time-independent, exponentially decreasing term equals the SSC profile when the averaged reference boundary concentration ($C(0, t)=N$) is in steady state. This term represents the averaged SSC profile.

For the quarter-diurnal variation term, the vertical phase lag and the amplitude

attenuation is given by:

$$\varphi(z) = b \frac{W_s}{K_s} z \quad (2.10)$$

$$A(z) = N \exp\left(-a \frac{W_s}{K_s} z\right) \quad (2.11)$$

where $\varphi(z)$ is the vertical phase lag, and $A(z)$ is the vertical amplitude attenuation of the periodic variation term. Equation (10) demonstrates that the vertical phase lag increases linearly with the height above the bed, and eq. (2.11) demonstrates that the amplitude decreases exponentially with the height above the bed, both being controlled by the tidal frequency ω , the setting velocity W_s , and the vertical sediment eddy diffusivity K_s . In this formulation a is always larger than 1, which indicates that the amplitude attenuation of the SSC variation is faster than the rate of decrease of the averaged SSC, as can be seen by comparing eq. (2.11) with the first term of RHS of eq. (2.9).

In accordance with eq. (2.5), in Condition (A) associated with a large $8\omega K_s / W_s^2$, the sediment is relatively fine, and the eddy diffusivity is relatively strong, then eq. (2.10) and eq. (2.11) reduce to:

$$\varphi(z) = \sqrt{\frac{\omega}{K_s}} z \quad (2.12)$$

$$A(z) = N \exp\left[-\left(\frac{W_s}{2K_s} + \sqrt{\frac{\omega}{K_s}}\right)z\right] \quad (2.13)$$

Eq. (2.12) shows that, in the case of a strong eddy diffusivity and fine-grained sediments, the rate of phase lag increase is only influenced by ω and K_s , and is neither related to W_s nor to the sediment grain size. If, on the other hand, in Condition (B), the sediment is relatively coarse with a low eddy diffusivity, then a and b are both constant. This suggests that the rates of phase lag increase and amplitude decrease are only controlled by K_s and W_s , neither being related to ω . This suggests that another time scaling parameter, namely the tidal frequency ω , is of importance in addition to

the basic scaling $W_s h / K_s$ for steady and uniform flow (Prandle, 1997). In Condition (B), the coarse sediment having a low eddy diffusivity causes the reduced effects in the tidal variation time scale, and as a result, the independence of the solution to ω . It is also noted that eq. (2.12) of the phase lag in SSC is of the same character as the lag in turbulent kinetic energy (TKE) production in Simpson (2000).

Integrating eq. (2.9), the vertical averaged SSC can be written as:

$$\begin{aligned} \overline{C(t)} = \frac{1}{h} \int_0^h C(z, t) dz = \frac{N K_s}{h W_s} \{1 - \exp(-\frac{W_s}{K_s} h) \\ + \frac{1}{\sqrt{a^2 + b^2}} [\cos(2\omega t - \tan^{-1} \frac{b}{a}) - \exp(-a \frac{W_s}{K_s} h) \cos(2\omega t - \tan^{-1} \frac{b}{a} - b \frac{W_s}{K_s} h)]\} \end{aligned} \quad (2.14)$$

where h is the water depth. The typical values of W_s and K_s are in the order of 10^{-2} to 10^{-3} , and the water depth in the order of 10 m. If $W_s h / K_s$ is sufficiently larger than 1, considering $a > 1$, the terms $\exp(-W_s h / K_s)$ and $\exp(-a W_s h / K_s)$ in this equation will be much lower than 1. In this situation, we neglect these terms, and the vertically averaged SSC is:

$$\overline{C(t)} = \frac{1}{h} \int_0^h C(z, t) dz = \frac{N K_s}{h W_s} [1 + \frac{1}{\sqrt{a^2 + b^2}} [\cos(2\omega t - \tan^{-1} \frac{b}{a})]] \quad (2.15)$$

This simplified solution can provide a clear estimation of the phase lag of the vertically averaged SSC behind the velocity, which is $\tan^{-1}(b/a)$ and ranges between 0 and 0.5π . It should be noted that this simplified solution is only valid in the conditions mentioned above. While the Neumann boundary condition (zero sediment flux at the sea surface) would be valid for a greater range of conditions, the analytical expression of the vertically averaged SSC would then be much more complex, and that would be beyond the scope of the present paper.

In Fig. 2.1, the predicted temporal evolution of SSC profiles are demonstrated for a representative tidal situation with $W_s = 2 \text{ mm s}^{-1}$, $K_s = 0.02 \text{ m}^2 \text{ s}^{-1}$, $\omega = 1.4 \times 10^{-4} \text{ s}^{-1}$, and a 20 m water depth. In this case, the vertical phase lag is 5.24 degrees per meter, and the amplitude of SSC variation is 0.86 times that at the location 1 m deeper.

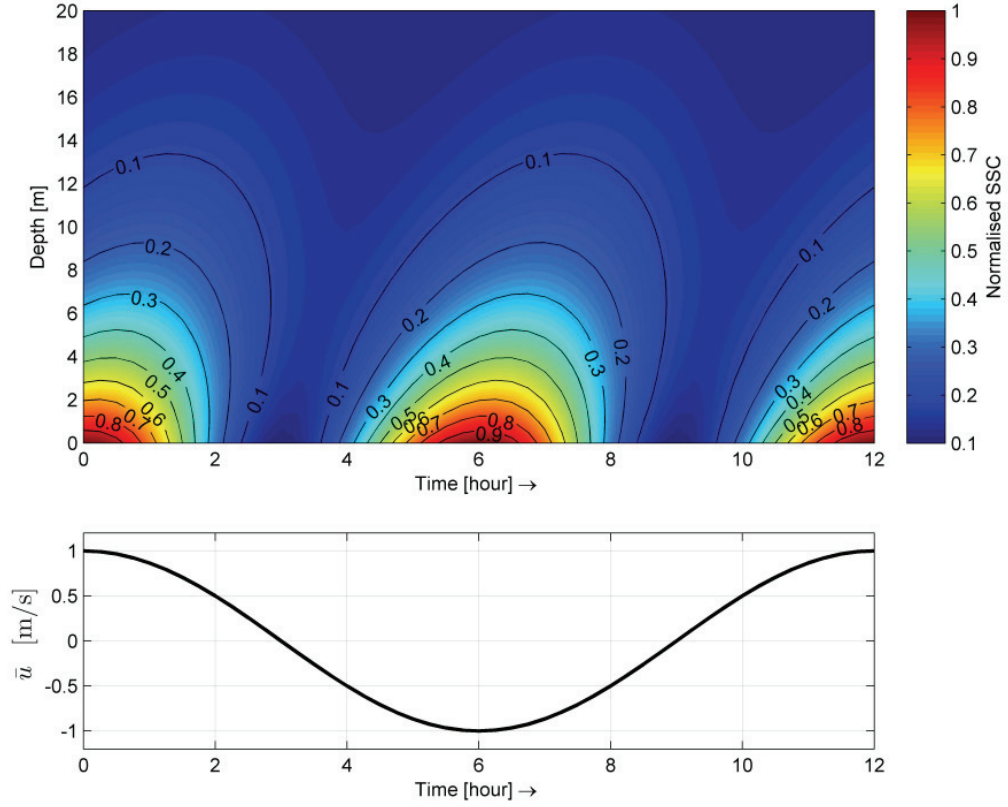


Fig. 2.1 Prediction of the variation in SSC with time in an M_2 tidal cycle. The predicted SSCs are calculated by eq. (2.9) for a representative tidal situation with $W_s = 2 \text{ mm s}^{-1}$, $K_s = 0.02 \text{ m}^2 \text{ s}^{-1}$, $\omega = 1.4 \times 10^{-4} \text{ s}^{-1}$, at a 20 m water depth. The SSC is normalized by the maximum value

The relationship between current velocity at the bed and SSC at a given height above the bed is specified in terms of eq. (2.7) and eq. (2.9), which can be simply represented as the relation of function $y(t)$ and the normalized velocity $x(t)$ at a given depth:

$$y(t) = \cos(2\omega t - \varphi) \quad (2.16)$$

$$x(t) = \left(\frac{u}{U}\right)^2 = \frac{1}{2}(\cos 2\omega t - 1) \quad (2.17)$$

Function $y(t)$ in eq. (2.16) represents the variation of SSC, being the simple-harmonic variation term in eq. (2.9), other parts in eq. (2.9) all being independent of time and hence of velocity, while φ is the phase lag defined in eq. (2.10). Function $x(t)$ in eq. (2.17) is the square of the normalized velocity, which has the same frequency as $y(t)$

and represents the current speed (the absolute value of velocity). This relationship is similar to the phase difference model suggested by Allen (1974). It is easy to eliminate the time between eq. (2.16) and (17), and to transform the relationship between y and x to a standard ellipse function:

$$\begin{aligned} (1 - \cos \varphi)X^2 + (1 + \cos \varphi)Y^2 &= (\sin \varphi)^2 \\ X &= (2x + y - 1) / \sqrt{2} \\ Y &= (y - 2x + 1) / \sqrt{2} \end{aligned} \tag{2.18}$$

When $\varphi = k\pi$ ($k = 0, 1, 2 \dots$), eq. (2.18) mathematically transforms into a line, which demonstrates that there are unique SSCs corresponding to given current speeds. If $\varphi \neq k\pi$, this equation describes an elliptical loop, the lengths of the major and minor axes of which are controlled by the phase lag φ . This indicates that, for a given current speed, there are two corresponding SSCs, one being associated with the accelerating, the other with the decelerating current speed. These elliptical loops are illustrated with respect to different values of $\varphi = 0, \pi/4, \pi/2$ and $3/4\pi$ in Fig 2.2.

Because the phase lag φ increases linearly with the height (z) in terms of eq. (2.10), the relationships between speed and SSC change with z . In the near-bed area, where most observations of SSC are made (e.g., Cacchione et al. 2006), a low phase lag φ (usually between 0 and 0.5π) produces counterclockwise loops in this relationship. A characteristic feature is that during accelerating flow the SSC is lower than during decelerating flow at corresponding current speeds, similar to the ellipse in Fig. 2.2 where $\varphi = \pi/4$. This is consistent with the general pattern of the observations cited in the introduction. In accordance with a phase lag of $\tan^{-1}(b/a)$ in eq. (2.15), which ranges between 0 and 0.5π , the depth-averaged SSC has a similar relationship with current speed.

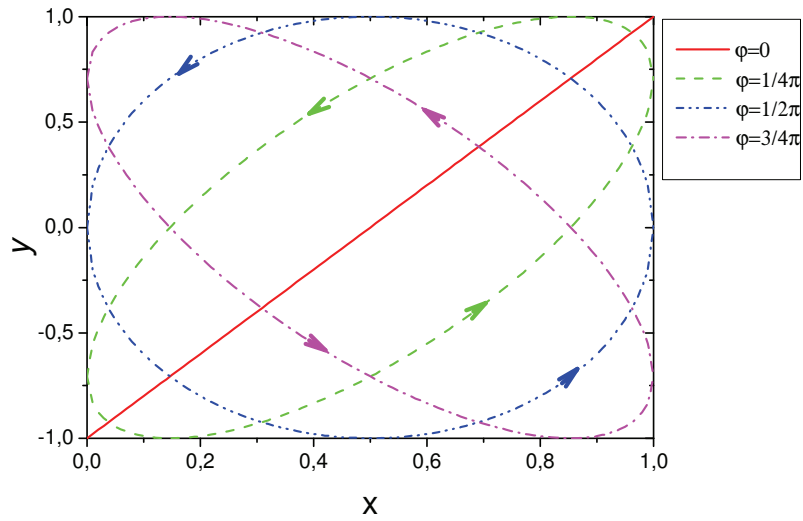


Fig. 2.2 Relationships between current speed and SSC at a given height above the bed where y and x are defined by eq. (2.16) and (17), respectively. y represents the variation of SSC, and x is the square of the normalized velocity representing the current speed (the absolute value of velocity). The resulting curves are either ellipses or straight lines, depending on the phase lag φ . The arrows indicate the direction of change in the individual curves (cf. text for details)

2.3. Validation

To validate our analytical solution of the vertical SSC phase lag and amplitude attenuation, the observations of Souza et al. (2004) were utilized. These authors had deployed a 1200 kHz acoustic Doppler current profiler (ADCP) over a spring tidal period between 27 and 29 May 2002 at a mean water depth of about 25 m in the tidally mixed region of the upper Gulf of California. The mean velocities and Reynolds stresses were estimated using two pairs of opposing acoustic beams, and the SSC was estimated from the acoustic backscatter. During the observational period, the tides were dominated by semi-diurnal components, the tidal velocities being almost rectilinear and of the order of 0.6 m s^{-1} near the sea surface and 0.3 m s^{-1} near the bottom. The eddy viscosity and sediment settling velocity were estimated to be between 10^{-3} and $10^{-2} \text{ m}^2 \text{ s}^{-1}$ and 0.0001 and 0.001 m s^{-1} , respectively. The vertical phase lag and the amplitude of SSC from 1 to 7 m above the seabed were also taken from Souza et al. (2004) (see Fig 2.3).

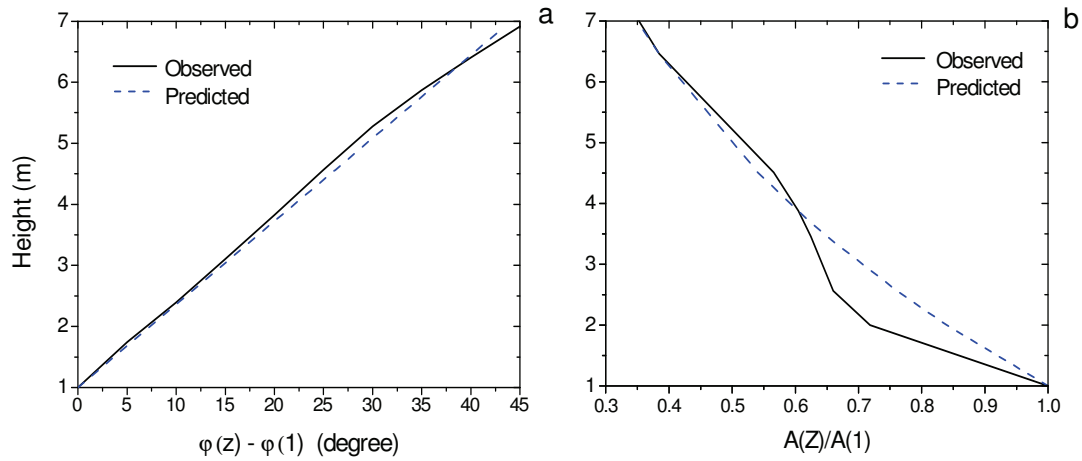


Fig. 2.3 (a) The vertical SSC phase lag from 1 to 7 m above the bed (the values are relative to the bottom phase). (b) The vertical SSC amplitude attenuation from 1 to 7 m above the bed (the values are normalized to the bottom amplitude). The observed curves are from Souza et al. (2004), the predicted curves based on eq. (2.10) and (11), respectively

The analytical solution uses the observed values of W_s and K_s with an M_2 frequency of $1.4 \times 10^{-4} \text{ s}^{-1}$. The eddy diffusivity is usually considered to be equal to the water eddy viscosity (Dyer 1986), K_s being chosen as $0.9 \times 10^{-2} \text{ m}^2 \text{ s}^{-1}$, and the settling velocity being set at 0.00075 m s^{-1} . The theoretically predicted curves of the vertical SSC phase lag and amplitude attenuation are illustrated in Figs 2.3a, b, which show reasonable agreement between observations and predictions.

From Fig. 2.3b it can be seen that the analytical solution predicts the vertical phase lag better than the amplitude attenuation, the most pronounced departure between the predicted and observed amplitude attenuation curves being located in the intense attenuation region of the lower part of the profile. This phenomenon can be explained by the effect of the sediment grain-size spectrum at the ADCP site.

If $K_s = 0.9 \times 10^{-2} \text{ m}^2 \text{ s}^{-1}$ and $\omega = 1.4 \times 10^{-4} \text{ s}^{-1}$ then, based on the W_s range of 0.0001 and 0.001 m s^{-1} , $8\omega K_s / W_s^2$ will change from 10^3 to 10 , which is still sufficiently larger than 1. In terms of the analysis of eq. (2.11) and (2.12), the rate of phase lag change is

almost unrelated to W_s , but the exponential rate on amplitude attenuation is strongly influenced by W_s (see Fig. 2.4). This indicates that the mixture of different grain sizes has little effect on the rate of phase lag change but a significant effect on the rate of amplitude attenuation.

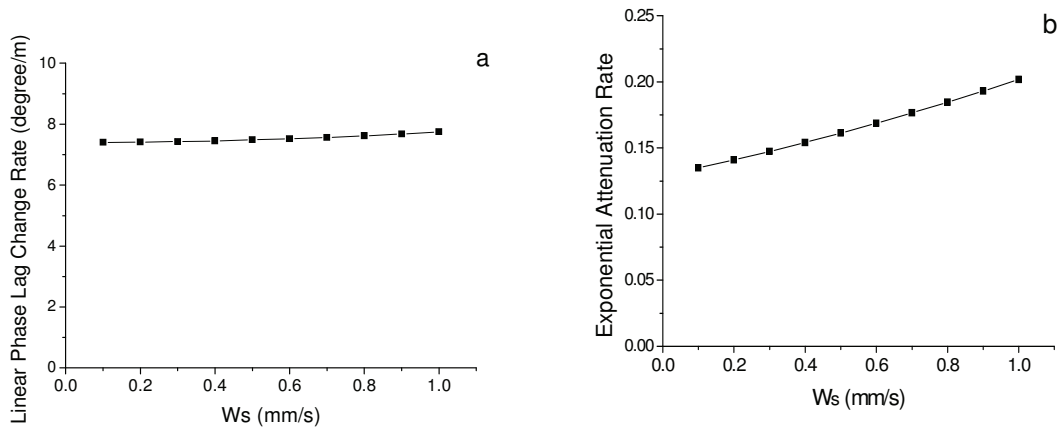


Fig. 2.4 (a) The relationship between the rate of linear phase lag change ($= bW_s/ K_s$, see eq. (2.10)) and particle settling velocity. (b) The relationship between the rate of exponential amplitude attenuation ($= aW_s/ K_s$, see eq. (2.11)) and particle settling velocity. Both datasets were calculated using eq. (2.9) with $K_s = 0.9 \times 10^{-2} \text{ m}^2 \text{ s}^{-1}$ and $\omega = 1.4 \times 10^{-4} \text{ s}^{-1}$

Due to the presence of coarse grains with relatively large settling velocities, the total SSC amplitude tends to decrease more rapidly, as shown in the lower part of Fig. 2.3b where the height above the bed is less than 3.5 m. Because of the rapid attenuation of coarse grains with distance from the bed, their contribution to the total SSC amplitude diminishes rapidly and can eventually be neglected when the distance to the bed is large enough. In the part of the profile away from the bed, most of the suspended sediment is composed of fine grains associated with lower attenuation rates (see Fig. 2.4b). That is why the amplitude attenuation rate is reduced in the upper part of Fig 2.3b. It should be noted that the theoretically predicted curve in Fig 2.3 can be considered to represent an average relationship.

2.4. Discussion

The mechanism generating the phase lag effect demonstrated above is the lag of sediment movement or the “diffusion/settling lag”. The concept of “settling lag”, which was originally proposed by van Straaten and Kuenen (1958) and Postma (1961) to explain the net landward directed sediment transport on tidal flats, is related to the time needed for the sediment to settle out during decreasing flow. In analogy, the “diffusion lag” is associated with the time needed for the sediment to be transported from a high concentration level to a low concentration level by the diffusion process. Diffusion lag can both act during accelerating and decelerating flows when SSC gradients exist. In a period of accelerating flow, bottom SSC increases rapidly with increasing current speed, which causes an upward decreasing SSC, the sediment needing time to be lifted to a higher level by the upward diffusion process. In a period of decelerating flow, bottom SSC decreases rapidly with decreasing current speed, which causes a downward decreasing SSC, the sediment needing time to be transported from a higher level to a lower level by the downward diffusion process. The settlement of sediment compensates the upward diffusion and enhances the downward diffusion. Because it takes more time for sediment to be lifted/settle to/from a higher level, the phase lag increases with distance above the bed, as predicted by eq. (2.10). In short, the phase lag is the time taken for sediment to respond to the changing current.

Being controlled by two opposing processes, the influence of sediment settling velocity on the response of SSC to the periodic currents is complex. The high settling velocity of coarse grains hinders the upward movement of sediment by diffusion when the velocity increases. This results in a delayed response of SSC and a large phase lag, but it also enhances rapid downward settling in response to the decreasing velocity, which is associated with a small phase lag. Substituting the expression of parameters a and b in eq. (2.9) into eq. (2.10), it can be seen that the phase lag at a given height above the bed correlates positively with the settling velocity, implying a stronger contribution of the former process. However, in terms of eq. (2.15), the phase

lag of the vertically averaged SSC ($\tan^{-1}(b/a)$) correlates inversely with the settling velocity, suggesting the importance of the latter process. This apparent contradiction can be explained by the rapid amplitude attenuation of coarse grains. Although coarse grains have a larger phase lag at a given height, the amplitude of the variation of fine grains is larger than that of coarse grains, which indicates that the number of delayed coarse grains is smaller than that of fine grains, and hence the vertically integrated and averaged SSC has a larger phase lag with fine grains.

Several other factors, which are not included in the present solution, may also be involved in producing the phase lag effect. One contribution is the phase lag of the turbulent Reynolds stresses and the kinetic energy behind the velocity (Allen 1974; Dyer 1986), which has been observed in tidal environments by Gordon (1975) and Thwaites and Williams (2001). Since the turbulence intensity influences sediment eddy diffusivity, the phase lag of turbulence intensity automatically causes a phase lag in SSC. Another factor involved in the phase lag is the contribution of “scour lag” (Allen 1974), which denotes the difference between the critical sediment erosion velocity and the deposition velocity (Postma 1961), but this is of less importance in the case of non-cohesive sediments. In addition, SSC profiles and their response to velocity are distorted by the influence of non-uniform horizontal sediment concentrations (Bass et al. 2002), limitations in sediment availability on the bed, the so-called bed armoring effect (Velegrakis et al., 1997), and stratification effects induced by salinity and/or sediment (Hamblin 1989; Wang et al. 2005).

In the solution, a constant vertical sediment eddy diffusivity K_s is assumed over time and space, in correspondence to several previous analytical approaches (Prandle 1997; Jung et al. 2004). However, as shown by Souza et al. (2004), in the tidal environments K_s will change greatly both in time and in the vertical domain. The potential effects of such inconstant K_s are currently still difficult to quantify analytically, but should clearly be investigated in future studies. It is suspected that, due to sediment erosion, diffusion and high SSC peaks are strongly associated with high velocities, the harmonic signals of SSC variations being possibly more related to such high-velocity

conditions. As a result, the constant K_s fitted to SSC observations may be close to the observed peak K_s values in M2 tidal flows. This consideration is consistent with the fact that the K_s value of $0.9 \times 10^{-2} \text{ m}^2 \text{ s}^{-1}$ used in Fig 2.3 for validation is close to the peak K_s value of about $10^{-2} \text{ m}^2 \text{ s}^{-1}$ observed by Souza et al. (2004). In addition, Souza et al. (2004) applied the analytical solution of Simpson (2000) in the vertical phase lag of TKE production with a constant vertical eddy viscosity (equal to K_s (Dyer 1986)), the result satisfying the eddy viscosity at a value of about 10^{-2} , which is also in good agreement with the observed peak K_s values.

There are several applications of the analytical solution presented here. Firstly, when the classic Rouse equation is used for fitting SSC profiles from which the Rouse number is then derived (e. g., Amos et al. 2010), it is tacitly assumed that sediment diffusion and settling take place rapidly enough to attain steady Rouse profiles. The analytical solution, however, shows that this assumption can cause systematic errors, i.e. the Rouse number may be overestimated for accelerating flows, and underestimated for decelerating flows because of the phase lag effect. As a result, care must be taken when using the Rouse equation if phase lag effects are significant.

Another application is that the phase lag effect has a potential influence on sediment transport and hence morphodynamic modeling. Since the SSC is higher in decelerating than in accelerating flows, the suspended sediment transport rate is higher in decelerating flows, and this contributes to the residual sediment transport if the tidal current is asymmetrical (Groen 1967; Hoitink et al. 2003). Finally, it should be noted that there is a complicated relationship between concentration or suspended sediment transport rate and current speed, and that, as a consequence, the chronology of a sediment transport situation needs to be taken into consideration.

2.5. Conclusions

The analytical solution for generating tide-induced vertical SSC profiles presented in this paper produces simple patterns and trends, which show that the vertical phase lag

of SSC behind velocity increases linearly with the height above the bed, and that the amplitude of SSC variations decreases exponentially with the height, both being controlled by the tidal frequency, the particle settling velocity, and the vertical sediment eddy diffusivity. The relationship between SSC and normalized current velocity can be described by an ellipse or a line with respect to different phase lags.

3. Tide-induced Suspended Sediment Transport: Depth-averaged Concentrations and Horizontal Residual Fluxes

Abstract

In coastal and estuarine waters, depth-averaged suspended sediment concentration (DASSC) at a fixed observation site has two sources: local resuspension and advection along a horizontal gradient. The empirical decomposition method can separate the horizontal residual suspended sediment flux (HRF) into several terms, e.g., Eulerian flux, Stokes' drift, and tidal pumping. A simple depth-averaged 1D model is solved analytically for an observational site to explore the determinants of the forcing factors comprising residual, M2 and M4 current velocities, mean and M2 water depths, and the DASSC gradient relative to the tidal variations of DASSC and HRF. Through the solutions, the relative contributions of local resuspension and advection are clarified, the empirical decomposition terms having clear physical explanations. The solutions are applied to fit and explain the observations at a fixed station in a macro-tidal channel located along the Jiangsu Coast, China. The results suggest a dependence of the M4 DASSC variation on resuspension induced by the M2 velocity, and the dependence of the M2 DASSC variation on the advection and resuspension induced by the interaction between the M2 and M4 velocities. The horizontal DASSC gradient results in large seaward tidal pumping, which is offset by the landward Lagrangian flux to produce a reduced landward HRF.

3.1. Introduction

Understanding the tide-induced behavior of suspended sediment dynamics is vital for morphological, environmental and ecological reasons (Dyer, 1997; Prandle, 1997). There are two key issues in this respect, namely, suspended sediment concentration (SSC), and horizontal residual suspended sediment flux (HRF). The former plays an important role in absorbing and scattering light, and hence influences biological

production (Tian et al., 2009), whereas the latter is essential in determining the fate of the sediment and its associated contaminants, including carbon in the context of the global consequences of anthropogenic change (Jay et al., 1997). For these reasons, SSC and current velocity time series are commonly measured at some fixed field stations during coastal and estuarine hydrodynamic surveys. From such data, the HRF can then be calculated for those locations by the integration of the observed SSC and velocity over individual tidal cycles. Consequently, the interpretation and prediction of SSC and HRF are based on both empirical and theoretical considerations.

By means of harmonic analysis of the tidal current signal, the observed SSC can be decomposed into several periodic components. In areas dominated by the M2 tide and its overtide, field data analysis showed that most of the SSC variance occurs at the M2 and M4 frequencies (Sternberg, 1985; van de Kreeke et al., 1997; Guezennec et al., 1999; van de Kreeke and Hibma, 2005). Theoretically, there are two potential sources for the suspended sediment at the observational point: localized sediment resuspension and horizontal advection. On this basis, Weeks et al. (1993) established a conceptual model to distinguish between these contributions. They suggested that, in an environment dominated by the M2 tidal current and characterized by a horizontal SSC gradient, the M2 SSC variation is due to advection along this gradient, whereas the M4 SSC variation is caused by localized resuspension as it is dependent on the magnitude but not the direction of the M2 current. This concept has been used to separate the contributions of advection and resuspension from observed SSC time series (Jago and Jones, 1998; Eills et al., 2004; Jago et al., 2006; Krivtsov et al., 2008). Furthermore, a similar consideration has been suggested in relating the M2 SSC signal to advection and the M4 SSC signal to resuspension (Sternberg, 1985; Sanford and Halka, 1993; van de Kreeke et al., 1997; van de Kreeke and Hibma, 2005). However, in some cases, more factors act on the system, which can then not be neglected, e.g., residual and M4 tidal currents. The question thus arises as how to specify the interaction of the different forcing factors in order to assess their individual contributions to the tidal SSC variation.

In principle, there is no problem in calculating suspended sediment fluxes from field measurements of SSC and current velocity. In analogy to the estuarine salt transport decomposition method (Dyer, 1974; Fisher, 1976), the suspended sediment flux averaged over a tidal cycle, here called HRF, can be quantified as follows (Dyer, 1997):

$$\begin{aligned}
 F &= \frac{1}{T} \int_0^T \int_0^H U \cdot C \cdot dz \cdot dt \\
 &= \underbrace{C_0 U_0 H_0}_{F1} + \underbrace{C_0 \overline{U_t H_t}}_{F2} + \underbrace{U_0 \overline{H_t C_t}}_{F3} + \underbrace{H_0 \overline{U_t C_t}}_{F4} + \underbrace{\overline{C_t U_t H_t}}_{F5} + \underbrace{H_0 \langle \overline{U_d C_d} \rangle}_{F6} + \underbrace{H_0 \langle \overline{U_d C_d} \rangle}_{F7}
 \end{aligned} \quad (3.1)$$

where C is the SSC, U is the current velocity, T is the tidal period, H is the water depth, the subscript 0 denotes the mean value over time and space, the subscript t denotes the vertically averaged tidal variation, and the subscript d denotes the deviations from the vertical means. Angled brackets ($\langle \rangle$) and overbars ($\overline{\quad}$) signify the means over the depth and the tidal cycle, respectively.

Each decomposed term represents a particular contribution related to a certain physical process (Dyer, 1997). The first term (F1) represents the non-tidal drift, called the Eulerian flux, while the second term (F2) is the flux induced by the Stokes' drift. The two terms denote the residual flow of water and the tidally and vertically averaged SSC to provide the advective sediment flux (the Lagrangian flux). The terms F3 to F5 are the tidal pumping terms that are produced by the phase differences between the depth-averaged suspended sediment concentration (DASSC), the depth-averaged velocity, and the tidal elevation. Term F6 indicates the tidally averaged vertical circulation, while term F7 arises from the changing forms in the vertical distribution of SSC and velocity.

This decomposition method has been applied widely to the study of sediment flux patterns (Uncles et al., 1985a, b; Su and Wang, 1986; Uncles and Stephen, 1993; Barua et al., 1994; Pino Q et al., 1994; Li and Chen, 1998; Wu et al., 2001; Ganju et al., 2005). By comparing the values of the decomposed terms, the relative importance of different processes can be assessed. One important application of the

decomposition method, for example, is to help understand the formation mechanism of estuarine turbidity maxima (ETM) (Dyer, 1997). Especially in well-mixed water bodies, tidal pumping plays a primary role for the maintenance of the ETM, this feature having been revealed by various observational and numerical modeling approaches (Allen et al., 1980; Uncles and Stephen, 1989; Brenon and Le Hir, 1999; Le Hir, 2001).

However, although each decomposed term can be related to particular physical processes, the quantitative contributions of the various forcing factors are not at all clear. For example, the tidal pumping terms are generally explained by the phase differences between the DASSC, the depth-averaged velocity, and the tidal elevation. But the DASSC is also a production of out-forcing factors, including residual and tidal currents, tidal elevations, and horizontal advection. Thus, in order to obtain a comprehensive understanding, the tidal pumping terms must consider the original forcing factors acting at a particular site. This, however, also requires a clarification of how to define the physical basis of each factor for the decomposition procedure.

To solve these issues, several numerical and analytical modeling approaches have been suggested. Thus, Bass et al. (2002) established a numerical model to study the response of SSC to tidal currents by assuming a constant horizontal SSC gradient, the results being then fitted to the observations, thereby supporting the SSC separation concept of Weeks et al. (1993). Although numerical modeling has the advantage of interpreting field observations and analyzing the sensitivity to different parameters, analytical models are better able to provide insights into the generic physics of system evolution (Dronkers, 2005). The analytical solutions of DASSC driven by several tidal constituents (e.g., M₂, M₄) have been investigated by Groen (1967) and Prandle (1997) without, however, considering the contribution of advection. Stanev et al. (2007) and Cheng and Wilson (2008) took horizontal advection into account and solved the depth-averaged one-dimensional (1D) suspended sediment transport equation for a particular site, but neglected the residual current velocity and water depth variation. While Cheng and Wilson (2008) compared their solution with

numerical modeling results, none of the above analytical solutions were directly compared with field observations.

The analytical formula of HRF is based on the solution of DASSC. Because of the lag response of SSC to the tidal current (Yu et al., 2011), the horizontal transport of suspended sediment is more complicated than that for bedload (van de Kreeke and Robaczewska, 1993; van Maren et al., 2004). As advection is not included in the DASSC solutions of Groen (1967) and Hoitink et al. (2003), their HRF solutions can not be applied to spatially heterogeneous areas. This effect, on the other hand, was considered by Cheng and Wilson (2008), but because they neglected the contributions of residual current velocity and water depth variation, some decomposition terms of the HRF in eq. (3.1), which represent the Stokes' drift and a part of the tidal pumping, can not be specified. Prichard (2005) provided semi-analytical solutions for HRF, but these are relatively complex and hence difficult to directly implement in practice.

The present study attempts to solve the 1D depth-averaged suspended sediment transport equation for a particular site with a more comprehensive inclusion of forcing factors (e.g., M2 tidal elevation, residual, M2 and M4 tidal currents, and a horizontal DASSC gradient). On this basis, the HRF is then formulated analytically and the physical meanings of its first 5 decomposition terms are clarified. The solutions are verified by field observations at an anchor station in a macro-tidal embayment located along the Jiangsu Coast, China.

3.2. Analytical solution

At first, a lateral homogeneous environment is assumed where the longitudinal 1D depth-averaged suspended sediment transport model is defined as

$$\frac{\partial \langle C \rangle H}{\partial t} = -\frac{\partial \langle UC \rangle H}{\partial x} + Resuspension + Deposition \quad (3.2)$$

with C as the SSC and U as the current velocity, both being functions of time (t) and horizontal distance (x), and H as the water depth. The horizontal diffusion term is

neglected (Bass et al., 2002; Stanev et al., 2007). The first term on the right-hand side (RHS) represents the contribution from horizontal advection. In addition, simultaneous local resuspension and deposition are assumed (Sanford and Halka, 1993) and width variations in velocity and SSC have been suppressed for simplicity.

The horizontal advection term in eq. (3.2) can be decomposed as follows:

$$\frac{\partial \langle UC \rangle H}{\partial x} = \frac{\partial \langle U \rangle \langle C \rangle H}{\partial x} + \frac{\partial \langle U_d C_d \rangle H}{\partial x} \quad (3.3)$$

The second term in the RHS of eq. (3.3) indicates the nonlinear interaction between the vertical velocity and SSC profiles. For the sake of simplicity, the third term in eq. (3.3) is not considered further as in other depth-averaged models (Dronkers, 1986; Uncles and Stephens, 1989; Cheng and Wilson, 2008). Equation (3) then reduces to:

$$\frac{\partial \langle UC \rangle H}{\partial x} = \frac{\partial \langle U \rangle \langle C \rangle H}{\partial x} = \langle U \rangle H \frac{\partial \langle C \rangle}{\partial x} + \langle C \rangle \frac{\partial \langle U \rangle H}{\partial x} \quad (3.4)$$

The resuspension rate due to the tidal current is written as (Prandle, 1997):

$$Resuspension = B \langle U \rangle^2, \quad B = \frac{M \rho C_D}{\tau_{cr}} \quad (3.5)$$

where M is an erosion constant, and C_D is the drag coefficient applicable to the depth-averaged velocity, and τ_{cr} is the critical erosion shear stress. For the sake of simplicity, M , C_D , and τ_{cr} are assumed to be constant over time and space. Coefficient B thus becomes a constant that represents the resuspension capacity.

The deposition rate is given by:

$$Deposition = W_s C_{bed} = D \langle C \rangle H, \quad D = W_s \frac{C_{bed}}{\langle C \rangle H} \quad (3.6)$$

where W_s is the sediment setting velocity, and C_{bed} is the near-bed SSC. For the sake of simplicity, it is assumed that the settling velocity and the ratio between the near-bed SSC (C_{bed}) and the vertical sediment inventory ($\langle C \rangle H$) are constant over time and space. Coefficient D thus also becomes a constant, which represents the deposition capacity.

Combining eqs. (3.2) to (3.6) with the continuity equation for flowing water:

$$\frac{\partial \langle U \rangle H}{\partial x} = -\frac{\partial H}{\partial t} \quad (3.7)$$

a simple form of the continuity equation for suspended sediment is obtained:

$$\frac{\partial \langle C \rangle}{\partial t} + D \langle C \rangle = -\langle U \rangle \frac{\partial \langle C \rangle}{\partial x} + \frac{B}{H} \langle U \rangle^2 \quad (3.8)$$

In this equation, three basic processes, namely advection of a horizontal DASSC gradient, local resuspension, and deposition are described. The second term on the left-hand side (LHS) represents the contribution of deposition, which is proportional to the DASSC, and the first and second terms of the RHS stand for the contributions of advection and resuspension, respectively. The effects of advection on the DASSC depend on the velocity and the horizontal DASSC gradient, the latter being hard to estimate analytically in practice. A substitute method to simulate this gradient is to find an approximate formula using empirical parameters from the study site. For example, the gradient can be assumed to be uniform and hence represented by a constant value (Weeks et al, 1993; Bass et al., 2002), or to be expressed as a combination of several temporal harmonic terms (Cheng and Wilson, 2008). At the study site, the tidal characteristics of current velocity and water depth can be obtained through harmonic analysis of observational data. By parameterizing the horizontal DASSC gradient, $\langle U \rangle$, and H in the harmonic series, the RHS of the eq. (3.8) can be written as a summation of a trigonometric Fourier series only associated with time:

$$\frac{\partial \langle C \rangle}{\partial t} + D \langle C \rangle = \sum_{i=1} A_i \cos(\omega_i t + \psi_i) \quad (3.9)$$

where A_i , ω_i and ψ_i are the amplitude, frequency and phase of the i th forcing harmonics, respectively. The general analytical solution of eq. (3.9) can now be written as:

$$\langle C \rangle = S \cdot e^{-Dt} + \sum_{i=1} \frac{A_i}{\sqrt{\omega_i^2 + D^2}} \cos(\omega_i t + \psi_i - \theta_i), \quad \theta_i = \tan^{-1} \frac{\omega_i}{D} \quad (3.10)$$

where S is an integral constant, and when the evolution of $\langle C \rangle$ tends to be stable, the first term of the RHS of eq. (3.10) becomes trivial and can be neglected. This solution depicts the temporal evolution of the DASSC at the study site.

Comparing the above two equations indicates that the i th harmonic of $\langle C \rangle$ in the second term of the RHS of eq. (3.10) responds to the i th forcing harmonic in the RHS of eq. (3.9) with the same frequency ω_i but with the amplitude reduced by the factor $(\omega_i^2 + D^2)^{1/2}$, on account of which the phase lags by θ_i .

In this study, the particular case is investigated where the transformation from the RHS of eq. (3.8) to the harmonic series in the RHS of eq. (3.9) can be specified. At first, because the dominant astronomical tide along much of the world's coasts is the semi-diurnal lunar tide (M2), the rectilinear tidal velocity can be modeled by a superposition of the M2 tide and its most significant overtide M4 (Friedrichs and Aubrey, 1988):

$$\begin{aligned} \langle U \rangle &= u_0 + u_1 \cos(\omega t + \phi_1) + u_2 \cos(2\omega t + \phi_2) & \hat{u}_0 &= u_0/u_1 \\ &= u_1 [\hat{u}_0 + \cos(\omega t + \phi_1) + \hat{u}_2 \cos(2\omega t + \phi_2)] & \hat{u}_2 &= u_2/u_1 \end{aligned} \quad (3.11)$$

where u_0 , u_1 and u_2 are the depth-averaged amplitudes of the residual, M2 and M4 velocities, respectively, ϕ is the phase of tidal velocity, and ω is the M2 tidal frequency. Since the amplitudes of residual and M4 velocities are typically one order of magnitude lower than the M2 amplitude, u_0 and u_2 are normalized by u_1 as \hat{u}_0 and \hat{u}_2 , respectively. These dimensionless variables are typically in the order of 0.1.

Similarly, the water depth can be modeled by a superposition of the M2 and M4 tides:

$$\begin{aligned} H &= h_0 + h \cos(\omega t + \phi) + h_2 \cos(2\omega t + \phi_2) & \hat{h} &= h/h_0 \\ &= h_0 [1 + \hat{h} \cos(\omega t + \phi)] \end{aligned} \quad (3.12)$$

where h_0 is the average water depth, and h and h_2 are the amplitudes of the M2 and M4 tidal elevations, respectively, and ϕ is the phase of the tidal elevation. In coastal and estuarine environments, it is assumed that h_0 is significantly larger than h , and h is

significantly larger than h_2 . Therefore, the contribution of the M4 tidal elevation can be neglected, and the dimensionless \hat{h} is typically one order lower than 1. The inverse of the water depth can be approximated by:

$$\frac{1}{H} = \frac{1}{h_0[1 + \hat{h} \cos(\omega t + \phi)]} = \frac{1}{h_0} [1 - \hat{h} \cos(\omega t + \phi)] \quad (3.13)$$

Because the spatial information on the DASSC is frequently unavailable in the field, a constant gradient (k) over time at the study site is assumed for the sake of simplicity in accordance with previous models (Prandle, 1997; Bass et al., 2002; Hill et al, 2003). The particular value of k can be attributed to the spatial heterogeneity of tidal currents, wave activity, sediment supply or water depth, and is especially valid for fine-grained materials (Prandle, 1997):

$$\frac{\partial \langle C \rangle}{\partial x} = k \quad (3.14)$$

Substituting eqs. (3.11), (3.13) and (3.14) to eq. (3.8), and neglecting the higher order (>1) trivial terms, the solution for the temporal evolution of DASSC is specified as:

$$\langle C \rangle = \sum_{i=1}^8 E_i = \sum_{i=1}^8 \frac{A_i}{\sqrt{\omega_i^2 + D^2}} \cos(\omega_i t + \psi_i - \theta_i), \quad \theta_i = \tan^{-1} \frac{\omega_i}{D} \quad (3.15)$$

The solution consists of eight harmonic terms (E1 to E8), their amplitude, frequency and phase being listed in Table 3.1. Each harmonic represents one or more process affecting the DASSC variation (See Appendix 3A). In terms of this solution, the contributions of the forcing factors, which comprise the residual, M2 and M4 current amplitudes and phases, the mean water depth, the M2 tidal amplitude and phase, and the DASSC gradient, can be determined.

In accordance with the second column in Table 3.1, it can be shown that k/u_1 and B/h_0 are comparable parameters, representing the relative importance of the horizontal advection due to the SSC gradient and the local resuspension, respectively.

Table 3.1. The coefficients of the trigonometric Fourier series in eq. (3.15). (See text for description)

	A_i / u_1^2	ω_i	ψ_i
E1	$-\frac{k}{u_1} \hat{u}_0 + \frac{1}{2} \frac{B}{h_0}$	0	0
E2	$-\frac{k}{u_1} + 2 \frac{B}{h_0} \hat{u}_0 - \frac{1}{2} \frac{B}{h_0} \hat{h} \cos(\phi - \varphi_1)$	ω	φ_1
E3	$\frac{B}{h_0} \hat{u}_2$	ω	$\varphi_2 - \varphi_1$
E4	$-\frac{1}{4} \frac{B}{h_0} \hat{h}$	ω	ϕ
E5	$-\frac{k}{u_1} \hat{u}_2$	2ω	φ_2
E6	$\frac{1}{2} \frac{B}{h_0}$	2ω	$2\varphi_1$
E7	$\frac{B}{h_0} \hat{u}_2$	3ω	$\varphi_1 + \varphi_2$
E8	$-\frac{1}{4} \frac{B}{h_0} \hat{h}$	3ω	$2\varphi_1 + \phi$

The analytical formula of HRF is, in turn, achieved by integrating the known analytical formulas of DASSC (eq. (3.15)) and current velocity (eq. (3.11)) over the vertical domain and the M2 tidal period. Because of the vertically averaged model, the first five terms (F1 to F5) of the HRF decomposition can be determined analytically for physical interpretations. Terms F6 and F7, which are related to the vertical deviations, are not covered by the present study. Neglecting the higher order (>2) trivial terms, the decomposition terms (F1 to F5) are written as:

$$F1 = \frac{u_1^3 h_0}{D} \left(\frac{1}{2} \frac{B}{h_0} \hat{u}_0 - \frac{k}{u_1} \hat{u}_0^2 \right) \quad (3.16)$$

$$F2 = \frac{u_1^3 h_0}{2D} \cos(\varphi_1 - \phi) \left(\frac{1}{2} \frac{B}{h_0} \hat{h} - \frac{k}{u_1} \hat{u}_0 \hat{h} \right) \quad (3.17)$$

$$F3 = -\frac{u_1^3 h_0}{2\sqrt{\omega^2 + D^2}} \frac{k}{u_1} \hat{u}_0 \hat{h} \cdot \cos(\varphi_1 - \phi - \theta_\omega) \quad (3.18)$$

$$F4 = \frac{u_1^3 h_0}{2\sqrt{\omega^2 + D^2}} \left[\left(-\frac{k}{u_1} + 2 \frac{B}{h_0} \hat{u}_0 - \frac{1}{2} \frac{B}{h_0} \hat{h} \cos(\phi - \varphi_1) \right) \cos \theta_\omega + \frac{B}{h_0} \hat{u}_2 \cos(2\varphi_1 - \varphi_2 + \theta_\omega) \right. \\ \left. - \frac{1}{4} \frac{B}{h_0} \hat{h} \cos(\phi - \varphi_1 - \theta_\omega) \right] + \frac{u_1^3 h_0}{2\sqrt{4\omega^2 + D^2}} \left[-\frac{k}{u_1} \hat{u}_2 \cos \theta_{2\omega} + \frac{1}{2} \frac{B}{h_0} \hat{u}_2 \cos(2\varphi_1 - \varphi_2 - \theta_{2\omega}) \right] \quad (3.19)$$

$$F5 = \frac{u_1^3 h_0}{8\sqrt{4\omega^2 + D^2}} \frac{B}{h_0} \hat{h} \cos(\varphi_1 - \phi - \theta_{2\omega}) - \frac{u_1^3 h_0}{4\sqrt{\omega^2 + D^2}} \frac{k}{u_1} \hat{u}_2 \hat{h} \cos(\varphi_1 - \varphi_2 + \phi - \theta_\omega) \quad (3.20)$$

where $\theta_\omega = \tan^{-1} \frac{\omega}{D}$, $\theta_{2\omega} = \tan^{-1} \frac{2\omega}{D}$, representing the phase lag of SSC to the forcing factors in the M2 and M4 frequencies, respectively. The interpretations of F1 to F5 can be found in Appendix 3B.

In practice, when current velocity, water depth, and SSC are measured at a fixed site, the analytical solutions can be applied in the following procedure. In a first step, the values of u_0 , u_1 , u_2 , h_0 , h , φ_1 , φ_2 , and ϕ are identified by harmonic analysis of the measured tidal current and the water depth at the study site. Three free parameters, however, can not be identified independently and thus need to be calibrated by fitting the prediction to the observed DASSC variations: the DASSC gradient k , the resuspension coefficient B , and the deposition coefficient D . Then, the temporal variation of DASSC is specified and its eight decomposed terms in eq. (3.15) are related to the special effects of the different forcing factors with clear physical meanings. The best fit parameters are applied to eqs. (3.16) to (3.20), and then, HRF is predicted and interpreted theoretically.

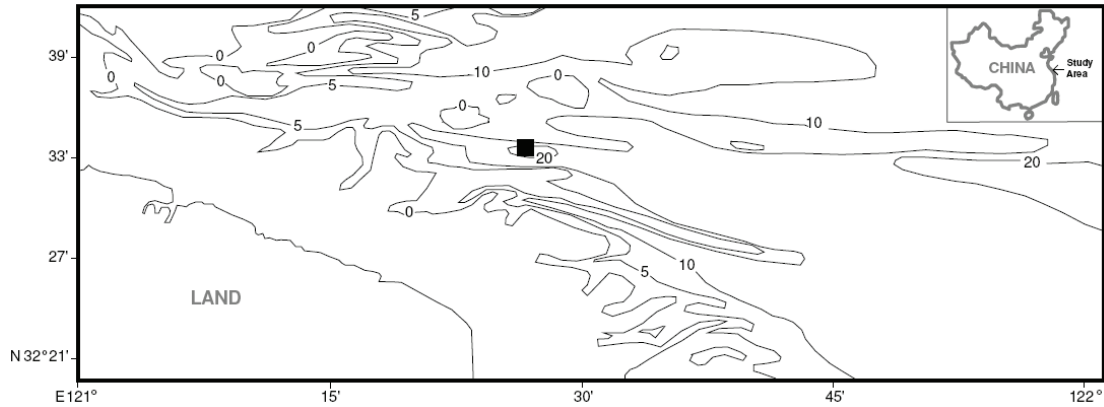


Fig. 3.1. Bathymetric map of the study area. The filled square is the observation site.

3.3. Observations and Applications

Hydrodynamic observations were carried out in a tidal channel located along the Jiangsu Coast, China (Fig. 3.1). Little fresh water flows into the study area, suggesting a well-mixed water body. The study area is characterized by a large tidal range and strong tidal currents of up to 7 m and 2 m s⁻¹, respectively. The M2 tide is the dominant tidal constituent. The bed mainly consists of silt and very fine sand, which are both mostly transported as suspended loads. Samples collected at the site have a mean grain size of 3.8 φ (0.072 mm). Field observations and remote sensing results based on TM images show the on-shore increase of SSC along the Jiangsu coastal sea (Xin et al., 2010).

A ship-mounted downward-looking acoustic Doppler current profiler (ADCP) (600 kHz, RDI) was deployed over a spring tidal period between 15 and 16 July 2003 at an anchor station (121°27' E, 32°34' N) with a mean water depth of about 20 m (Fig. 3.1). Local wind waves are <0.5 m in height and are therefore of minor importance for sediment transport in the channel. Current velocity and acoustic backscatter intensity profiles were recorded every 30 seconds. During the observation, 55 water samples from different water layers were collected at different times. These were subsequently filtered through pre-weighed filters of 0.45 μm aperture. The filters plus sediment were dried and weighed to determine the SSC, which was then used to calibrate the

acoustic signal strength of the ADCP. A linear regression equation was established between SSC (C , in mg l^{-1}) and the ADCP backscatter intensity (EI in dB) (Fig. 3.2):

$$\log_{10}(C) = -4.8557 + 0.0788EI \quad R = 0.86 \quad (3.21)$$

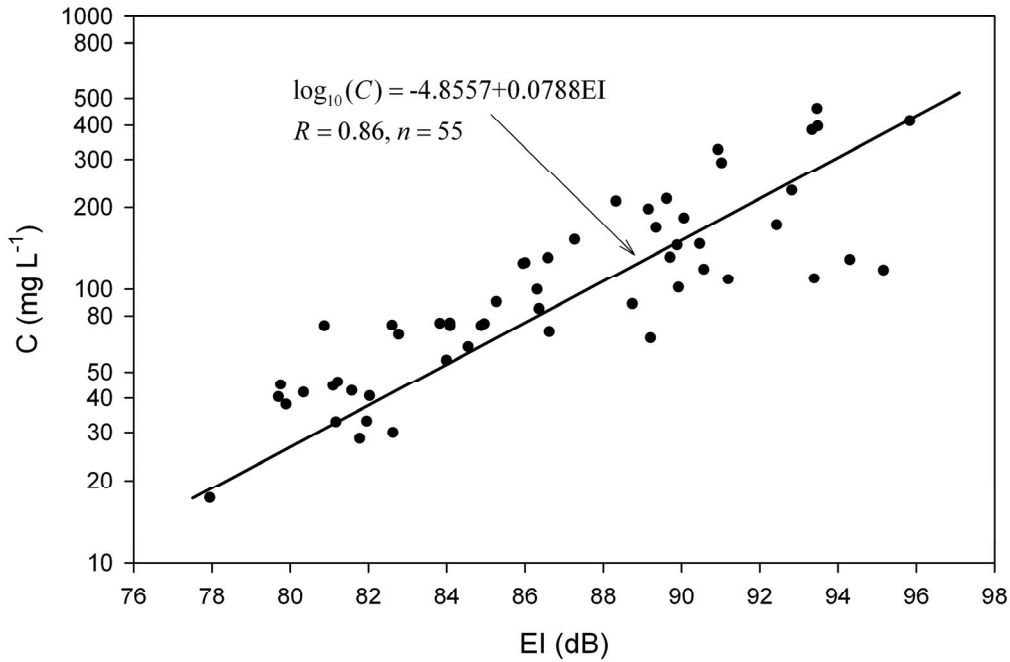


Fig. 3.2. The relationship between SSC (C in mg l^{-1}) and ADCP backscatter signal intensity (EI in dB).

During the observational period, the tidal velocities were almost rectilinear directed east-west along the channel axis. Figure 3.3 shows the temporal evolution of the vertical current speed and SSC profiles, the latter being estimated from the backscatter intensity following eq. (3.21). To remove some of the ruggedness in the high-frequency records, the water depth and the vertically averaged SSC were smoothed using a 10-min window (Fig. 3.4, middle and lower panels). The current speeds and directions were also averaged every 10 min. According to the method of You (2005), the main tidal current direction was determined as being 93° from the north, the measured velocity being then projected in this direction (Fig. 3.4, upper

panel). The projected velocity has positive values towards the sea and the fit by eq. (3.11) represents the combined residual, M2 and M4 velocities:

$$\begin{aligned} \langle U \rangle &= -0.08 + 1.32 \cos(\omega t + 115^\circ) + 0.11 \cos(2\omega t + 219^\circ) \\ &= 1.32[-0.061 + \cos(\omega t + 115^\circ) + 0.083 \cos(2\omega t + 219^\circ)] \end{aligned} \quad (3.22)$$

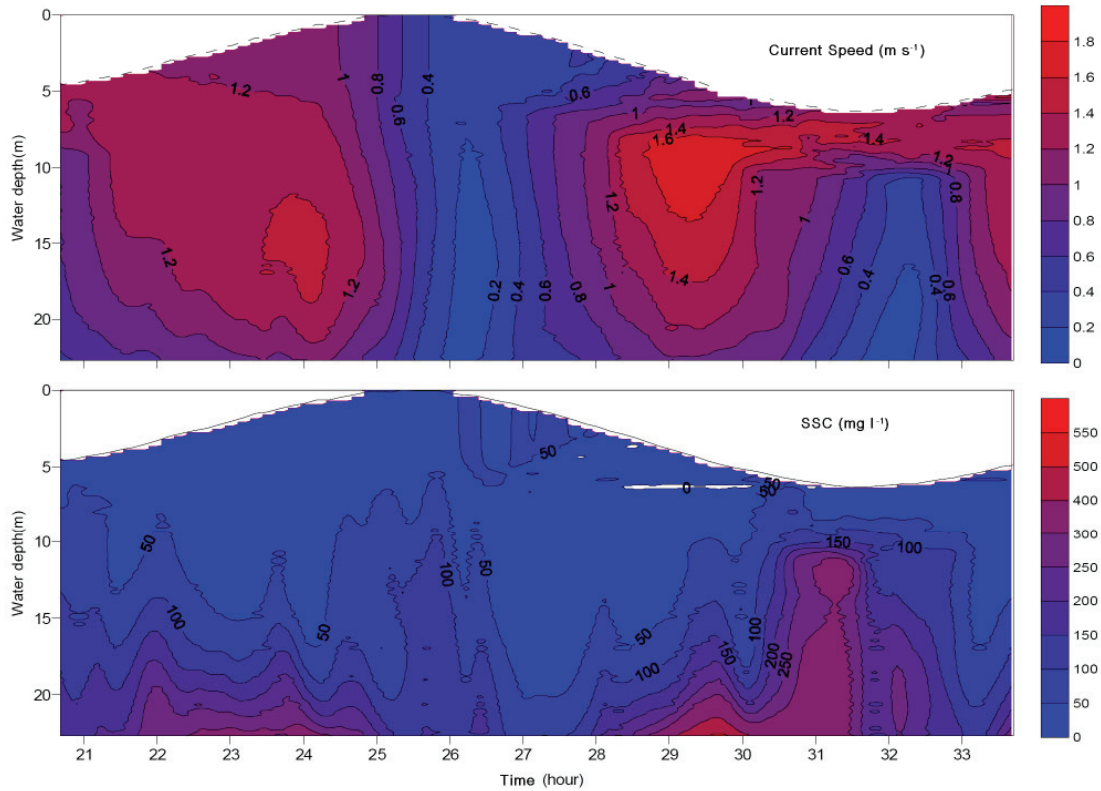


Fig. 3.3. Observed current speed and SSC during a tidal cycle.

The observed and fitted velocities have a high degree of consistency (Fig. 3.4, upper panel). The fitted result (eq. (3.22)) suggests (1) that the dominant M2 velocity amplitude is one order of magnitude larger than the residual and M4 velocities; (2) that the phase difference between the M2 and M4 velocities is ebb dominated; and (3) that the residual velocity is directed landward and has a similar amplitude as the M4 velocity.

Similarly, the observed water depth is fitted by the combined mean depth and M2 tidal elevation following eq. (3.12) (Fig. 3.4, middle panel):

$$H = 19.55 + 3.05 \cos(\omega t + 225^\circ) = 19.55[1 + 0.156 \cos(\omega t + 225^\circ)] \quad (3.23)$$

The M2 tidal range is 6.1 m, its phase leading the M2 velocity by 112° , which results in a primary standing tidal wave and landward Stokes' drift of the water.

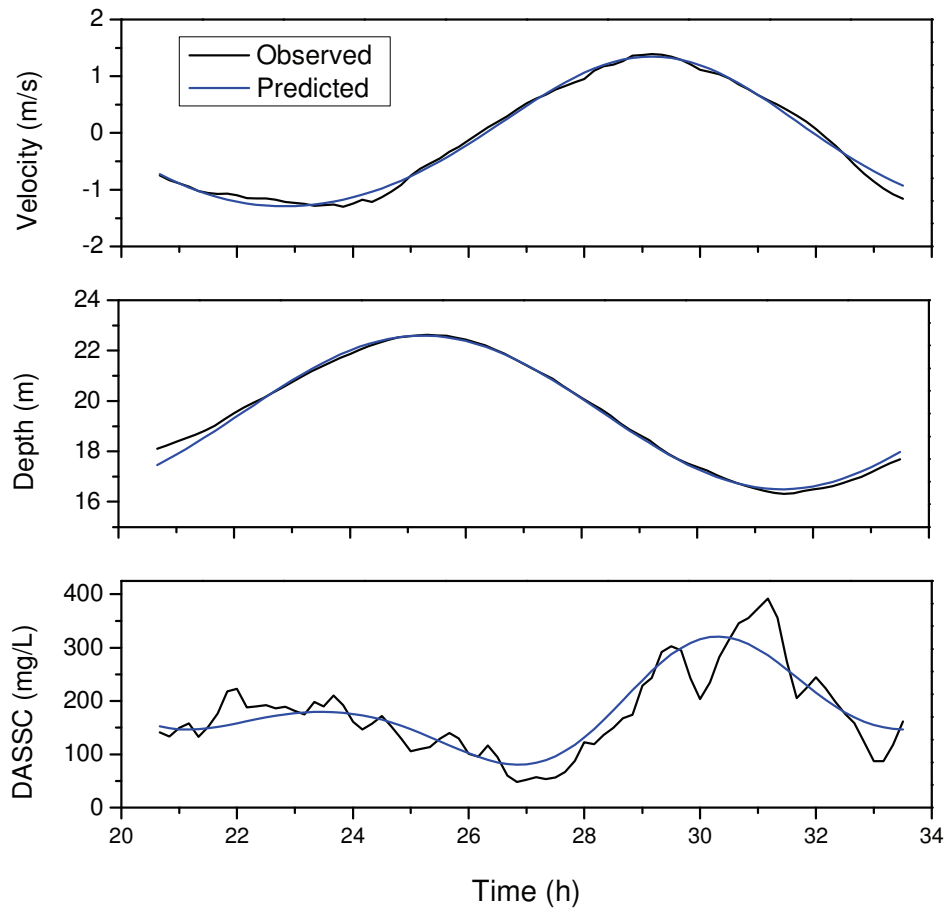


Fig. 3.4. Observed (black curves) and predicted (blue curves) current velocity, water depth, and DASSC. Positive velocities are directed seaward.

Because no spatial DASSC information was available, and the estimation of the mean sediment settling velocity and erosion constant are difficult, the three parameters (k , B , and D) needed to be calibrated. The predicted DASSC based on the analytical solution in eq. (3.15) was fitted to the ADCP concentration data for optimization. A similar

procedure as that used to determine the free parameters by fitting the modeling results to the observational data has previously been applied in other numerical modeling approaches (Sanford and Halka, 1993; Jago and Jones, 1998; Bass et al., 2002; Yang and Hamrick, 2003). Because the best fit parameters encapsulate a number of assumptions and simplifications made in the analytical solution, these parameters may not represent actual values, but are nevertheless useful in interpreting the measured concentration signal.

Before fitting, the ranges of the three parameters must be constrained. The observed tidally averaged DASSC was about 200 mg l^{-1} and the tidal excursion distance about 10 km. As a result, the maximum possible value of the gradient is about $2.0 \times 10^{-5} \text{ kg m}^{-4}$, and the limits for k were thus set at -2.0×10^{-5} and $2.0 \times 10^{-5} \text{ kg m}^{-4}$. Amos et al. (1992) found that the erosion constant M in eq. (3.5) ranges between 2.0×10^{-5} and $3.5 \times 10^{-3} \text{ kg m}^{-2} \text{ s}^{-1}$. In the present study, this range was reduced to 10^{-5} and $5.0 \times 10^{-3} \text{ kg m}^{-2} \text{ s}^{-1}$, and a τ_{cr} of 0.25 N m^{-2} for sand-mud mixtures (van Ledden et al., 2004) and a C_D of 2.5×10^{-3} assumed (Soulsby, 1997). Thus, based on eq. (3.5), the resuspension coefficient B was constrained between 10^{-4} and $5.0 \times 10^{-2} \text{ kg s m}^{-4}$. The lower limit for the sediment settling velocity was set at 0.07 mm s^{-1} (corresponding to a grain size of about $10 \text{ }\mu\text{m}$, cf. Gibbs et al., 1971), the upper limit at 3 mm s^{-1} (corresponding to that of large flocs; Hill and McCave, 2001). The ratio between near-bed SSC and DASSC, which was estimated from the observed SSC profiles, has a mean value of 4.59. In terms of eq. (3.6) and using the mean depth of 19.55 m, the deposition coefficient D ranges between 1.6×10^{-5} and $7.0 \times 10^{-4} \text{ s}^{-1}$.

The best fit prediction of DASSC by the analytical solution is plotted in the lower panel of Fig. 3.4. Compared with the observations, the prediction shows reasonable agreement in that, besides the high-frequency fluctuations in the measured data, the main DASSC variance is represented by the prediction. The calibrated parameters of k , B , and D have reasonable values (Table 3.2). The best fit k of $-8.8 \times 10^{-6} \text{ kg m}^{-4}$ indicates the landward increase in DASSC by 88 mg l^{-1} every 10 km. This landward increase in DASSC in coastal tidal channels had already been recognized by Postma

(1961) in the Dutch Wadden Sea, and is also consistent with the general patterns of the spatial distribution of the Jiangsu Coastal Sea (Xin et al., 2010). The best fit B of $4.2 \times 10^{-4} \text{ kg s m}^{-4}$ and D of $1.0 \times 10^{-4} \text{ s}^{-1}$ are related to an erosion constant of about $4.2 \times 10^{-5} \text{ kg m}^{-2} \text{ s}^{-1}$ and a sediment settling velocity of about 0.42 mm s^{-1} , respectively. The two parameters k/u_1 and B/h_0 are 6.7×10^{-6} and $2.2 \times 10^{-5} \text{ kg s m}^{-5}$, indicating comparable contributions of horizontal advection due to the SSC gradient and local resuspension.

Based on eq. (3.15), the DASSC can be decomposed into eight terms (E1 to E8). The tidally averaged DASSC (E1) of observations and predictions are 177.6 and 181.7 mg l^{-1} , respectively. Applying the best fit parameters to eq. (3.A1) in Appendix 3A illustrates that advection (the first term of the RHS in the equation) contributes -7.1 mg l^{-1} because the residual current comes from a low concentration area, and that local resuspension contributes 188.8 mg l^{-1} .

The tidally varying terms of E2 to E8 are shown in Fig. 3.5. E6, E2 and E3 have amplitudes of 63.3 , 44.2 , and 18.2 mg l^{-1} , respectively, making the largest contribution to the total variation. The relative importance of E_i ($i = 2$ to 8) in eq. (3.15) can be evaluated as the ratio between the amplitude of E_i and the sum of the amplitudes of E2 to E8. The results suggest that the ratios for E6, E2 and E3 are 42.7% , 29.8% and 12.3% , respectively, the sum of the three ratios amounting to 84.8% . E6 has the M4 frequency, and E2 and E3 have the M2 frequency.

On the basis of the analytical solution (Table 3.1 and Appendix 3A), it is known that E6 represents the M4 variation of the DASSC induced by the M2 current resuspension, which corresponds to the local component in the concept of Weeks et al. (1993). Because of the trivial parameters \hat{u}_0 and \hat{h} and the comparable values of k/u_1 and B/h_0 , the amplitude of E2 are dominated by k/u_1 (Table 3.1), this in-phase variation with the M2 velocity being thus mainly attributable to the advection effect. Ebb currents bring high concentration waters to the observation site, resulting in a higher DASSC during the ebb than during the flood tide. If the residual velocity and

the water depth variance are excluded, E2 is consistent with the advection component of Weeks et al. (1993). E3, which is due to the resuspension induced by the interaction of the M2 and M4 velocities, also has an M2 frequency, its relative importance being controlled by \hat{u}_2 . Therefore, the M2 variations of DASSC are not only controlled by advection effects, but are also related to the contributions of the residual velocity, the water depth variance, and, especially, the local resuspension.

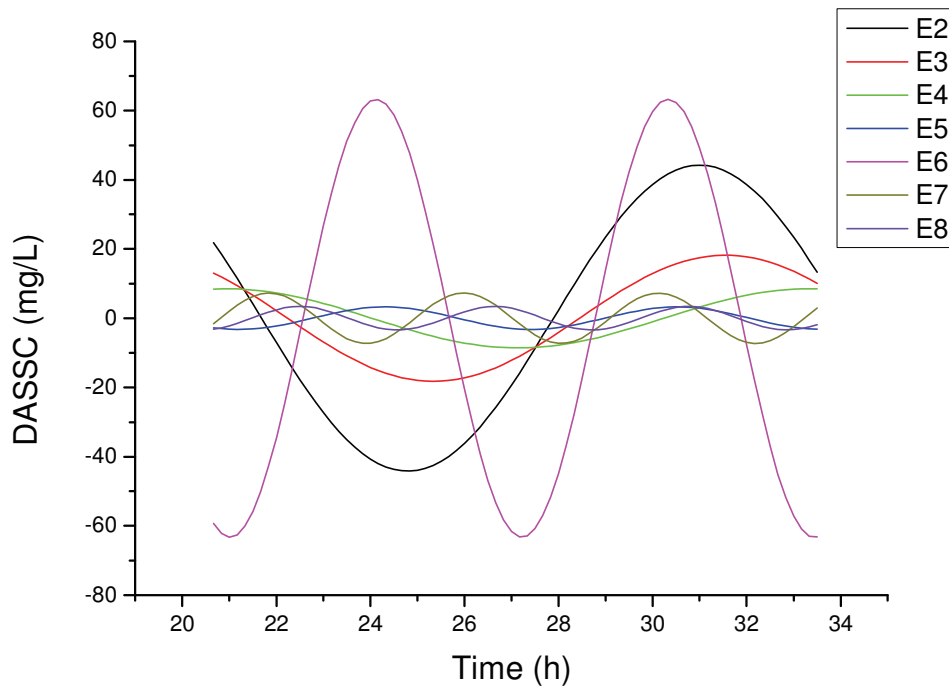


Fig. 3.5. Periodic decomposition terms (E2 to E8) in eq. (3.15) using the best fit parameters.

In Table 3.2, HRF and its decomposition terms (F1 to F5) are calculated on the basis of the observations, the Prediction1 using the best fit parameters to eqs. (3.16) to (3.20) producing reasonable results. It should be noted that here F6 and F7 are neglected and HRF is the sum of F1 to F5. The Eulerian flux (F1), which is driven by the landward residual velocity and the tidally averaged DASSC, is directed landward. Because of the phase difference of 112° between the M2 velocity and the M2 elevation, the Stokes' drift (F2) is also landward directed. F3 is small, and F4 dominates the tidal

pumping. Applying the best fit parameters in eq. (3.19), it is found that the landward positive DASSC gradient is the most important reason for the positive sign of F4 (seaward). The phase lag of DASSC to the M2 velocity (θ_ω) strongly controls the absolute value of F4. F5 accounts for nearly 25% of F1, being mainly attributed to the interaction between the M2 velocity and the M2 elevation. Because of the balance of landward Lagrangian flux (F1+F2) and seaward tidal pumping (mainly in F4), the total flux is towards the land and has a reduced value in the order of $0.1 \text{ kg m}^{-1} \text{ s}^{-1}$.

Table 3.2. The tide- and depth-averaged SSC (E1), HRF and its decomposition terms (F1 to F5) at the observation site. Observation data are listed on the first row. Prediction1 uses the three best fit parameters (DASSC gradient k , resuspension coefficient B , and deposition coefficient D), Prediction2 forces the zero k , representing the non-advection condition, Prediction3 forces the zero k and the half D , representing the finer sediment condition, and Prediction4 forces the zero k and the double D , representing the coarser sediment condition. Positive values of sediment flux denote seaward.

	$k*10^6$ (kg m^{-4})	$B*10^4$ (kg s m^{-4})	$D*10^4$ (s^{-1})	E1 (mg l^{-1})	F1	F2	F3	F4	F5	HRF
Observation				177.6	-0.277	-0.133	0.009	0.358	-0.074	-0.117
Prediction1	-8.8	4.2	1.0	181.7	-0.284	-0.137	0.008	0.432	-0.062	-0.043
Prediction2	0	4.2	1.0	188.8	-0.295	-0.142	0.000	-0.077	-0.064	-0.578
Prediction3	0	4.2	0.5	363.4	-0.590	-0.284	0.000	-0.131	-0.066	-1.071
Prediction4	0	4.2	2.0	90.9	-0.148	-0.071	0.000	-0.064	-0.054	-0.337

3.4. Discussion

3.4.1. Influence of advection

The influence of advection of a horizontal concentration gradient on the DASSC evolution and the HRF can be evaluated by modifying the parameter k in Table 3.1 and eqs. (3.16) to (3.20). In the case of the Jiangsu coast, China, the landward positive DASSC gradient has a pronounced effect. Here advection was excluded by setting $k = 0$, and the DASSC time series and the HRF were calculated by eqs. (3.15) to (3.20). In this way, the system was only driven by local resuspension and deposition.

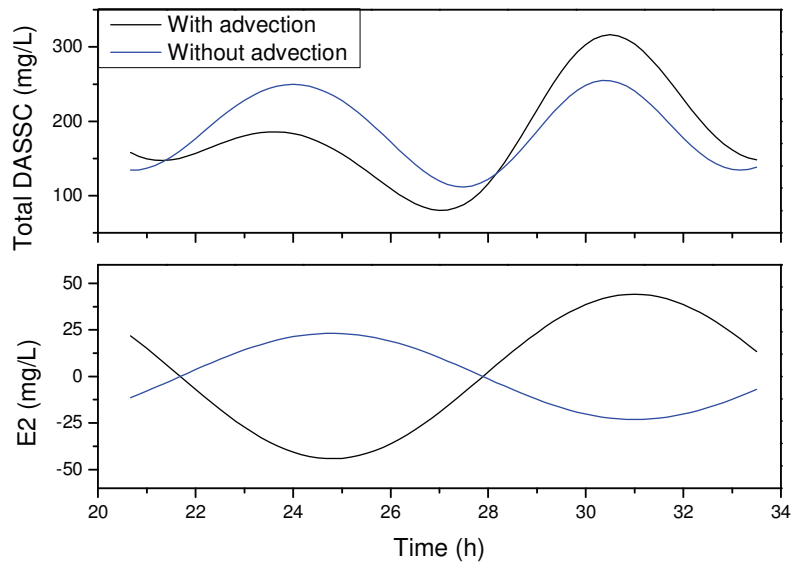


Fig. 3.6. The different responses of DASSC at the observation site to the conditions with and without the effects of advection induced by the horizontal DASSC gradient. The upper panel shows the total DASSC, the lower panel the E2 decomposition term, which contributes most of the advection influence.

The resulting DASSC is compared with the best fit prediction (Fig. 3.6). Without the contributions of advection, the asymmetry of the DASSC during the flood and ebb phases disappears. For the E2 term in eq. (3.15) and Table 3.1, which contributes most of the influence of advection, Fig. 3.6 shows that, when advection is excluded, its variation has only about half of its original amplitude and the phase is inverse.

The tidally averaged DASSC (E1) and each decomposition term of the suspended sediment flux (F1 to F5) are listed in Table 3.2 as Prediction2. Compared with the best fit results (Prediction1), all of these are similar, except for F4, which reduces from seaward to landward from a value of $0.432 \text{ kg m}^{-1}\text{s}^{-1}$ to $0.077 \text{ kg m}^{-1}\text{s}^{-1}$. This landward tidal pumping (F3+F4+F5) and the landward Lagrangian flux (F1+F2) lead to a large landward total flux (HRF = $-0.578 \text{ kg m}^{-1}\text{s}^{-1}$). These results suggest that, at the observation site, advection induced by the landward positive DASSC gradient plays a crucial role in determining the large seaward F4 and, in turn, the nearly balanced total flux.

Traditionally, tidal pumping is suggested to be mainly due to current asymmetry and sediment lag effects (Uncles and Stephen, 1989; Brenon and Le Hir, 1999). However, the above analysis indicates an important influence of horizontal advection. Thus, when applying the empirical decomposition method to observations (eq. (3.1)), care must be taken when interpreting the decomposed terms, especially that of tidal pumping.

3.4.2. Influence of the deposition coefficient

For a given hydrodynamic condition, the Rouse profile of SSC shows that $C_{bed}/\langle C \rangle H$ is strongly depended on W_s . Based on the definition in eq. (3.6), the deposition coefficient D is also mainly controlled by W_s .

There are three important aspects concerning the influence of D . Firstly, it determines the phase lag of DASSC to the forcing factors. The phase lag can be measured by the ratio between the frequency ω_i and the deposition coefficient D (eq. (3.10) and eq. (3.15)). For coarse-grained sediments having high settling velocities, D is sufficiently larger than ω_i to produce a reduced phase lag. Conversely, for fine-grained sediments having low settling velocities, D is much less than ω_i on account of which a large phase lag is produced. The trend from an in-phase response for coarse sediment to an out-of-phase response for fine sediment indicates the importance of the dimensionless scale ω_i/D , which represents the ratio between the time scale of sediment settling and that of the forcing factor variation. This result is consistent with previous studies (Prandle, 1997; Bass et al., 2002; Stanev, et al., 2007; Cheng and Wilson, 2008).

Secondly, the tidally averaged DASSC varies directly with $1/D$ (eq. (3.A1)). Thus, low sediment settling velocities produce high mean concentrations, and vice versa. Equation (15) shows that the amplitudes of the periodic terms (E2 to E8) are proportional to $(\omega_i^2 + D^2)^{1/2}$. This indicates that varying ranges of DASSC are also inversely related to D .

Thirdly, the phase lag affects the tidal pumping flux. The parameters θ_ω and $\theta_{2\omega}$,

which represent the phase lag of SSC to the forcing factors at the M2 and M4 frequencies, respectively, are involved in the formulas of F3 to F5. These formulas indicate that the combinations of these phase lags and the phase of the M2 and M4 velocities and the M2 elevation strongly determine the magnitude of tidal pumping.

Two test experiments (Prediction3 and Prediction4) were carried out based on the no-advection prediction (Prediction2) to study the response of changing D (Table 3.2). Prediction3 and Prediction4 produce a halving and a doubling of D , respectively, but keep the two other parameters the same as in Prediction2, in which the advection is excluded. The lag between DASSC and the current velocity decreases with D (the upper panel of Fig. 3.7), and the response of E6 to its forcing factor of the M2 speed shows the same characteristics (the lower panel of Fig. 3.7). The lower panel also indicates that the amplitude is inversely related to D , but, because of the comparable values of D and ω , the difference in the amplitudes of the three E6 curves is relatively small.

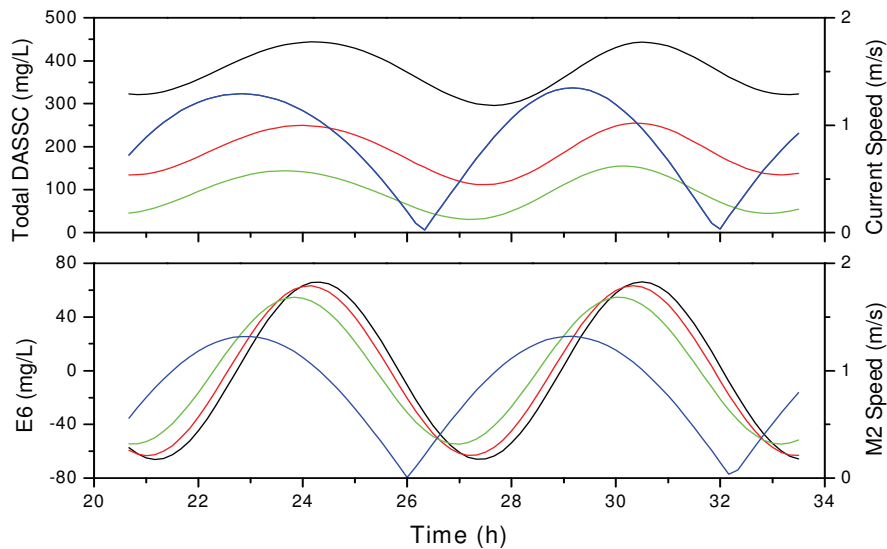


Fig. 3.7. The response of DASSC at the observation site to different deposition coefficients (D). The upper panel shows the total current speed and the total DASSC, the lower panel the M2 tidal current speed and the E6 decomposition term, which is the largest part of the DASSC variation. The black, red, and green curves are associated with Prediction3, Prediction2, and Prediction4 (Table 3.2), respectively. They have a D of $0.5 \times 10^{-4} \text{ s}^{-1}$, $1 \times 10^{-4} \text{ s}^{-1}$, and $2 \times 10^{-4} \text{ s}^{-1}$, respectively. The blue curves show current speeds. Here the effect of advection is excluded.

In Table 3.1, the halving of D results in a doubling of the tidally averaged DASSC (E1) and, consequently, a doubling in the Lagrangian flux (F1+F2). Similarly, the doubling of the D values lead to a halving of the E1, F1 and F2 values. The absolute values of the pumping terms (F4 and F5) are also inversely related to D , but the response of F4 is more pronounced than that of F5. The experiment with a lower D has a higher landward total suspended sediment flux. This indicates that fine grains have more potential to be transported in the landward direction, thereby contributing to grain-size sorting.

3.4.3. Applicable scope of the solution

The analytical solution presented in this paper investigates the responses of suspended sediment in a depth-averaged 1D model to the combination of three basic processes: advection of a horizontal DASSC gradient, local resuspension, and deposition. After reasonable simplification, the three processes are shown to be controlled by the DASSC gradient k , the resuspension coefficient B , and the deposition coefficient D , respectively. Because of its simplicity, the solution can be easily applied to field observations, thereby providing a more comprehensive understanding of DASSC variation and HRF than the empirical methods of Weeks et al. (1993) and Dyer (1997). The solution can be fitted to the observations at a fixed station in a well-mixed and bidirectional tide-dominated environment after the three free parameters (k , B and D) have been calibrated.

However, because of its simplicity some processes have been omitted. For example, in connection with sediment deposition, aggregation and disaggregation have been observed in the course of the tidal cycle (Ellis et al., 2004; Jago et al., 2006). This means that the settling velocity is not constant but variable over the tidal cycle. Furthermore, bed consolidation (Dyer, 1995; Anthony et al., 2010), depth-limited erosion (Sanford and Maa, 2001), and bed sediment availability (Velegrakis et al., 1997; Bass et al, 2002) may complicate the local resuspension simulation. Also,

stratification effects induced by salinity and/or sediment can significantly influence the water and sediment dynamic behavior (e.g., Geyer, 1993; Wang et al., 2005). Thus, suspended sediment is subject to different advection in different water layers, and this shear diffusion caused by the nonlinear interaction of turbulence and advection may play a substantial role in horizontal suspended sediment transport (e.g., Stanev et al., 2007).

The assumption of a constant DASSC gradient k is a lesser problem. Thus, if a spatial DASSC distribution pattern is available from numerical modeling results (Cheng and Wilson, 2008) and/or multi-site observations, this gradient can be parameterized as a trigonometric Fourier series only associated with time. Then, substituting the series and the parameterized velocities and water depths in eq. (3.8), a new solution of eq. (3.9) can easily be obtained. Only when such spatial information is not available, as in the case of single site observations, a constant gradient must be assumed in the present solution, which then provides a first order approximation only. It should also be noted that a constant gradient assumption is not suitable for some environments, for example, the central part of the estuarine turbidity maximum, although it would satisfy the areas on either side of it.

3.5. Conclusions

Simplified analytical solutions for tidal variations of DASSC and HRF have been obtained for a single site based on a depth-averaged 1D model combined with three basic processes: advection of a horizontal DASSC gradient, local resuspension, and deposition. The model is driven by the forcing factors of residual, M2 and M4 current velocities, mean and M2 water depth, and the DASSC gradient. The solution of DASSC consists of eight terms, each of which represent the particular effects of different forcing factors with clear physical meanings, thereby allowing the empirical decomposition terms of HRF to be formulized and directly interpreted.

The solutions have been successfully applied to fit and explain the observations at a

fixed station in a macro-tidal channel located along the Jiangsu coast, China. The results suggest that the M4 DASSC variation is due to resuspension induced by the M2 velocity, and that the M2 DASSC variation is mainly controlled by advection and, in addition, by resuspension induced by the interaction of the M2 and M4 velocities. The horizontal DASSC gradient leads to a large seaward tidal pumping (F4 term), which is offset by the landward Lagrangian flux that results in a reduced landward HRF.

Appendix 3A. Interpretation of eight harmonic terms in the solution of DASSC

The solution of DASSC in eq. (3.15) consists of eight harmonic terms (E1 to E8) with the coefficients shown in Table 3.1, each term corresponding to particular physical processes induced by the forcing factors and their interactions. These factors are residual, M2 and M4 current velocities, mean and M2 water depth, and the DASSC gradient.

E1 is the SSC averaged over depth and tidal cycle:

$$E1 = \overline{\langle C \rangle} = \frac{1}{T} \int_0^T \langle C \rangle dt = \frac{1}{D} (-ku_0 + \frac{1}{2} \frac{B}{h_0} u_1^2) \quad (3.A1)$$

The first term ($-ku_0$) indicates the contribution of horizontal advection by the residual current, causing the averaged DASSC to decrease when the DASSC increases in the direction of the residual velocity, and vice versa. The second term ($Bu_1^2/2h_0$) is the tidally averaged DASSC induced by local resuspension of the M2 current.

E2, E3 and E4 represent the M2 variations of DASSC but with different phases. E2 has the same phase as the M2 velocity (ϕ_1). The first term in A_2 ($-ku_1$) shows an in-phase response of DASSC to the horizontal advection driven by the M2 current, which has been identified by Weeks et al. (1993) as the advective component. The second and third terms are due to the interaction between the residual and the M2 velocity, and that between the M2 velocity and the M2 tidal elevation, respectively.

E3 is induced by the interaction of the M2 and M4 currents and thus with the phase of $(\varphi_2 - \varphi_1)$. E4 demonstrates the interaction between the M2 velocity and the M2 elevation, having the same phase as the M2 elevation (ϕ).

E5 and E6 have the M4 frequency. E5 shows an in-phase response of DASSC to the horizontal advection driven by the M4 current. E6 is the M4 variation of DASSC induced by the M2 current resuspension and represents the local component in the concept of Weeks et al. (1993). E7 and E8 stand for the M6 variation of the DASSC. E7, as in the case of E3, is also due to the M2 and M4 current interaction, but has a triple frequency and the phase of $(\varphi_2 + \varphi_1)$. E8 is another product of the interaction of the M2 velocity and the M2 elevation.

Appendix 3B. Interpretation of the terms F1 to F5 in the solution of HRF

The mechanisms of residual sediment flux can be revealed by the analytical formula of terms F1 to F5. Eq. (3.16) shows that the Eulerian flux F1 is controlled by the residual velocity (u_0) and the tidally averaged DASSC (eq. (3.A1)). Eq. (3.17) shows that the Stokes' drift flux is strongly related to the phase difference between the M2 velocity and the M2 tidal elevation ($\varphi_1 - \phi$) and the amplitude of the M2 tidal elevation. Eq. (3.18) shows that F3, which is induced by the interaction between the tidal elevations and the DASSC, is a second order trivial term, and has less importance for the total flux. The long formula of F4 in eq. (3.19) indicates the complexity of the interaction between velocity and DASSC. The existence of several zero and first order trivial terms in eq. (3.19) suggest the probable importance of F4 to the total flux. This characteristic has been supported by field observations. Su and Wang (1986), Li and Chen (1998), Wu et al. (2001), and Ganju et al. (2005) found that this term is not only dominant in the tidal pumping (F3+F4+F5), but is also important for the total flux. The solution indicates the control of the phase lag of DASSC and the phase differences between tidal current and tidal elevation. The first term in eq. (3.20), which is the only first order trivial term for F5, shows a strong

dependence on the amplitude of the tidal elevation of the M2 tide, the phase differences among the velocity and tidal elevations, and the phase lag of DASSC. The involvement of the DASSC gradient (k) in the formulas of F3 to F5 suggests an impact of horizontal advection on tidal pumping.

4. Scale-dependent Characteristics of Equilibrium Morphology of Tidal Basins along the Dutch-German North Sea Coast

Abstract

Tidal basins can be characterized by two major morphological elements: tidal channels and tidal flats. Some scale-dependent empirical relations have been suggested based on observations in tidal basins of the Dutch and German coast. Thus, the dimensional parameters of channel area and volume are proportional to the 1.5 power of the basin area and tidal prism, respectively, whereas the dimensionless parameters of relative channel area and the ratio between channel volume and tidal prism are both proportional to the square root of basin area (A_b). The coefficients before the power in these relations are of the order of 10^{-5} . In order to provide physical explanations for these relations, a theoretical model and a two-dimensional horizontal numerical model are developed. Based on the concept of uniform equilibrium channel velocity, the channel cross-sectional area is directly proportional to A_b and, when integrating the cross-sectional area in the flow direction, a 1.5 power relationship between the channel volume and A_b is obtained. Due to the parameters expressing the characteristic basin depth and the ratio of channel depth to the characteristic depth, which are confirmed to be scale-insensitive in both the numerical model and in field observations, the channel area is also proportional to $A_b^{1.5}$. Theoretical expressions suggest the same order for the coefficients before the power as found in empirical studies. In the numerical model, the same type of scaling relations are illustrated, and the morphological response of changing grain size and tidal amplitude can be successfully predicted by the theoretical model.

4.1. Introduction

Tidal inlets and tidal basins are of importance for economic reasons, e.g., by providing natural harbors, inland waterways, recreational areas, and land resources,

and for ecological and environmental reasons (e.g., for marine invertebrates, fish, birds) (Reise, 2001). Due to the impacts of sea-level rise (SLR) resulting from global warming (IPCC, 2007) and of human activity (e.g. land reclamation, harbor construction), a thorough understanding of the characteristics of tidal basin morphology is essential in order to predict morphodynamic responses to these changes and to make appropriate management decisions (Flemming and Bartholomä, 1997; Lee et al., 1999; van Goor et al., 2003; FitzGerald et al., 2008).

In the past, research on tidal inlets mostly focused on the concept of equilibrium cross-sectional area (A), which was suggested to have a power law relationship with tidal prism (P), the so-called P - A relationship (O'Brien, 1969; Bruun, 1978; Gao and Collins, 1994; D'Alpaos et al., 2010). However, from a planimetric point of view, the most striking feature of tidal basin morphology is that it consists of two major elements, namely channels and tidal flats (van Dongeren and de Vriend, 1994), where channels are defined as the area below the mean low-water level (MLW), and tidal flats comprise the area between MLW and the mean high-water level (MHW).

To describe the morphology of this two-element system in a quantitative but simple way, four basic parameters have been proposed: tidal channel area (A_c), tidal flat area (A_f), average channel depth relative to mean sea level (MSL) (D_c), and average tidal flat elevation relative to MHW (D_f). From these basic parameters, a number of other physical parameters can be deduced. For example, the total area of the basin can be expressed as $A_b = A_c + A_f$, and the tidal prism as $P = 2 A_c * a + A_f * D_f$, where a is the tidal amplitude, $V_c = A_c * D_c$ is the channel volume below MSL, and $V_f = A_f * D_f$ is the water volume stored over the flats. These morphological parameters have been used to illustrate the equilibrium morphology and tidal asymmetry in tidal basins and estuaries (Friedrichs and Aubrey, 1988; Dronkers, 1998; Wang et al., 2002).

Geomorphological and sedimentological systems respond on specific spatial scales (Dodds and Rothman, 2000). The scaling relationship or scaling law is usually characterised by a power-law relationship between the geomorphological or sedimentological parameter of a basin and its area A_b . An example is Hack's law for

terrestrial drainage basins (Hack, 1957) that suggests that the main stream length is proportional to A_b^h where h is the so-called Hack's exponent. The application and evaluation of Hack's scaling law to submarine basins and tidal flats have been investigated through field observations and theoretical analyses (Marani et al., 2003; Novakowski et al., 2004; Rinaldo et al., 2004; Hood, 2007; Straub et al., 2007). In this context, the P - A relationship is also a kind of scaling law because P is strongly dependent on basin area (Williams et al., 2002).

For the parameters of tidal basin morphology introduced above (e.g., A_c , A_f , D_c , D_f), the question arises whether these also follow similar scaling laws. Based on field observations of tidal basins along the Dutch and German North Sea coast, some empirical relationships between morphological parameters and spatial scale factors have been recognized (Renger and Partenscky, 1974; Eysink, 1990), (c.f. section 3 for details). However, to our knowledge, intrinsic physical explanations for these scale-dependent characteristics in theoretical and numerical models are still lacking.

Studies on the morphodynamics of tidal basin systems have made use of both theoretical and numerical methods (de Swart and Zimmerman, 2009). In this context, Friedrichs (1995) and Friedrichs and Aubrey (1996) applied the concept of spatial uniform stability bed shear stress (or current velocity) in tidal channels and on tidal flats, to establish an analytical expression of channel cross-sectional areas and tidal flat profiles. Based on a similar concept of equilibrium channel velocity, Allen (2000) suggested a state of dynamic equilibrium in tidal marsh systems where the total channel cross-sectional area increases linearly with tidal drainage area, a concept which was validated by observations (Lawrence et al., 2004). One-dimensional models have been used to investigate the evolution and equilibrium of tidal channel and tidal flat morphology both analytically (Schuttelaars and de Swart, 2000; Pritchard and Hogg, 2003) and numerically (Lanzoni and Seminara, 2002; Todeschini et al., 2008). With the development of numerical modeling technology (Latteux, 1995; Lesser et al., 2004; Roelvink, 2006), long-term morphodynamics of tidal basin systems have been studied by means of two- and three-dimensional, process-based

models (Cayocca, 2001; Fortunato and Oliveira, 2004; Ganju et al., 2009), especially in the Dutch coastal region (Wang et al., 1995; Dastgheib et al., 2008; van der Wegen and Roelvink, 2008; van der Wegen et al., 2008; Dissanayake et al., 2009).

In this paper, the scale-dependent characteristics of equilibrium morphology of Dutch and German tidal basins are investigated. The study commences by introducing some empirical scaling relations of tidal basin morphology and then proceeds with an evaluation of theoretical and numerical models with the aim of providing physical explanations for the scaling relations.

4.2. Study area

A number of tidal basins fringe the Dutch and German North Sea coastlines. There are, generally, two types of tidal basins in this region: the back-barrier tidal basins (e. g., Wadden Sea, stretching for 500 km from Netherlands in the west to Denmark in the northeast covering the German North Sea coast) and estuarine tidal basins (e. g., tidal basins in Western Scheldt estuary, southern Netherlands, and in the Elbe river estuary, inner German Bight) (Dronkers, 2005). Both types of tidal basins are lined by mainland dikes, and are separated by drainage divides or barrier islands and sandy shoals on which tidal channel networks develop that are separated by largely non-vegetated or bare intertidal flats exposed to the air during the ebb phase. The largest part of the basins is occupied by sandy sediment, the rest comprising fine-grained material (Flemming and Davis, 1994; Oost and de Borer, 1994). Within the basins, the tides are the predominant forcing factor, locally generated waves forming a subordinate component (Nyandwi and Flemming, 1995; Krögel and Flemming, 1998). Fresh water discharge is very small compared with the large tidal prisms (Toffolon and Crosato, 2007). According to Davies (1964), the region is classified as being mesotidal (M2 tidal range 2 to 4 m).

4.3. Empirical model

Based on field observations of tidal basin bathymetry along the Dutch and German coast, some empirical scaling relationships have been suggested for morphological parameters. Thus, for German Bight inlet systems, Renger and Partenscky (1974) found that the channel area A_c was proportional to the 1.5 power of basin area A_b :

$$A_c = 2.5 \times 10^{-5} A_b^{1.5} \quad (4.1)$$

The relative area of tidal channels in a basin can be derived from:

$$\frac{A_c}{A_b} = 2.5 \times 10^{-5} \sqrt{A_b} \quad (4.2)$$

Eq. (4.2) shows that the dimensionless parameter of relative channel area is scale-dependent, being proportional to the square root of the dimensional basin area. This relationship was used in the morphological model of van Dongeren and de Vriend (1994) for the Dutch Wadden Sea.

Another empirical relation, which was suggested by Eysink (1990), is that between channel volume V_c and tidal prism P :

$$V_c = cP^{1.5} \quad (4.3)$$

where c is an empirical coefficient. For different tidal basins in the Netherlands, the calibration of coefficient c revealed that it was dependent on the size of tidal flats, ranging from $8 * 10^{-5}$ in the Dutch Wadden Sea region, to $6.5 * 10^{-5}$ in the Western Scheldt. Eq. (4.3) suggests that channel volumes are proportional to the 1.5 power of tidal prisms.

Similar to the transformation of eq. (4.1) to (4.2), eq. (4.3) can be rewritten as:

$$\frac{V_c}{P} = cP^{0.5} = c\sqrt{DA_b} \quad (4.4)$$

where D is a characteristic depth of the basin, defined by: $D = P / A_b$. Eq. (4.4) demonstrates that the dimensionless parameter expressed by the ratio between channel

volume and tidal prism is scale-dependent, being proportional to the square root of the dimensional basin area if D is independent of scale.

Table 4.1. Observed tidal basin morphological parameters in the North Frisian Wadden Sea of Schleswig-Holstein, Germany (modified from Hofstede (2002))^a

Basin Name	a (m)	A_b (km ²)	A_c/A_b	D_c (m)	D_f (m)	D (m)	D_c/D	P (km ³)	V_c/P	V_f/P
Tümlauer Bucht	1.51	6.3	0.02	2.51	0.91	0.95	2.64	0.006	0.04	0.94
Schatzkammer	1.56	17.1	0.05	2.19	1.20	1.29	1.70	0.022	0.08	0.89
Hooger Loch	1.31	17.8	0.06	2.67	1.10	1.20	2.23	0.021	0.14	0.86
Neufahrwasser	1.56	37.3	0.12	2.98	1.41	1.62	1.84	0.060	0.22	0.77
Flackstrom	1.62	45.4	0.18	4.61	1.43	1.76	2.63	0.080	0.48	0.67
Wesselburener Loch	1.55	66.1	0.20	4.42	1.34	1.68	2.63	0.111	0.51	0.64
Rummelloch-West	1.34	83.7	0.21	4.45	1.44	1.70	2.62	0.142	0.55	0.67
Süderaue	1.42	190.3	0.51	5.32	1.60	1.94	2.74	0.370	1.18	0.40
Piep	1.64	203.0	0.27	6.65	1.57	2.04	3.26	0.414	0.88	0.56
Norderaue	1.35	245.2	0.39	5.60	1.73	2.09	2.68	0.513	1.03	0.51
Hörnum Tief	1.05	290.2	0.53	3.72	1.50	1.82	2.05	0.528	1.08	0.39
Lister Tief	0.93	402.3	0.48	3.44	1.05	1.48	2.31	0.597	1.12	0.36

^a where a is the tidal amplitude, A_b is the basin area, A_c is channel area, D_c is mean channel depth below MSL, D_f is the mean tidal flat elevation below MHW, D is the characteristic depth of the basin ($= P/A_b$), P is the tidal prism, V_c is the channel volume below MSL, and V_f is the tidal water storage over the tidal flat.

The morphological parameters in Table 4.1 have been calculated using observational data from the tidal basins of the North Frisian Wadden Sea in Schleswig-Holstein (located along the northern part of the German North Sea coast) as published in Hofstede (2002). The largest tidal basin, the “Hever”, has been excluded in the present analysis due to remarkable deviations in the empirical relations, which suggests that this large tidal basin has probably not yet reached an equilibrium state (Gao, 2008). In terms of these data, the same type of scaling relations were found between the relative area of channels (A_c/A_b) and the ratio between channel volume and tidal prism (V_c/P) with basin area and between channel volume (V_c) and tidal prism (P) (Figure 4.1):

$$\frac{A_c}{A_b} = 2.59 \times 10^{-5} \sqrt{A_b} \quad (4.5)$$

$$V_c = 4.70 \times 10^{-5} P^{1.5} \quad (4.6)$$

$$\frac{V_c}{P} = 6.54 \times 10^{-5} \sqrt{A_b} \quad (4.7)$$

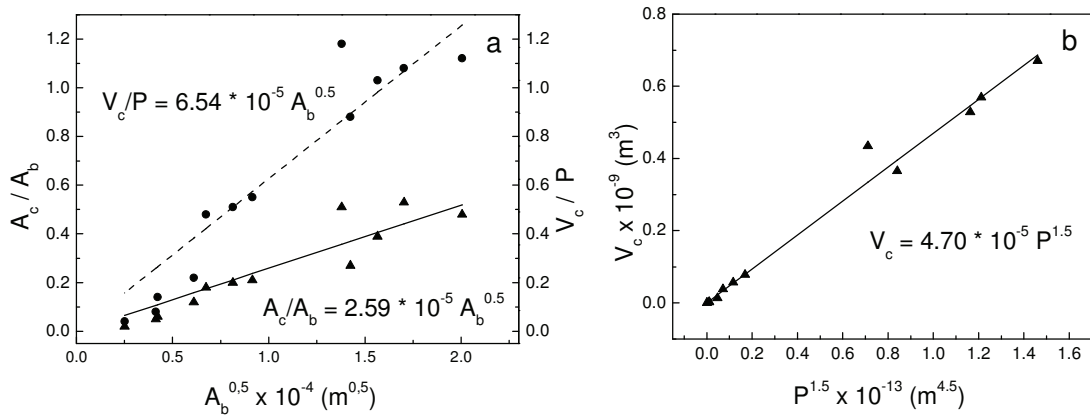


Figure 4.1. The morphological scaling relationships on the basis of observations in the North Frisian Wadden Sea of Schleswig-Holstein. (a) Relations between relative channel area (A_c/A_b), the ratio between relative channel volume and tidal prism (V_c/P) and basin area (A_b); (b) Relation between channel volume and tidal prism. The regression equations are shown on the figures.

The coefficient before the power in eq. (4.5) is very similar to that in eq. (4.2). Table 4.1 shows that the characteristic depth of the basin D and the ratio between channel depth and characteristic depth D_c/D are not clearly correlated with basin area, which suggests that they are scale-insensitive.

In summary, the empirical models indicate that the dimensional parameters of channel area and volume are proportional to the 1.5 power of the basin area and tidal prism, respectively, and that the dimensionless parameters of relative channel area and the

ratio between channel volume and tidal prism are both proportional to the square root of basin area. The values of coefficients before the power in these relations are in the order of 10^{-5} .

These empirical relationships raise a number of questions. Why are there power-law relations? Why are the powers 1.5 and 0.5 so prominent? And why are the values of coefficients before the power in the order of 10^{-5} ? On the other hand, it may be conjectured that there could be some scale-independent characteristics in tidal basin systems that produce these scale-dependent relations. To answer these questions, the physics behind the morphology must be understood.

4.4. Theoretical model

A theoretical model based on the earlier approaches of Friedrichs (1995) and Allen (2000) has been constructed to reveal the physical mechanisms of the empirical morphological scaling characteristics. The first assumption is that, in tidal basins that are in an equilibrium state, there is a stability shear stress (τ_s) which tends to be uniform throughout the tidal channels and which is necessary to just maintain a zero gradient in net along-channel sediment transport (Friedrichs, 1995). This stability shear stress is related to the peak current (U_p) velocity by the Manning formula for open channels (Henderson, 1966):

$$U_p = \frac{1}{n} \sqrt{\frac{\tau_s}{\rho g}} h_R^{1/6} \quad (4.8)$$

where g is the acceleration due to gravity, n is the Manning friction coefficient, which depends on the bed condition, and h_R is the hydraulic radius of the channel. In wide channels, h_R is approximately equal to the mean water depth. This equation shows that the peak velocity is directly proportional to $\tau^{0.5}$, while being weakly related to the channel depth. For the sake of simplicity, the stability uniform peak velocity is used instead of the stability shear stress (cf. Friedrichs and Aubrey, 1996; and Dronkers, 2005).

If the channel velocity is assumed to be sinusoidal, the stability peak velocity can be transformed to the stability uniform tide-averaged velocity, called equilibrium velocity (U_{eq}) by Allen (2000):

$$U_{eq} = \frac{2}{\pi} U_p \quad (4.9)$$

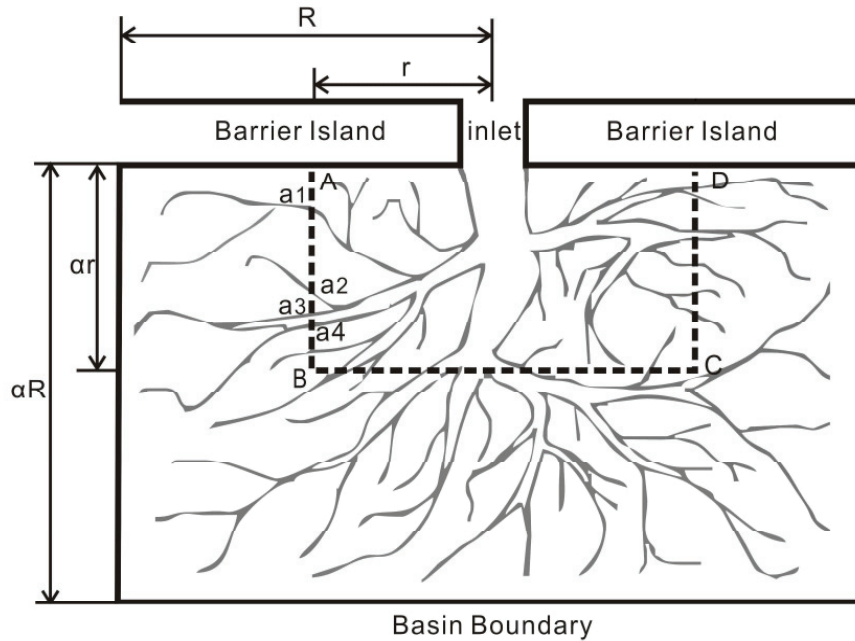


Figure 4.2. Definition diagram of the morphology of an idealized back-barrier tidal basin used in the theoretical model. Gray lines depict the tidal channels, and transect ABCD cuts channels with cross-sectional areas a_1, a_2 , etc.

In the present study an idealized back-barrier tidal basin has been constructed (Figure 4.2), which is similar to typical tidal basins found in the Dutch and German Wadden Sea. The tide enters and leaves the basin only through the inlet between the barrier islands. The half-width of the basin is defined as R , and the length is αR , where the coefficient α indicates the basin shape. The transect ABCD, with a half-width of r , has the same shape as the basin, and cuts channels 1, 2, ..., n , with the cross-sectional area below MSL perpendicular to the flow direction of a_1, a_2, \dots, a_n , respectively. The total discharge during a tidal cycle (Q) through these channels can be estimated by means of the equilibrium velocity, which is taken to be uniform in all channels:

$$Q = \frac{T}{2} (U_{eq} a_1 + U_{eq} a_2 + \dots + U_{eq} a_n) = \frac{T}{2} U_{eq} a_t \quad (4.10)$$

where T is the tidal period, and $a_t = a_1 + a_2 + \dots$, a_n is the total cross-sectional area measured along transect ABCD. If the water on a tidal flat enters and leaves through the nearest adjacent tidal channel, the tidal discharge can be expressed as the tidal prism over the area outside the transect ABCD (Allen, 2000). When assuming a constant characteristic depth in the basin ($D = P / A_b$), this discharge is:

$$Q = 2\alpha(R^2 - r^2)D \quad (4.11)$$

Eliminating Q in eq. (4.10) and (4.11) yields:

$$a_t = 4\alpha(R^2 - r^2)D / TU_{eq} \quad (4.12)$$

By integrating eq. (4.12), and considering that U_{eq} remains almost constant along the equilibrium state channel, which is supported by observations (Friedrichs, 1995) and numerical modelling (Todeschini et al., 2008), the total channel volume below the MSL can be written as:

$$V_c = \int_0^R a_t \cdot dr = \frac{8\alpha D}{3TU_{eq}} R^3 \quad (4.13)$$

Because the tidal prism of the basin $P = 2 \alpha D R^2$, the relationship between the channel volume and the tidal prism can be established as:

$$V_c = \frac{2\sqrt{2}}{3TU_{eq} \sqrt{\alpha D}} P^{1.5} \quad (4.14)$$

This equation is the theoretical expression of eq. (4.3), and demonstrates the 1.5 power relation between the channel volume and tidal prism.

With the basin area $A_b = 2 \alpha R^2$, the theoretical expression of relations between channel area and basin area in eq. (4.1) and (4.2) can be obtained, assuming that the channel area is equal to the ratio between the channel volume and the mean channel depth D_c :

$$A_c = \frac{V_c}{D_c} = \frac{2\sqrt{2}}{3TU_{eq}\sqrt{\alpha}(D_c/D)} A_b^{1.5} \quad (4.15)$$

$$\frac{A_c}{A_b} = \frac{2\sqrt{2}}{3TU_{eq}\sqrt{\alpha}(D_c/D)} \sqrt{A_b} \quad (4.16)$$

The ratio between channel volume and tidal prism in eq. (4.4) can also be written as:

$$\frac{V_c}{P} = \frac{2\sqrt{2}}{3TU_{eq}\sqrt{\alpha}} \sqrt{A_b} \quad (4.17)$$

Eqs. (4.14) to (4.17) provide the physically-based expressions for the same scaling relations expressed in eqs. (4.1) to (4.7). The consequent question now is whether the coefficients before the power of P or A_b in eqs. (4.14) to (4.17) are kept constant through different scales as observed in the empirical relations. These coefficients include five variables: T , U_{eq} , α , D , and D_c/D . The tidal period is the same for the same tidal regime as, for example, the dominant M2 tide along the Dutch and German coasts. The equilibrium velocity is related to the grain size of the bed sediment, the tidal range, and the tidal asymmetry (Friedrichs, 1995), none of which are directly linked to the basin scale. Bruun (1978) also suggested that the peak velocities in tidal inlets tend to remain in the range between 0.9 and 1.2 m/s. Therefore, we assume that U_{eq} is scale-independent or not sensitive to changes in scale. The shape of tidal basins (α) at different scales is still not clear and will be discussed later, but we assume that, in the same region, the general basin shape will not change very much, as observed in self-similarity or fractal theory. As a result, this leaves the question about the scale-dependency of the last two variables to be answered, i.e. the characteristic depth of a basin D and the ratio between channel depth and characteristic depth D_c/D . The observational values listed in Table 4.1 and numerical modelling results presented in the next section illustrate that these final two variables are both scale-insensitive. The above analysis thus confirms that the theoretical equations are in agreement with the empirical equations.

The ratio between the coefficient before $P^{1.5}$ in eq. (4.14) and that before $A_b^{0.5}$ in eq.

(4.16) is $D_c/D^{1.5}$, and the ratio between the coefficient before the $A_b^{0.5}$ in eq. (4.17) and that in eq. (4.16) is D_c/D . If we use typical values for these five variables, e.g., T in the order of $4 \cdot 10^4$ s for the M2 tide, U_{eq} in the order of 1 m/s (Bruun, 1978; Allen, 2000), and α , D and D_c/D in the order of 1, the coefficients before the power of P or A_b in eq. (4.14) to (4.17) are in the order of 10^{-5} , which is consistent with the empirical values.

4.5. Numerical model

4.5.1. Methods and Setting

The two-dimensional depth-averaged numerical modeling of tidal basin morphology in response to varying spatial scales was carried out by using the Delft3DTM software package. Delft3DTM can simulate hydrodynamic and morphodynamic changes at different time scales, and has been utilized and validated widely in different coastal environments (Temmerman et al., 2005; Tonnon et al., 2007; Edmonds and Slingerland, 2010), including tidal basins in Dutch and German estuaries (van der Wegen and Roelvink, 2008; van der Wegen et al., 2008) and Wadden Sea (Marciano et al., 2005; Dastgheib et al., 2008; Dissanayake et al., 2009).

In the model, the depth-averaged, nonlinear shallow-water equations are derived from the three-dimensional Reynolds-averaged Navier-Stokes equations for incompressible free surface flow. Only tidal forcing is considered, vertical velocities, Coriolis force, density differences, and wind and waves being neglected in accordance with other long-term morphological modeling approaches (Dastgheib et al., 2008; van der Wegen and Roelvink, 2008; van der Wegen et al., 2008; Dissanayake et al., 2009). The detailed description of the Delft3DTM flow model can be found elsewhere (Lesser et al., 2004; van der Wegen and Roelvink, 2008). Sediment transport was calculated by the approach of van Rijn (see Delft3DTM flow manual for a full reference) for non-cohesive sands. For morphological updatings, the "online" approach suggested by Roelvink (2006) was adopted, which speeds up bed adjustments by multiplying the

bed sediment flux in each time step by a morphological scale factor (MF). This method has in the past been successfully used with a typical MF in the order of 100 (Dastgheib et al., 2008; van der Wegen and Roelvink, 2008; van der Wegen et al., 2008; Dissanayake et al., 2009; Ganju et al., 2009; Edmonds and Slingerland, 2010). In the present model, an MF of 60 was taken.

Table 4.2. Numerical modelling results for tidal basins with different scales and shapes after a 60 year simulation ^a

No.	A_b (km ²)	α	A_c/A_b	D_c (m)	D_f (m)	D (m)	D_c/D	P (km ³)	V_c/P	V_f/P
Case a	21.3	0.67	0.22	3.02	1.87	2.12	1.42	0.05	0.31	0.69
Case b	32.0	1	0.25	3.15	1.85	2.13	1.47	0.07	0.36	0.65
Case c	48.0	1.5	0.28	3.52	1.81	2.14	1.64	0.10	0.46	0.61
Case d	48.0	0.67	0.30	3.42	1.91	2.24	1.53	0.11	0.46	0.59
Case e	72.0	1	0.33	3.66	2.00	2.33	1.57	0.17	0.52	0.57
Case f	108.0	1.5	0.42	4.02	2.13	2.46	1.63	0.24	0.63	0.53
Case g	108.0	0.67	0.43	3.97	2.10	2.48	1.60	0.27	0.68	0.49
Case h	162.0	1	0.48	4.51	2.19	2.59	1.74	0.42	0.84	0.44
Case i	243.0	1.5	0.58	4.85	2.23	2.68	1.81	0.65	1.05	0.35

^a where α is the ratio between the basin length and its half width defined in Figure 4.2. All the cases are simulated with an initial water depth of 1.5 m in the basin, a tidal amplitude of 1.5 m, and a grain size of 0.15 mm.

Nine cases, each having a different spatial scale, were constructed for the numerical modeling exercise (case a to i, in Table 4.2). In agreement with the shapes of the tidal basins in the Wadden Sea region, each case resembles the idealized back-barrier tidal basin used in the theoretical model (cf. Figure 4.2). The areas for a single basin increase by a factor of 12, from 21.3 to 243 km² from case a to i, covering the main data range used for the regression by Renger and Partenscky (1974). In order to investigate the contributions of shape factor, case c and d, and case f and g were designed to have the same basin areas but different shape factors.

Case e is taken as the reference case, as it has an intermediate size of 72 km², which is close to that of the Otzum tidal catchment between Spiekeroog and Langeoog islands

in the German Wadden Sea. The modeling domain, bathymetry and grids of case e are shown in Figure 4.3a where three tidal basins are bounded by a chain of barrier islands interrupted by three inlets connecting to the open sea, each basin having a width of 12 km and a length of 6 km. The initial depth of the basins was set at a constant value of 1.5 m, which equals the M2 tidal amplitude marking the outer North Sea alongshore boundary.

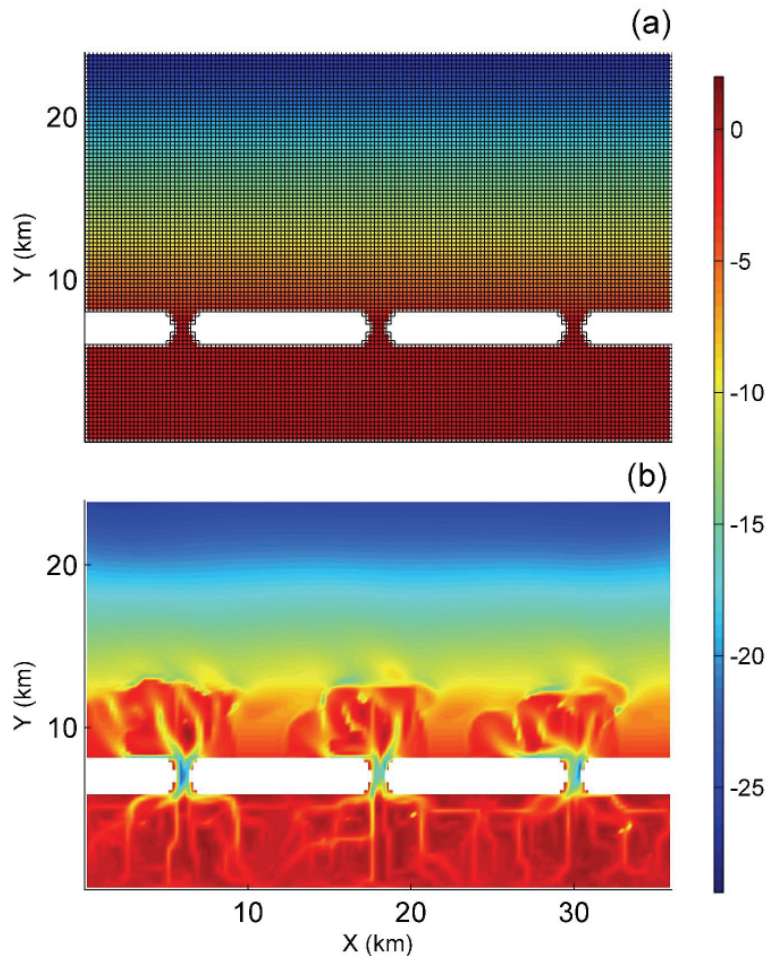


Figure 4.3. (a) The initial bathymetry and grid of the reference case e in Table 4.2; (b) The final bathymetry map of case e after a 60 year simulation. Color bar denotes the bed elevation (m).

This initial bathymetry defines the basin at the depth of MLW, which is the boundary separating tidal channels and tidal flats. In the outer area, water depth progressively increases from 3 m off the barrier islands to 25 m along the northern open sea boundary. A representative mean bed sediment grain size of 0.15 mm, as found in the

Otzum tidal catchment (Flemming and Ziegler, 1995), was adopted in the model. The seaward boundary in the north was a water-level boundary with an M2 tidal amplitude of 1.5 m, which approximates the spring tidal amplitude in the East Frisian Wadden Sea (Flemming and Davis, 1994). The two lateral boundaries were defined as Neumann boundaries, allowing the alongshore velocity and water level to develop without disturbance (Dastgheib et al., 2008; Dissanayake et al., 2009). The other eight cases have the same initial and boundary conditions, only the modelling domain being changed with different areas and/or shape factors. The characteristics of the basins in these cases are shown in Table 4.2.

Because the characteristic time scale for generating equilibrium conditions in the tidal basins of the Wadden Sea has been suggested to be 30 years (van Dongeren and de Vriend, 1994), all the model cases were simulated for a 60 year period to make sure that the system approached equilibrium. The temporal evolution of some characteristic morphological parameters was used to examine the equilibrium state of the system.

4.5.2. Results

Two major parameters, namely the relative area of channels (A_c/A_b) and the ratio between channel depth and characteristic basin depth (D_c/D), were chosen for the equilibrium state examinations. Figure 4.4 shows the temporal evolution of these two parameters in cases a, e, and i (cf. Table 4.2), which have the minimum, intermediate, and maximum areas, respectively. Both parameters approach stable values after the 60 year simulation, indicating that the basin systems reached equilibrium states. The results also indicate that the time needed for equilibrium is related to the spatial scale, i.e. the larger the basin, the longer the time to reach equilibrium. It is interesting to note that this has also been suggested for fluvial systems (Dade and Friend, 1998).

The 60 year bathymetry modeling of the whole domain in the reference case e is illustrated in Figure 4.3b, which shows that the tidal basins are filled with sediment accompanied by the formation of dendritic tidal channels and tidal flats with ebb tidal

deltas forming on the seaward side of the inlets. The final tidal basin morphology for all nine cases is illustrated in Figure 4.5. It can be seen that the general aspects are in accordance with that of case e. The bed elevation range increases with the basin area from case a to i, suggesting that larger basins have deeper channels.

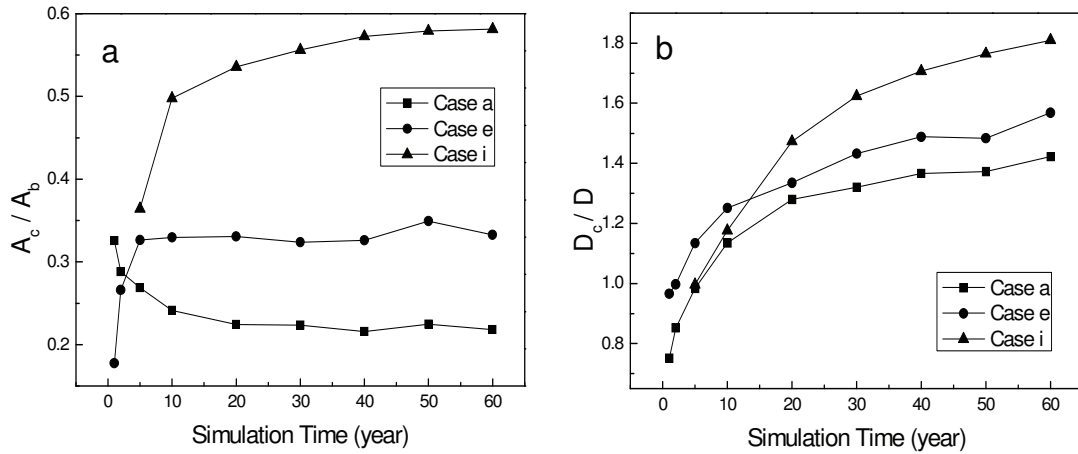


Figure 4.4. Temporal evolution of the relative area of channels (A_c/A_b) and the ration between channel depth and characteristic basin depth (D_c/D) in case a, e, and i in Table 4.2, which have the minimum, intermediate, and maximum area, respectively.

The morphological parameters for the final states of all cases are illustrated in Table 4.2. It can be seen that some parameters are strongly scale-dependent, but that others are scale-insensitive. With basin area and tidal prism increasing by an order of magnitude, respectively, the relative area of channels (A_c/A_b) and the ratio between channel volume and tidal prism (V_c/P) increase by a factor of 2.64 and 3.39, respectively. The two important pending parameters in the theoretical model, i.e. the characteristic depth of the basin D and the ratio between channel depth and characteristic depth D_c/D , are seen to be more or less scale-insensitive, only increasing by 26 % and 27 % from the smallest to the largest basin, respectively. The mean channel depths D_c and tidal flat depths D_f increase by 61 % and 19 %, respectively. In summary, Table 4.2 indicates that with basin area and tidal prism as controlling parameters, A_c/A_b and V_c/P are pronounced scale-dependent, whereas D , D_c/D and D_f are relatively scale-insensitive.

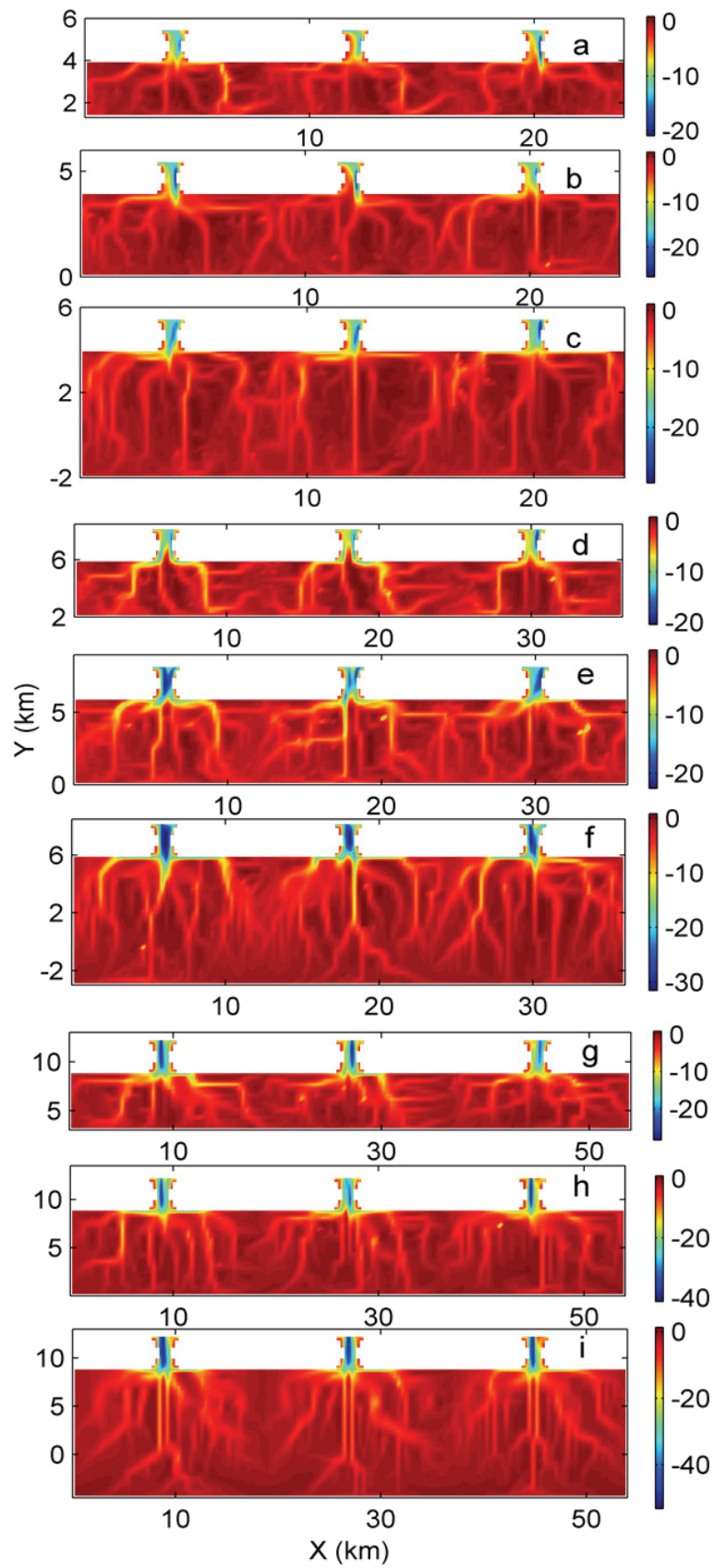


Figure 4.5. The final bathymetry of the tidal basins after a 60 year simulation; (a) to (i) correspond to the cases a to i in Table 4.2, respectively. Color bar denotes the bed elevation (m).

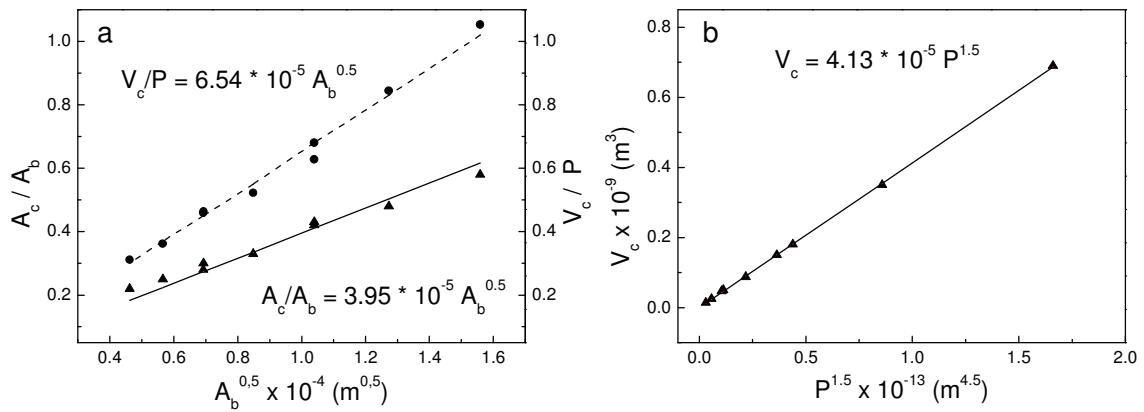


Figure 4.6. The morphological scaling relations in numerical modeling results. (a) The relations between the relative channel area (A_c/A_b), the ratio between relative channel volume and tidal prism (V_c/P) and the basin area (A_b); (b) The relation between channel volume and tidal prism. The regression equations are shown on the figures.

The morphological relations demonstrated in the empirical equations (4.1) to (4.7) and in the theoretical equations (4.14) to (4.17) are reproduced in Figure 4.6 using the numerical modeling results. Regression equations of the numerical results confirm the same type of power-law relations predicted by both empirical and theoretical models:

$$\frac{A_c}{A_b} = 3.95 \times 10^{-5} \sqrt{A_b} \quad (4.18)$$

$$V_c = 4.13 \times 10^{-5} P^{1.5} \quad (4.19)$$

$$\frac{V_c}{P} = 6.54 \times 10^{-5} \sqrt{A_b} \quad (4.20)$$

An interesting finding is that the basin shape factor plays a very minor role in the scaling of morphological parameters. With the same basin area (48 km^2), A_c/A_b in case c is only 7 % smaller than in case d, and V_c/P in case c is practically identical to that in case d. Corresponding similarities also exist for case f and g, A_c/A_b and V_c/P in case f being 2 % and 8 % smaller than in case g, respectively, the shape factor being 1.5 for case c and f and 0.67 for case d and g. The good correlations obtained when only

considering the influence of basin area (Figure 4.6) also suggests that the basin morphology is not directly controlled by their shapes.

Table 4.3. Sensitivity analysis of the numerical modelling of tidal basins ^a

No	I.D. (m)	<i>a</i> (m)	G.S. (mm)	A_c/A_b	D_c (m)	D_f (m)	D (m)	D_c/D	P (km ³)	V_c/P	V_f/P
Case e1	1.00	1.00	0.15	0.38	2.56	1.48	1.68	1.53	0.12	0.59	0.54
Case e2	2.00	2.00	0.15	0.29	4.89	2.47	2.92	1.67	0.21	0.49	0.60
Case e3	1.00	1.50	0.15	0.32	3.83	2.05	2.35	1.63	0.17	0.52	0.60
Case e4	2.00	1.50	0.15	0.35	3.70	1.94	2.31	1.60	0.17	0.56	0.55
Case e5	1.50	1.50	0.10	0.34	3.76	1.97	2.32	1.62	0.17	0.56	0.56
Case e6	1.50	1.50	0.20	0.33	3.46	2.09	2.39	1.44	0.17	0.48	0.58

^a where I.D. is the initial water depth below MSL in the basins, and G.S. is the mean grain size. These sensitivity analyses are based on the reference case e in Table 4.2, the basin area, basin shape, and simulation time being the same as in case e.

4.5.3. Sensitivity analysis

A series of sensitivity analyses were carried out in order to evaluate the influences of the initial and boundary conditions based on the reference case e, including tidal amplitude, initial basin depth, and bed sediment grain size (Table 4.3). In case e1 and e2 a tidal amplitude of 1 and 2 m, respectively, was chosen, the initial basin depth changing with tidal amplitude. Case e3 and e4 have an initial basin depth of 1 and 2 m, respectively, with a constant tidal amplitude of 1.5 m. Grain size effects are tested in case e5 and e6, using a mean grain size of 0.1 and 0.2 mm, respectively.

The morphological parameters of the sensitivity analysis are shown in Table 4.3. With respect to the influence of tidal amplitude, the larger amplitude in case e2 produces deeper channels, deeper tidal flats and also greater characteristic depths, accompanied by a significantly smaller channel area and volume, but only a small increase in D_c/D . In cases e3 and e4, the changes in all parameters remain small. A_c/A_b and V_c/P in case e3, which has a smaller initial depth, are slightly less than those in case e4, while D , D_f , D_c and D_c/D are slightly larger in case e3, indicating an insensitivity to the initial

depth. The coarser sediment in case e6 causes reduced erosion of channels but a deepening of the tidal flats, inducing a slightly deeper D but a more pronounced decrease in D_c/D . A_c/A_b does practically not respond to changes in grain size, although the development of channel volume is significantly inhibited by the coarser sediment.

4.6. Discussion

4.6.1. Comparison of empirical, theoretical and numerical modeling results

All the empirical, theoretical and numerical models produce scale-dependent relations with the same power of 0.5 or 1.5 when comparing eq. (4.2), (4.5), (4.16) and (4.18) for A_c/A_b , eq. (4.3), (4.6), (4.14) and (4.19) for V_c , and eq. (4.7), (4.17) and (4.20) for V_c/P . The coefficients before the power are all in the same order of 10^{-5} . The relative larger scatters of the observational data in the empirical model in Figure 4.1 than in the numerical modeling results in Figure 4.6 can be attributed to the different tidal range and sediment grain size conditions.

The theoretical model was associated with the assumption that the two parameters D and D_c/D were scale-insensitive. This is confirmed by observations in the North Frisian Wadden Sea of Schleswig-Holstein (Table 4.1) and the numerical modeling results (Table 4.2). Eq. (4.8) indicates that the velocity is proportional to $D_c^{1/6}$ with the condition of having the same shear stress, a 61% increase in D_c over the scale range used in the numerical model (Table 4.2), and only inducing an 8% increase in velocity. The observations in the North Frisian Wadden Sea of Schleswig-Holstein (in Table 4.1) also suggest that D_c is not strongly related to basin area. The small influence of channel depth supports the assumption that a uniform peak stability velocity is superior to shear stress in the theoretical model.

The results from the sensitivity analysis on the influence of grain size in the numerical modeling can be explained by theory. As U_{eq} is related to the sediment critical shear stress (Friedrichs, 1995), it is assumed that the ratio between U_{eq} for 0.2 mm and that for 0.1 mm is equal to the ratio of the threshold velocities of these sediments. Based

on the simple formula of Miller et al. (1977), this ratio is estimated at 1.22. The theoretical equation (4.17) predicts that V_c/P is inversely proportional to U_{eq} ; therefore, the predicted ratio between V_c/P with 0.1 mm and that with 0.2 mm sediment is 1.22, which is close to the numerical result of 1.17 (Table 4.3). Furthermore, the theoretical eq. (4.16) suggests that A_c/A_b is inversely proportional to $U_{eq} D_c/D$. According to the ratio of D_c/D calculated on the basis of the data in Table 4.3, the predicted ratio between A_c/A_b with 0.1 mm and that with 0.2 mm sediment is 1.08, which is again close to the numerical result of 1.03 (Table 4.3).

It has been shown above that the theoretical model can predict the trends of the influences of tidal amplitude on scaling relations. Because the equilibrium velocity U_{eq} increases with tidal amplitude (Friedrichs, 1995), the coefficients before the power in eq. (4.16) and (4.17) are negatively related to tidal amplitude. This suggests that, for a constant area, the basin with a larger tidal amplitude has smaller values of A_c/A_b and V_c/P , which is confirmed by the numerical modeling results listed in Table 4.3 and field observations of Dieckmann (1985). Eq. (4.14) suggests that the coefficient before $P^{1.5}$ also varies inversely with U_{eq} and then with tidal amplitude. This is a possible explanation for the empirical values of Eysink (1990) that range from $8 * 10^{-5}$ in the Dutch Wadden Sea area, which has a relatively small amplitude of about 1 m (Dissanayake et al., 2009), to $6.5 * 10^{-5}$ in the Western Scheldt, which has a relatively large amplitude of about 2 m (Dronkers, 2005).

The theoretical model also suggests that the coefficients before the power in eq. (4.14) to (4.17) are inversely proportional to $\alpha^{0.5}$, but this was not confirmed in the numerical model. In Table 4.2, the numerical results show that different basin shape factors result in the same trends but that the values are greatly reduced. For example, with the same basin area but pronounced different shape factors, A_c/A_b in case c is only 7% smaller than in case d, and only 2% smaller in case f than in case g, whereas the theory predictions are 33% for both cases. This discrepancy may suggest that the shape factor is not externally imposed but instead internally self-formed and hence scale-independent. It is hypothesized that for systems with identical sedimentological

and hydrodynamic conditions (sediment grain size, tidal amplitude, etc.), the shapes of tidal basins at different scales and orders are generally identical, being unrelated to the imposed basin boundaries. This hypothesis is similar to fractal theory and should be investigated in the future.

4.6.2. The mechanisms for the formation of scale-dependent morphology

The morphological equilibrium of tidal basins mainly results from a balance between flood dominated landward input of sediment related to offshore tidal asymmetry and ebb dominated seaward sediment output due to Stokes' drift (Dronkers, 2005). Increases in tidal flat areas and decreases in tidal amplitude and channel depth ratios can reduce the tidal asymmetry in tidal basins until the equilibrium morphology is reached (Friedrichs and Aubrey, 1988). These considerations imply the existence of an equilibrium channel and basin area ratio, and an equilibrium channel volume and tidal prism ratio.

Empirical regressions demonstrate that both ratios have power-law relations with basin area, the power coefficient being 0.5. The equivalent forms of these relations are that channel area and volume are proportional to the 1.5 power of basin area. These 1.5-power-law relations can be simply explained by the theoretical model outlined above. In an equilibrium state, the uniform equilibrium channel velocity causes the cross-sectional areas to be proportional to the tidal prism. Observations have shown that this is dependent on the tidal drainage basin area (Williams et al., 2002). The direct proportional relationships between cross-sectional areas and basin areas were confirmed by the theoretical model in the present paper, besides having also been verified by observations, e.g., in the Venice Lagoon tidal basins (D'Alpaos et al., 2010). The channel volume can thus be obtained by integrating the cross-sectional area in the flow direction through the length dimension of the basin. This results in the 1.5 power relationship between channel volume and basin area. Due to the scale-insensitivity of the characteristic basin depth and the ratio between channel depth and the characteristic depth, which have been confirmed in the numerical model

and by observations in the North Frisian Wadden Sea of Schleswig-Holstein, channel area is also proportional to the 1.5 power of basin area. This is the physical basis of the power-law relationships.

Several other factors, which are not included in the present investigation, may also be involved in the formation of an equilibrium tidal basin morphology. Thus, wave action not only plays an important role in local tidal flat morphology (Friedrichs and Aubrey, 1996; Roberts et al., 2000; Fagherazzi et al., 2006, 2007), but is also involved in transporting sediment to the inlet mouth by longshore drift along the seaward boundary of barrier islands (Gao and Collins, 1994). The importation of some of this sediment into the tidal basin would obviously influence the evolution of basin morphology. By the same token, storm surges can induce conspicuous sediment transport and morphological changes in tidal basins (Bartholdy and Aagard, 2001; Bartholomä et al., 2009; Lettman et al., 2009). In the present study uniform sediment grain sizes were employed in the theoretical and numerical models and it can be expected that changing grain sizes and related bedforms and roughness factors will affect the morphology predicted by the prevailing models. For example, bed armoring by coarse lag deposits (shell) may prevent channel deepening (Flemming and Ziegler, 1995).

The presence of local wind-generated waves provides a potential explanation for the existence of different coefficients before the power in scaling relationships between empirical and numerical modeling results. In the scaling of A_c/A_b , the empirical values of the coefficients are $2.5 * 10^{-5}$ in eq. (4.2) for the southern German Bight area and $2.59 * 10^{-5}$ in eq. (4.5) for the North Frisian Wadden Sea coast. In contrast to this, the numerical modeling yields a common coefficient of $3.95 * 10^{-5}$ in eq. (4.18). On the other hand, both empirical and numerical models result in very similar coefficients of $6.54 * 10^{-5}$ in eq. (4.7) and (4.20) for the scaling relations of V_c/P , and coefficients of $4.70 * 10^{-5}$ in eq. (4.6) and $4.13 * 10^{-5}$ in eq. (4.19) for the scaling relations of V_c . These results suggest that, in comparison to observations, for the same basin area, the numerical model produces similar channel volumes but larger channel areas, which

may indicate a reduced average channel depth, this effect increasing with the basin scale.

This reduced average channel depth in the numerical modeling is partly due to the contribution of shallow channel areas with elevations close to MLW. Fagherazzi et al. (2006, 2007) suggest that wave shear stress peaks for a specific water depth, varying from -1.5 m for unlimited fetch (>3000 m) to -0.6 m for a fetch of 1000 m in the Venice Lagoon which has a tidal amplitude of 0.35 m. This critical depth for peak wave shear stress prevents the formation of a stable bed around this depth and induces bed elevations either above or below it. In the German Wadden Sea tidal basins, which have a relatively large fetch of several kilometres and tidal amplitudes of 1 to 1.5 m, it is possible that the critical depths are below or close to MLW, thereby reducing the channel area at this elevation. It can then be expected that this wave contribution increases with the basin scale because larger basins with longer fetchs favors stronger wave action. Because wave action is not considered in the numerical model, the existence of the scale-increasing, unrealistic shallow channel area leads to larger coefficients for the scaling relations of A_c/A_b .

4.6.3. Implications for morphological changes induced by reclamation and sea level rise

The nonlinear responses of channel area and volume to basin area have potential implications for the morphological behavior of tidal basins in response to SLR and human impact. In the Wadden Sea, which has experienced extensive land reclamations over the past 1000 years, large parts of the tidal basins near the mainland boundary have disappeared (Flemming and Nyandwi, 1994; Mai and Bartholomä, 2000). Due to the landward position of the reclaimed areas, they had relatively small channel areas. This implies that the remaining tidal basins had relatively large channel areas that had to be filled by the reduced tidal prism to regain the initial balance between channel area and volume ratio. Furthermore, because the channel area and volume are proportional to the 1.5 power of basin area, the reduced basins require

more sediment input to reach equilibrium. The potential sources for these sediments include the ebb tidal deltas and the barrier-island shorefaces. Sediment transfer to the back-barrier basins from the latter source must, over time, inevitably induce a landward retreat of the barrier islands.

This has also been postulated by Flemming and Bartholomä (1997) on the basis of an empirical conceptual model for the stratigraphic evolution of the Wadden Sea. Since not enough sediment is provided from external sources, the system compensates SLR by moving sediment from the upper barrier-island shorefaces to the back-barrier basins. As a consequence, the islands migrate landwards across their own back-barrier tidal flats. In fact, reduced tidal basins created by SLR need more sediment to compensate SLR because of their more rapidly decreasing channel volumes compared to the decreasing basin area. This process exacerbates the retreat of the islands until a new equilibrium state is achieved.

4.7. Conclusions

In tidal basins, empirical, theoretical and numerical models show scale-dependent relationships between equilibrium morphological parameters and basin scales: the dimensional parameters of channel area and volume are proportional to the 1.5 power of the basin area and tidal prism, respectively, and the dimensionless parameters of relative channel area and the ratio between channel volume and tidal prism are both proportional to the square root of basin area. The coefficients before the power in these relations are in the order of 10^{-5} in both empirical and numerical models, which can be compared with the predictions of theoretical models associated with some scale-insensitive parameters, including the equilibrium channel velocity, characteristic basin depth, and the ratio of channel depth to characteristic basin depth.

These scale-dependent relations can be simply explained by the theoretical model: integrating the channel cross-sectional area, which is directly proportional to the basin area, in the flow direction results in the 1.5 power relationship between the channel

volume and basin area. Due to the scale-insensitive ratio between channel depth and characteristic depth, the channel area is also proportional to the 1.5 power of basin area.

5. Modelling the Equilibrium Hypsometry of Back-barrier Tidal Flats in the German Wadden Sea (southern North Sea)

Abstract

Hypsometry is the distribution of volume or horizontal surface area with respect to elevation. Some observations show contradictory scale-dependent characteristics of tidal flat hypsometries in back-barrier tidal basin environments, and traditional theory explains the flattening hypsometry by relating concave-up hypsometries in low tidal range basins to the dominating influence of wind waves rather than tidal currents. In order to investigate these two problems, two series of numerical modeling exercises were carried out using schematized rectangular back-barrier tidal basins roughly corresponding to the tidal basins found in the German Wadden Sea. The results show that, in the equilibrium states of tidal basins, hypsometries of back-barrier tidal flats are dependent on the basin scale and tidal range. Thus, large basin areas and low tidal ranges favour strong concave-up hypsometries, whereas small basin areas and high tidal ranges favour less concave-up hypsometries. Because wind waves were excluded in the model, these relationships are purely associated with tidal-current action. In addition to traditional theory, which emphasizes the relative importance of wind waves, the flattening of hypsometric profile shapes can therefore also be interpreted as a response to the relative area of intertidal areas or channels in the tidal basins. Thus, if tidal channels have relatively large areas, the development of tidal flats between channels is markedly restrained, the tidal flats being prevented from growing upward to higher elevations. As a result, strong concave-up hypsometries are formed that are associated with relatively large areas of low tidal flats and small areas of high tidal flats. As basins with large areas and low tidal ranges have large relative channel areas, this results in pronounced concave-up hypsometries, and vice versa.

5.1. Introduction

Hypsometry is a concise and quantitative method to characterize and understand the morphological characteristics of the Earth's surface (Strahler, 1952; Emery, 1979; Walcott and Summerfield, 2008). In mountainous areas, the hypsometry of fluvial drainage basins has been shown to be sensitive to tectonic, lithologic, and climatic factors, which, in turn, make it a useful proxy for these external factors (Masek et al., 1994; Perez-Pena et al., 2009; Jansen et al., 2010). By analogy, hypsometry is a sensitive morphological parameter of tidal basins and tidal flats, being not only related to hydrodynamics and morphodynamics (Boon and Byrne, 1981; Eiser and Kjerfve, 1986; Marciano et al., 2005; Toffolon and Crosato, 2007; Moore et al., 2009) but having also been shown to be useful in ecological and environmental contexts (Kirby, 2000; Oertel, 2001; Sanderson and Coade, 2010). For example, Wang et al. (2002) addressed the relationship between hypsometry and tidal asymmetry, and Oertel (2001) suggested that hypsometry has a strong influence on wetland health. The types of sediment in these tidal basin systems are diverse, covering sand (Wang et al., 2002; Toffolon and Crosato, 2007), fine sand and silt (Moore et al., 2009), mud-sand mixtures (Boon and Byrne, 1981), and mud (Kirby, 2000).

Two kinds of hypsometric curves are used in practice to characterize the morphology of tidal basins (Oertel, 2001). The first kind, called volume hypsometry, is the water volume below a reference elevation as a function of this elevation (Wang et al., 2002). The second kind, called area hypsometry, is the horizontal basin surface area below a reference elevation with respect to this elevation (Friedrichs and Aubrey, 1996). In order to compare the shape of hypsometric curves, these parameters, which include water volume, surface area, and elevation, are usually normalized to some characteristic values. Normalization is particularly essential when the relevant parameters vary significantly between different basins. If the tidal system is simplified to a one-dimensional cross-shore system, the area hypsometric curve degenerates into a cross-shore tidal flat profile (Friedrichs and Aubrey, 1996).

There are still some unknown aspects about tidal basin and tidal flat hypsometry. A

first problem concerns scale effects. Geomorphological and sedimentological systems are generally suggested to respond on specific spatial scales (Dodds and Rothman, 2000), such scale-dependent hypsometric characteristics having been observed and successfully modeled in the case of fluvial basins (Willgoose and Hancock, 1998; Hurtrez et al., 1999). In the case of tidal basins, however, such hypsometric scale effects are still in dispute. Thus, for the volume hypsometry of German Wadden Sea tidal basins (southern North Sea), Renger and Partenscky (1974) found a logarithmic relationship between the water volume below a certain elevation and this elevation with an empirical coefficient for any individual tidal basin, and suggested that this coefficient reflected a power-law relationship with the basin area. This means that the hypsometry is scale-dependent. On the other hand, comparing two American tidal basins, Boon (1975) and Boon and Byrne (1981) suggested that area hypsometry was scale-independent. Then, following the early work of Strahler (1952), they used the area hypsometry as an indicator of the evolutionary stage of tidal basins regardless of scale differences, relating a certain shape of the hypsometric curve to an immature, mature or more mature state of tidal basins. This concept has been applied by Moore et al. (2009) to evaluate the development of estuary morphology. In this context, and besides the unclear definition of 'mature', a systematic investigation of scale effects on tidal basin hypsometry is still lacking.

The second problem concerns the influence of tidal range on tidal basin hypsometry. For the area hypsometry of tidal flats in German Wadden Sea tidal basins, Dieckmann et al. (1987) suggested that the hypsometric curves tended to be more concave-up for tidal flats having a lower tidal range and less concave-up for tidal flats having a higher tidal range. Friedrichs and Aubrey (1996) attribute the concave-up hypsometry of tidal flats in low tidal range basins to the dominant forcing of wind waves rather than tidal currents, but the question remains whether tidal processes alone could generate the observed responses of the hypsometric shapes to the tidal ranges.

Numerical modeling was suggested to be a useful tool to study the morphodynamics of tidal basin systems (Wang et al., 1995; de Swart and Zimmerman, 2009). With the

development of new numerical modeling techniques (Latteux, 1995; Lesser et al., 2004; Roelvink, 2006), long-term morphodynamics of tidal basins in the Wadden Sea have been successfully studied by means of two-dimensional (2D), process-based models (Wang et al., 1995; Dastgheib et al., 2008; Dissanayake et al., 2009).

In the present study, two series of numerical modeling exercises have been carried out to investigate the two problems of back-barrier tidal basin hypsometry outlined above: (1) Is hypsometry scale-dependent or scale-independent? (2) How is basin hypsometry influenced by tidal range (mean tidal current strength)? The study focuses on the hypsometry of the tidal flat area between the mean low-water level (MLW) and the mean high-water level (MHW) of tidal basins because a) it is of particular importance for ecological systems, and b) it can be directly compared with the results of previous studies (Boon, 1975; Eiser and Kjerfve, 1986; Dieckmann et al., 1987; Friedrichs and Aubrey, 1996; Kirby, 2000).

5.2. Study area

The study area is the East Frisian sector of the German Wadden Sea, which borders the coast of the southern North Sea between the river Ems in the west and the Jade Bay in the east (Fig. 5.1). The East Frisian Wadden Sea is 4–12 km wide and stretches over 90 km along the coast, comprising a chain of seven barrier islands and six large tidal basins characterized by a network of tidal channels (Ehlers, 1988). The back-barrier tidal basins are predominantly controlled by tidal forcing, although locally generated wind waves are strongly dependent on the fetch distances and water depth and play an important secondary role (Krögel and Flemming, 1998). The tide is semidiurnal with average tidal ranges of 2.2 m in the west and 2.8 m in the east, respectively. Tidal current speeds during fair weather reach up to 1.3 m/s in the inlets and 0.3 m/s on the tidal flats (Davis and Flemming, 1991). Current velocities are stronger near the inlet mouths and decrease toward the landward boundary and tidal basin drainage divides. Within the back-barrier tidal basins, surface sediments mainly

consist of sand, muddy sand, sandy mud and mud, the grain-size distribution patterns revealing a well-defined landward fining trend (Flemming and Ziegler, 1995). Due to land reclamation, the position of the mainland dike appears to have enhanced energy levels near the mainland shore, as a consequence of which finer sediments ($<90\mu\text{m}$) are unstable and hence prevented from permanent deposition (Flemming and Nyandwi, 1995).

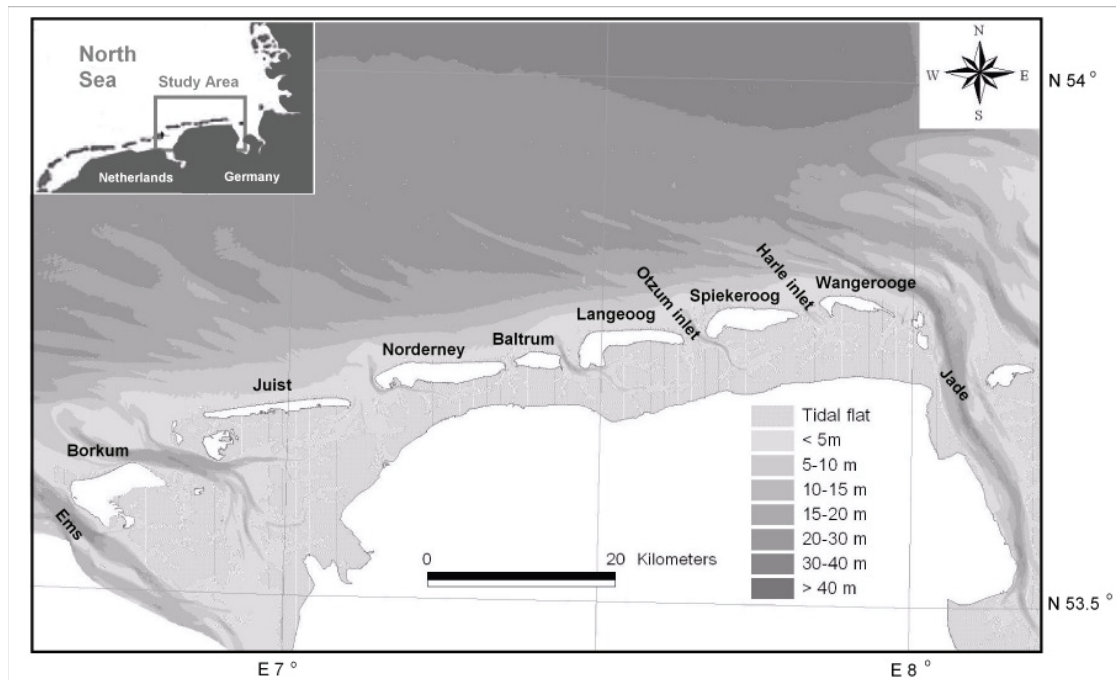


Fig. 5.1. Location map of the study area along the East Friesian barrier-island coast of the German Wadden Sea (southern North Sea). The color bar denotes the water depth relative to mean sea level (m).

5.3. Methods

5.3.1. Model description

In order to assess the physical processes involved in the formation of equilibrium hypsometry, a two-dimensional, depth-averaged process-based morphodynamic model (Delft3DTM software package) was applied to a schematized model domain having dimensions similar to the tidal basins of the German Wadden Sea. Delft3DTM has been utilized and validated widely in different coastal environments to simulate

morphodynamic changes at different time scales (e.g., Tonnon et al., 2007; Edmonds and Slingerland, 2010), including tidal basins of the Wadden Sea region (Marciano et al., 2005; Dastgheib et al., 2008; Dissanayake et al., 2009).

In the model, only tidal forcing was considered, neglecting vertical velocities, Coriolis force, density differences, wind and waves, this being consistent with other long-term morphological modelling studies (Dastgheib et al., 2008; Dissanayake et al., 2009; van der Wegen et al., 2010). The two-dimensional depth-averaged continuity equation and nonlinear, shallow-water momentum equations for incompressible free surface flow were solved numerically with a constant seabed drag coefficient for sandy beds of $3 * 10^{-3}$ (Soulsby, 1997; de Swart and Zimmerman, 2009). A detailed description of the Delft3DTM flow model can be found elsewhere (Lesser et al., 2004).

Sediment transport was calculated by van Rijn's approach (see Dissanayake et al., 2009, and the Delft3DTM flow manual for a full reference) for non-cohesive sands, and the standard advection-diffusion equation was employed for suspended sediment transport. Both suspended load and bedload were involved in the Exner equation for sediment mass conservation to simulate the morphological changes. In order to save calculation time for long-term modelling, the "online" approach suggested by Roelvink (2006) was adopted, which speeds up bed adjustments by multiplying the bed sediment flux in each time step by a morphological scale factor (MF). This method has been successfully applied using a typical MF in the order of 100 (Dastgheib et al., 2008; Dissanayake et al., 2009; Edmonds and Slingerland, 2010; Geleynse et al., 2010). In the present model, an MF of 60 was taken.

5.3.2. Model setting

In the first series of model runs, the scaling characteristics of tidal basin hypsometry were investigated. For this purpose, nine cases with different spatial scales were constructed and numerically modeled (case a to i in Table 5.1). Each case comprises idealized rectangular back-barrier tidal basins with three inlets, as was suggested by de Swart and Zimmerman (2009) and which is in good agreement with the tidal basins

of the German Wadden Sea region. The basin areas increase by a factor of 12 from 21.3 to 243 km² from case a to i, covering the main data range used for the regression by Renger and Partenscky (1974). In order to investigate the influences of basin shape, case c and d, and case f and g were designed to have the same basin areas but different shape factors, which are defined as the ratio of the basin cross-shore length to its longshore length.

Table 5.1. Numerical modeling results for tidal basins with different scales and tidal ranges after a 60 year simulation period.

No.	A (km ²)	α	ID (m)	TR (m)	A_f/A	H/TR	H_{max}/TR	b	HI
1st Series for Scale effect									
Case a	21.3	0.34	1.50	3.00	0.78	0.38	0.79	0.95	0.48
Case b	32.0	0.50	1.50	3.00	0.75	0.38	0.85	0.86	0.45
Case c	48.0	0.75	1.50	3.00	0.72	0.40	0.89	0.71	0.45
Case d	48.0	0.34	1.50	3.00	0.70	0.36	0.79	0.73	0.46
Case e	72.0	0.50	1.50	3.00	0.67	0.33	0.78	0.67	0.42
Case f	108.0	0.75	1.50	3.00	0.58	0.29	0.79	0.55	0.39
Case g	108.0	0.34	1.50	3.00	0.57	0.30	0.68	0.56	0.44
Case h	162.0	0.50	1.50	3.00	0.52	0.27	0.67	0.48	0.40
Case i	243.0	0.75	1.50	3.00	0.42	0.26	0.78	0.40	0.33
2nd Series for tidal range effect									
Case e1	72.0	0.50	1.00	2.00	0.62	0.26	0.79	0.64	0.33
Case e	72.0	0.50	1.50	3.00	0.67	0.33	0.78	0.67	0.42
Case e2	72.0	0.50	2.00	4.00	0.71	0.38	0.85	0.77	0.45

where A is the basin area, α is the ratio between the basin cross-shore length and its longshore length, ID is the initial water depth below MSL in the basins, TR is the tidal range, A_f is the tidal flat area, H is the average tidal flat elevation above MLW, H_{max} is the maximum tidal flat elevation above MLW, b is the coefficient in eq. (5.2) representing the shape of the volume hypsometry, and HI is the area hypsometric index in eq. (5.3) representing the shape of the area hypsometry. All the cases have been simulated with a grain size of 0.15 mm.

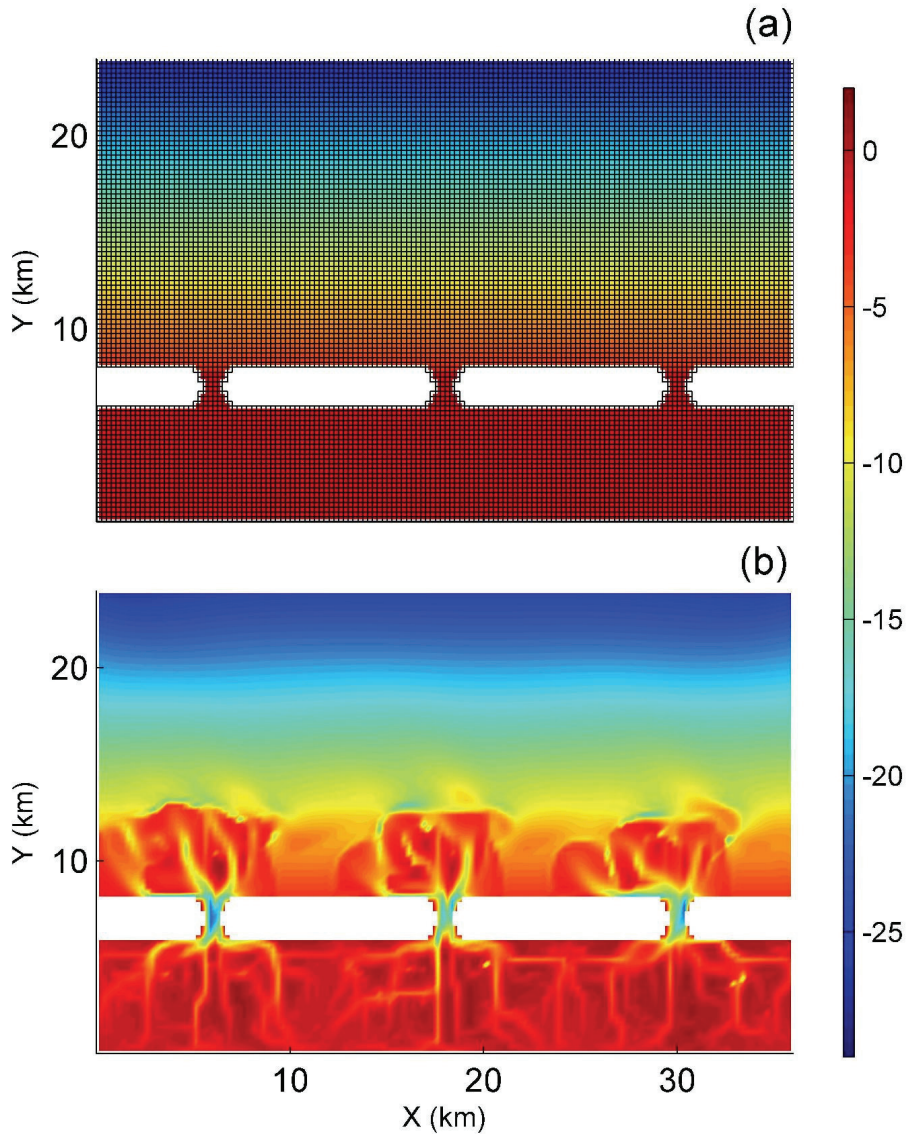


Fig. 5.2. (a) The initial bathymetry and grid of the reference case e in Table 5.1. (b) The final bathymetry of case e after a 60 year simulation period. The color bar denotes the bed elevation relative to mean sea level (m).

Case e is taken as the reference case, which has an intermediate size of 72 km^2 , similar to that of the Otzum tidal catchment between Spiekeroog and Langeoog Islands in the German Wadden Sea. The modeling domain, bathymetry and grids of case e are shown in Fig. 5.2a where three tidal basins are bounded by a chain of barrier islands interrupted by three inlets connecting to the open sea, each basin having a width of 12 km and a length of 6 km. The initial depth of the basins was set at a constant value of 1.5 m, which equals the tidal amplitude of the dominant M2 tide

along the open North Sea boundary of the model domain. This initial bathymetry defines the basin at the depth of MLW, the boundary separating tidal channels and tidal flats. In the outer area, the water depth progressively increases from 3 m off the barrier islands to 25 m along the northern open sea boundary. A representative mean bed sediment grain size of 0.15 mm was adopted in the model, which corresponds to the dominant grain size recorded by Flemming and Ziegler (1995) in the Otzum tidal catchment. In accordance with Todeschini et al. (2008) and van der Wegen et al. (2010), the water-level of the dominant M2 tide was employed for the seaward boundary with a tidal range of 3 m, which approximates the spring tidal range in the East Friesian Wadden Sea (Flemming and Davis, 1994). The two lateral boundaries were defined as Neumann boundaries to allow the alongshore velocity and water level to develop without disturbance (Dastgheib et al., 2008; Dissanayake et al., 2009). The other eight cases have the same initial and boundary conditions but changing modelling domains with respect to area and/or shape factor.

In the second modeling series, the influences of tidal range were evaluated. As in the case of the first modeling series, case e with a tidal range of 3 m was again chosen as the reference case. In addition, two other cases were designed (cases e1 and e2), which were forced by tidal ranges of 2 and 4 m, respectively, the other settings being kept the same as in case e, except that the initial basin depths were adjusted to the respective tidal amplitudes in order to retain the same characteristic basin bed states relative to MLW. The characteristics of the basins in these cases are shown in Table 5.1.

All the model cases were simulated for a 60 year period to make sure that the system reached equilibrium, van Dongeren and de Vriend (1994) having suggested a characteristic time of 30 years for generating equilibrium tidal basin morphology in the Wadden Sea. The equilibrium state of the system was assessed by the temporal evolution of two characteristic morphological parameters, the relative area of tidal flats (A_f/A) and the average tidal flat elevation above MLW (H).

5.3.3. Data processing

For the volume hypsometry, Renger and Partenscky (1974) established an empirical logarithmic correlation between the water volume and the elevation:

$$Z = \log_a(V/V_L) \quad (5.1)$$

where Z is the elevation above MLW, V is the water volume stored below this elevation, V_L is the water volume stored below MLW, and a is a regression coefficient representing the shape of the volume hypsometry, the upward concavity of the curve shape decreasing with increasing values of a . Contrary to the normalized water volume (V/V_L), Z on the left side of eq. (5.1) is a dimensional value. In order not to obscure differences between tidal basins with different vertical scales (tidal ranges), eq. (5.1) was normalized to the tidal range (TR):

$$\log(V/V_L) = (TR \log a)(Z/TR) = b(Z/TR) \quad (5.2)$$

where b is a more robust volume hypsometry shape indicator than coefficient a but has the same inverse shape relationship as the latter.

The hypsometric integral (HI), which is defined by the area below the non-dimensional area hypsometric curve, was used as an indicator of the curve shape, larger HI-values being associated with less concave-up curve shapes (Willgoose and Hancock, 1998; Cohen et al., 2008). HI provides a quantitative measure for comparing catchments and has been applied widely to fluvial basins (Walcott and Summerfield, 2008; Jansen et al., 2010). For tidal flats, the non-dimensional HI can be calculated as:

$$HI = \frac{H - H_{min}}{H_{max} - H_{min}} = \frac{H}{H_{max}} \quad (5.3)$$

where H , H_{min} and H_{max} are the average, minimum and maximum tidal flat elevations above MLW, and H_{min} is equal to 0. Eq. (5.3) suggests that HI and the area hypsometry shape are controlled by the ratio between the mean and maximum heights

of tidal flats, and if two flats have a similar H_{max} , the area hypsometric curve of the flat with the larger mean elevation is less concave-up.

5.4. Results

5.4.1. Equilibrium state examinations

Two representative parameters, namely the relative area of tidal flats (A_f/A) and the average tidal flat elevation above MLW (H), were chosen for the equilibrium state examinations. In Fig. 5.3, the temporal evolution of these two parameters in cases a, e, and i (cf. Table 5.1), which correspond to the minimum, intermediate, and maximum areas, respectively, show that they remain stable after the 60 year simulation period, indicating that the basin and tidal flat systems have attained equilibrium states. It is noted that the time needed for equilibrium is related to the spatial scale, i.e. the larger the basin, the longer the time to reach equilibrium, this having also been suggested for fluvial systems (Dade and Friend, 1998).

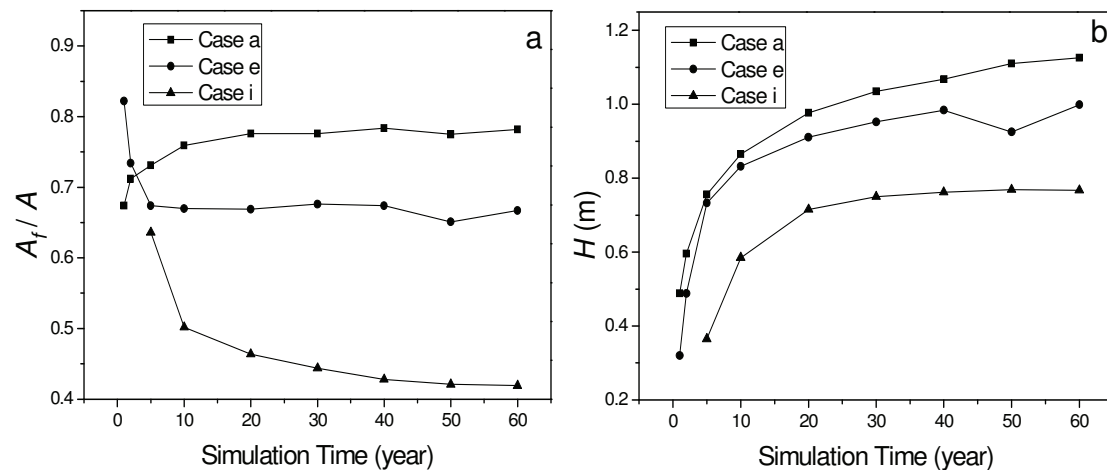


Fig. 5.3. Temporal evolution of a) the relative area of tidal flats (A_f/A), and b) the average tidal flat elevation above MLW (H) for cases a, e, and i in Table 5.1, which have the minimum, intermediate, and maximum areas, respectively.

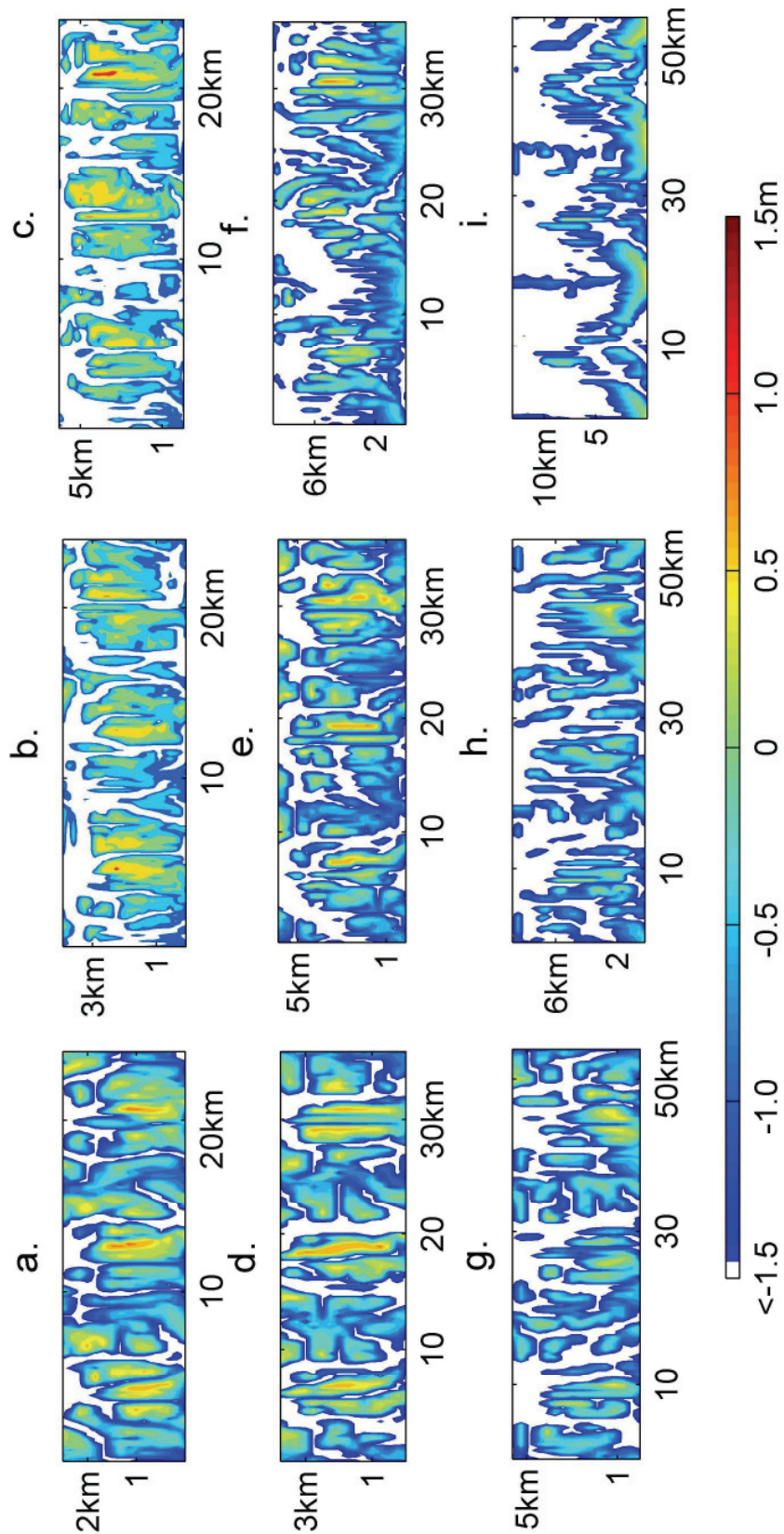


Fig. 5.4. The final bathymetry of the tidal flats after a 60 year simulation; (a) to (i) correspond to the cases a to i in Table 2, respectively. The color bar denotes the bed elevation relative to mean sea level (m), and the white areas are channels below MLW.

5.4.2. Scale effects

Scale effects on back-barrier tidal flat hypsometries were investigated in the first modeling series. Fig. 5.2b shows the final bathymetry over the whole modeling domain for reference case e after a 60 year simulation period where the tidal basins have become filled with sediment accompanied by the formation of tidal flats and dendritic tidal channel systems, and the formation of ebb tidal deltas on the seaward side of the inlets. The other eight cases have the same general morphological aspects (not shown). The overall morphology generated by the simulations is consistent with the real back-barrier tidal basin systems of the German Wadden Sea.

The final tidal flat morphology of the nine cases in the first modeling series (case a to i) is illustrated in Fig. 5.4. Tidal flats are distributed in the form of patches separated by tidal channels, and the crests of flats are located at the watersheds between the channels. Fig. 5.4 and Table 5.1 show that, with increasing basin area, the relative area of tidal flats (A_f/A) is progressively reduced from 0.78 in case a to 0.42 in case i..

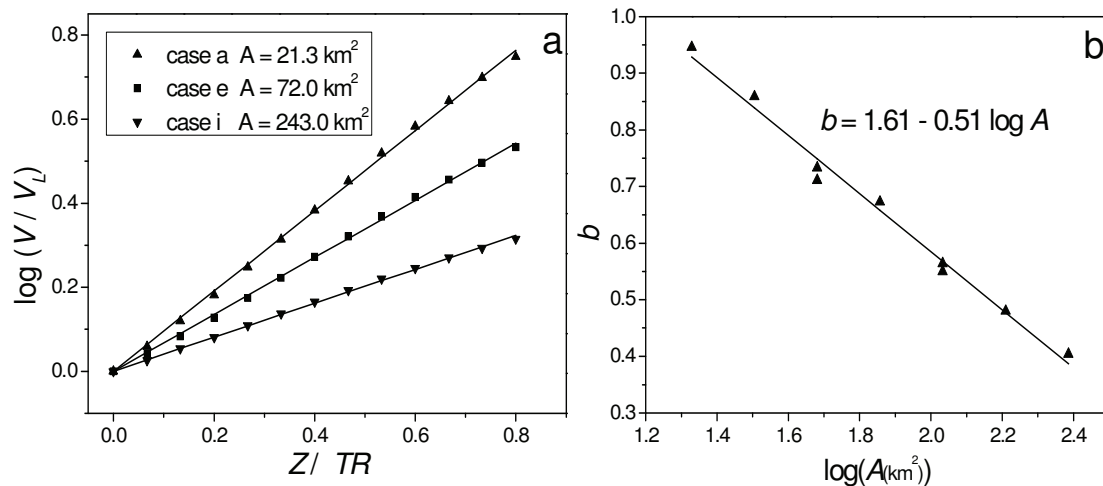


Fig. 5.5. (a) Volume hypsometric curves describing the relationship between the water volume (V) and the elevation above MLW (Z) for cases a, e and i in Table 5.1, which have the minimum, intermediate, and maximum areas, respectively. The water volume is normalized to the water volume below MSL (V_L), and the elevation is normalized to a tidal range of 3 m (TR). Data points show the modelling results, and the lines are the regressions in terms of eq. (5.2). (b) The relationship between the coefficient b and the basin area (A) in km^2 .

The volume hypsometric curves of tidal flats were derived for cases a to i, each showing an excellent correlation with elevation as defined in eq. (5.2). This is illustrated in Fig. 5.5a for cases a, e and i as listed in Table 5.1. These cases correspond to the minimum, intermediate, and maximum area, respectively. From Table 5.1 and Fig. 5.5b it is evident that the coefficient b decreases linearly with increasing basin area (A in km^2) as expressed by the equation:

$$b = 1.61 - 0.51 \times \log A \quad (5.4)$$

Because b is inversely proportional to the upward concavity of the hypsometric curve, eq. (5.4) indicates that, under the model assumptions, volume hypsometry is indeed scale-dependent, i.e. the larger the basin area, the stronger the upward concavity of the volume hypsometry.

In the case of area hypsometry, corresponding curves were plotted between the elevation and the relative horizontal tidal flat areas below this elevation. This is illustrated in Fig. 5.6a for cases a, e and i, which shows that upward concavity increases with increasing basin area. Fig. 5.6b demonstrates that the maximum tidal flat elevation (H_{max}) is not correlated with basin area. Instead, as illustrated in Fig. 5.6c, the average tidal flat elevation (H) is negatively correlated with the basin area (A in km^2):

$$H / \text{TR} = 0.39 - 6.67 \times 10^{-4} A \quad (5.5)$$

where the tidal range (TR) is 3 m. As a consequence, and in agreement with eq. (5.3), the hypsometric integral (HI) has an inverse linear relationship with basin area (A in km^2) (Table 5.1 and Fig. 5.6d):

$$\text{HI} = 0.48 - 5.81 \times 10^{-4} A \quad (5.6)$$

This suggests that the upward concavity of the curve is proportional to the basin scale, thus indicating that the area hypsometry has the same scale-dependent characteristics as the volume hypsometry: the basin with the larger area is associated with an area

hypsoetry having a stronger upward concavity. It is noted that the volume hypsoetry and area hypsoetry are related to each other. The basin surface area is the derivative of the water volume to the related elevation. Therefore, the volume hypsoetry and area hypsoetry have similar scale dependent characteristics.

From Table 5.1 it can be seen that basins with the same areas but different shapes (cases c and d, and cases f and g) have similar volume hypsoetry shape coefficients (b), whereas the area hypsoetry shape coefficients (HI) are similar in small basins (cases c and d) but dissimilar in larger basins (cases f and g).

5.4.3. Tidal range effect

The influences of tidal range on the tidal flat volume and area hypsoetries were evaluated in the second numerical modeling series (Table 5.1). As illustrated in Fig. 5.7a, the basin with the larger tidal range (e2) has a higher volume hypsoetry shape coefficient (b), indicating less upward concavity of the corresponding volume hypsoetric curve. This is also evident in Fig. 5.7b, which shows the same relationship between area hypsoetry and tidal range. Therefore, the tidal flat hypsoetric concavity is negatively correlated with tidal range in the case where only tidal processes are taken into account.

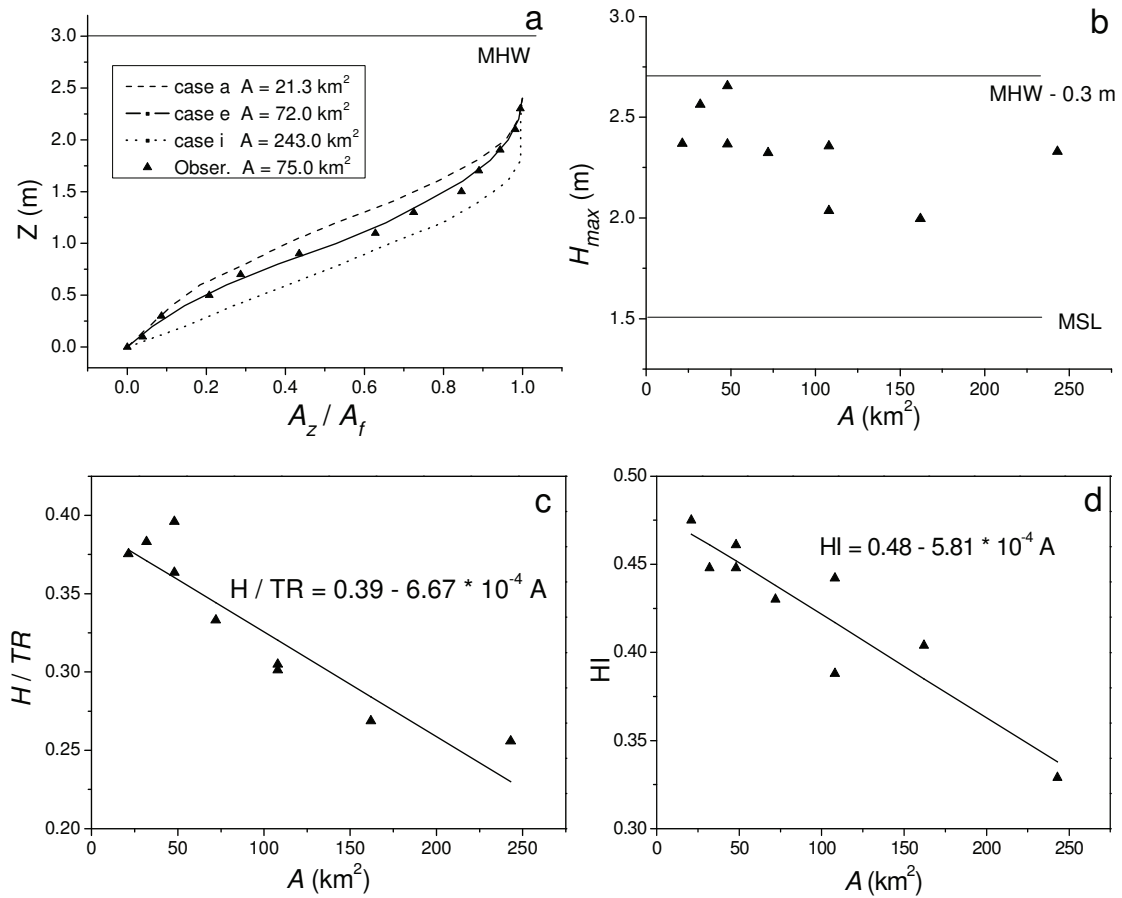


Fig. 5.6. (a) Area hypsometric curves describing the relationship between the tidal flat area (A_z) and the elevation above MLW (Z). The tidal flat area is normalized by the total tidal flat area in the basin (A_f). The lines show the modeling results for cases a, e and i in Table 5.1, the data points representing the observed tidal flat bathymetry of the Otzum and Harle tidal catchments in the German Wadden Sea, both having an average catchment area of about 75 km^2 . (b) The relationship between the maximum tidal flat elevation (H_{max}) and the basin area. (c) The relationship between average tidal flat elevation (H) and basin area (A), where H is normalized to a tidal range (TR) of 3 m. (d) The relationship between the hypsometric integral (HI) and the basin area. All basin areas are in km^2 .

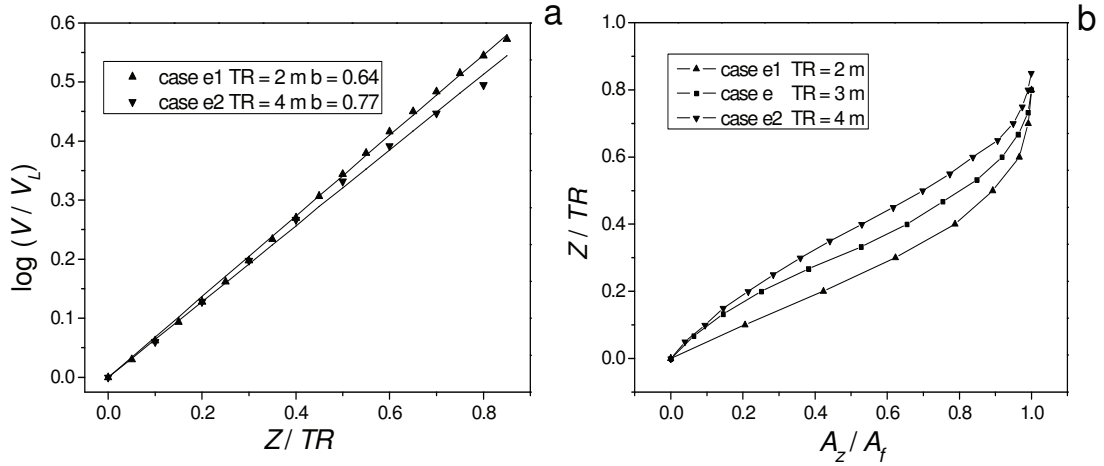


Fig. 5.7. (a) Volume hypsometric curves describing the relationships between the water volume (V) and the elevation above MLW (Z) for cases e1 and e2 with different tidal ranges (Table 5.1). The water volume is normalized to the water volume below MSL (V_L). Data points show the modeling results, and the lines are the regressions in terms of eq. (5.2) with regression coefficient b . (b) Area hypsometric curves describing the relationships between the tidal flat area (A_z) and Z for cases e1, e and e2. The tidal flat area is normalized to the total flat area in the basin (A_f). In both (a) and (b), the elevation is normalized to the tidal range (TR).

5.5. Discussion

5.5.1. Comparison with observations

Due to the schematic model settings, the numerical modeling results can only be compared with a few matching field cases. However, more importantly, the observed model trends demonstrate the morphodynamic response of tidal basins to changes in external forcing.

The observed tidal flat area hypsometries of the Otzum and Harle tidal catchments of the German Wadden Sea, which both have average catchment areas of about 75 km^2 , show good agreement with that illustrated in Fig. 5.6a for case e with an area of 72 km^2 .

The relationship between the volume hypsometry shape coefficient b and the basin area (A in km^2) was initially obtained from observations in the German Wadden Sea

by Renger and Partenscky (1974):

$$b = 2.09 - 0.81 \times \log A \quad (5.7)$$

Comparing this equation with eq. (5.4) of the modelling results shows that both describe the same response pattern of b to A , although absolute values are somewhat different.

Based on the observations in the Dutch Wadden Sea, Eysink (1993) established an empirical relationship between the average tidal flat elevation (H) and the basin area (A in km^2):

$$H / \text{TR} = 0.41 - 2.9 \times 10^{-4} A \quad (5.8)$$

This equation is very similar to eq. (5.5) of the modelling results. This indicates that the decrease in average tidal flat elevation with increasing basin area revealed in the modeling results is consistent with field observations, although the modeling results expressed in eq. (5.5) show a more rapid decrease than that suggested by eq. (5.8).

Eysink (1993) found that, in the Dutch Wadden Sea, the maximum tidal flat elevation (H_{max}) in most cases lay between MSL and MHW-0.3 m, and that it did not correlate with basin area. This phenomenon is also observed in the modeling results of this study (Fig. 5.6b). Because of the scale-dependence of the average tidal flat elevation and the scale-independence of the maximum elevation, the hypsometric integral (HI), as defined in eq. (5.3), is also scale-dependent and has the same scaling trend as the average tidal flat elevation in the Dutch Wadden Sea. This observation supports the numerical modeling findings of HI in eq. (5.6) and Fig. 5.6d.

Assessing the influence of tidal range, the modeling results illustrated in Fig. 5.7 show the same relationship between the tidal flat hypsometry shape and the tidal range as observed in the German Wadden Sea by Dieckmann et al. (1987). For the same region, Dieckmann (1985) suggested that the ratios between the median tidal flat elevations above MLW and the tidal ranges are 0.3-0.4 for lower mesotidal areas, 0.4-0.5 for upper mesotidal areas, and 0.5-0.6 for lower macrotidal areas, where the median

elevation is defined as the level corresponding to the 50th percentile of the cumulative area frequency of a tidal basin. In the modeling results, these ratios are 0.24, 0.32, and 0.38 for cases e1, e, and e2 with 2, 3, and 4 m tidal ranges, respectively. Although the absolute values of these ratios are lower than those found by Dieckmann (1985), the increasing trend of these ratios towards larger tidal ranges is the same.

5.5.2. Basin scale and tidal range control on the tidal flat hypsometry

The numerical modeling results clearly show that, under the model assumptions, in the equilibrium states of tidal basins, both volume and area hypsometries of back-barrier tidal flats are dependent on the basin scale and tidal range, i.e. large basin areas and low tidal ranges favor more pronounced concave-up hypsometries, whereas small basin areas and high tidal ranges favor more subdued concave-up hypsometries. It should be noted that only tidal processes were taken into account in the model.

Traditionally, for one-dimensional (1D) cross-shore tidal flat profiles along open-sea coasts, theoretical investigations (Zimmerman, 1973; Friedrichs and Aubrey, 1996) and numerical modeling experiments (Roberts et al., 2000; Pritchard et al., 2002) attribute the tidal basin hypsometry to the relative importance of forcing by tidal currents and wind waves, tidal current domination resulting in convex hypsometries, wind wave domination in concave hypsometries. This concept was applied to the tidal flats of the back-barrier basins of the German Wadden Sea to explain the associations of small tidal ranges with concave-up hypsometries and of large tidal ranges with convex hypsometries in the observations of Dieckmann et al. (1987) and Friedrichs and Aubrey (1996). The logic is that, with increasing tidal range, tidal currents play a more important role in tidal flat hypsometry, as a result of which hypsometric curves are less concave-up. Based on this logic, the scale-dependence of tidal flat hypsometry was investigated. The longer fetch in larger tidal basins allows wind waves to develop freely, the stronger wave action favoring a more pronounced concave-up hypsometry. The field evidence for basin scale and tidal range effects can be successfully explained in this way.

However, the present modeling results suggest that an alternative interpretation is also possible. Thus, in a model in which wind waves are excluded, tidal currents alone create the same type of relationships between basin scale or tidal range and tidal flat hypsometry in back-barrier tidal basins. In this context, the relative importance of tidal currents and wind waves can not be the sole mechanism.

A new mechanism arises from the application of the 1D cross-shore profile theory to the 2D back-barrier tidal basins, e.g. the German Wadden Sea. Because the cross-shore tidal flat slope towards the open sea is not significant in these environments, and the tidal flats develop between tidal channels, these can not be characterized by 1D cross-shore profiles (cf. Fig. 5.2b and 5.4). If 1D profiles are applied to tidal flats in the cross-channel direction, the development of the tidal flats is usually limited to different degrees by the neighboring channels, as illustrated in Fig. 5.4. This suggests that the tidal flat hypsometry of the whole tidal basin system has to be considered.

From a planimetric point of view, back-barrier tidal basins consist of two major elements, namely channels and tidal flats. Tidal channels have a format of dendritic networks (cf. Fig. 5.2b), which are required to distribute the tidal water and suspended sediment over the basin platform (Allen, 2000). The tidal flat hypsometry should thus to some extent be dependent on the size of the tidal channels, large channel areas being associated with subdued tidal flats between the channels, preventing the flats from reaching high elevations. As a result, a relatively large area of low tidal flats and a relatively small area of high tidal flats are formed, which is associated with a more pronounced concave-up hypsometry.

This hypothesis is supported by the present modeling results. Table 5.1 illustrates the uniform characteristics of basins with pronounced concave-up tidal flat hypsometries (e.g., case i and e1). Although these are related to large basin areas or low tidal range, a common feature is the association with relatively small tidal flat areas (A_f / A) or relative large channel areas. Basins with subdued concave-up hypsometries (e.g., case a and e2), in turn, have relatively large tidal flat areas. In Fig. 5.8 the volume

hypsoetry shape coefficient b is plotted against the relative tidal flat area (A_f/A) for all the cases in the two modelling series (Table 5.1). The excellent correlation suggests a uniform relationship regardless of the different external parameter influences (basin area or tidal range). In addition to the traditional theory of the relative importance of tidal currents and wind waves, the relative tidal flat area concept developed in this study is thus another possible interpretation of the effects of basin area and tidal range on the back-barrier tidal flat hypsoetry. Basins with large areas and low tidal ranges have large relative channel areas, which leads to a pronounced concave-up hypsoetry, and vice versa.

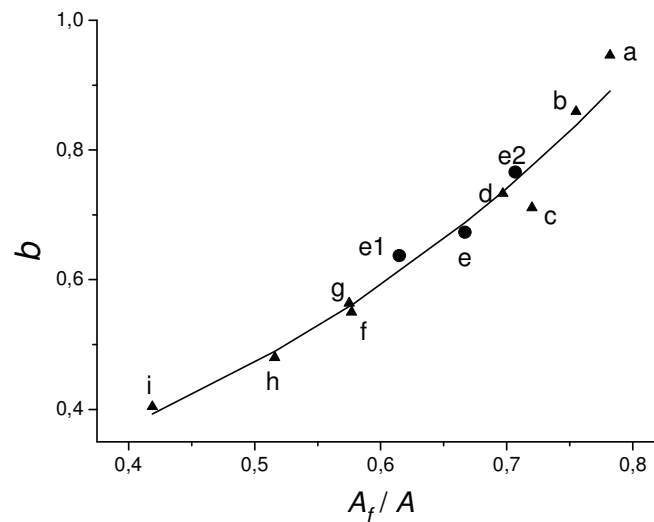


Fig. 5.8. Relationship between the volume hypsoetry shape coefficient b and relative tidal flat area of the tidal basins (A_f/A). Triangles denote the cases in the first modeling series for scale effect, and filled circles denote the cases in the second modeling series for tidal range effect (Table 5.1). Each case marks its corresponding point.

The response of relative tidal flat area in back-barrier tidal basins to the basin scale and tidal range will be investigated in a separate study on the basis of empirical, theoretical and numerical models, and is beyond the scope of the present paper.

It should be noted that the present modeling results reflect the conditions characterizing sandy environments and care must be taken when applying them to

mixed sand-mud and mud dominated tidal basins. The prediction of cohesive sediment transport is more complex and highly sensitive to input parameters such as the erosion constant, the critical erosion and deposition bed shear stresses, and the sediment bulk density (Whitehouse et al., 2000). Mixtures of sand and mud are even more complex. As a consequence, the hypsometric characteristics of tidal basins comprising mixed sand-mud or muddy sediments and their analogies/differences compared with sandy systems are still poorly understood.

In addition, the reasonable agreement observed between the model results based purely on tidal current forcing and field measurements does not imply that waves are of minor importance. The agreements of the model outputs in case e with prototype measurements in the Otzum and Harle tidal catchments may be attributed to the adoption of the constant seabed drag coefficient of $3 * 10^{-3}$. Soulsby (1997) suggested drag coefficients of $2.6 * 10^{-3}$ and $6.1 * 10^{-3}$ for unrippled and rippled sand, respectively, and $2.4 * 10^{-3}$ for sand/gravel and sand/shell mixtures. Because of efficient grain-size sorting, sand/gravel and sand/shell mixtures form lag deposits in the channels, whereas finer-grained sediments accumulate on the intertidal flats. Friedrichs (1995) suggested that, in equilibrium tidal basins, the tidal channels display a uniform bed shear stress throughout, the value being dependent on the bed grain size and the tidal range. Thus, higher current velocities are required to balance the small drag coefficients in the channels. Based on the conservation of tidal prisms, high channel velocities result in smaller channel cross-sectional areas, implying narrower tidal channels and, in turn, smaller channel planimetric areas. According to the above hypotheses, small channel planimetric areas may cause subdued concave-up hypsometries. Consequently, if smaller and more realistic channel drag coefficients were applied in the numerical model, the modeled hypsometric curve would be less concave-up than observed in case e in Fig. 5.6a. Wave forcing, on the other hand, tends to produce stronger concave-up curve trends. The two processes thus offset each other, thereby explaining the apparent consistency between model outputs and prototype measurements. However, as it is difficult to quantify wave effects, it is

currently impossible to reliably distinguish between the contributions of the two mechanisms to the back-barrier tidal flat hypsometry.

5.6. Conclusions

Numerical modeling results suggest that, under the model assumptions, in the equilibrium states of tidal basins, both volume and area hypsometries of back-barrier tidal flats are dependent on the basin scale and tidal range, i.e. large basin areas and low tidal ranges favor pronounced concave-up hypsometries, whereas small basin areas and high tidal ranges favor subdued concave-up hypsometries. As shown in this paper, such relationships can be caused by tidal currents alone. In addition to the traditional theory of the relative importance of tidal currents and wind waves, the relative tidal flat area is another possible interpretation of the effects of basin area and tidal range on the back-barrier tidal flat hypsometry. The interpretation is that, for channels having a relatively large area in the basin, the development of the tidal flats between channels is restrained, preventing the flats from growing upward to high elevations. As a result, a pronounced concave-up hypsometry is formed, which is associated with relatively large areas of low tidal flats and small areas of high tidal flats. Basins with large areas and low tidal ranges have large relative channel areas, which results in a pronounced concave-up hypsometry, and vice versa.

6. Modeling the Formation of a Sand Bar within a Large Funnel-shaped, Tide-dominated Estuary: Qiantangjiang Estuary, China

Abstract

The Qiantangjiang Estuary (the outer part being known as Hangzhou Bay) located on the east coast of China is a large funnel-shaped, tide-dominated and well-mixed estuary. The estuarine morphology is characterized by a large sand bar having a total length of 125 km and an elevation of 10 m above the average depth of the adjacent seabed. In order to investigate the physical processes governing the formation of this morphological feature, two-dimensional depth-averaged process-based morphodynamic modeling (Delft3D) was carried out on a schematized funnel-shaped domain with exponentially decreasing widths based on the dimensions of the Qiantangjiang Estuary. Starting from a longitudinally regularly sloping bed, the model was driven by the M2 tide with a 2.5 m range at the seaward boundary and a constant river discharge of $10^3 \text{ m}^3 \text{ s}^{-1}$ at the landward boundary, the parameters being compatible with *in situ* observations. The model simulated a 6,000-year period, the output showing the development of a sand bar that reached equilibrium within about 3,000 years. The general shape, size and position of the modeled sand bar are consistent with the observations. Short-term simulations of hydrodynamic and sediment transport processes at the initial stage indicate that, in response to the interactions between river discharge and tidal currents, which are strongly influenced by the funnel-shape, the sand bar developed in the transition zone between the river-dominated upper estuary and the flood-dominated lower estuary where sediment transport pathways converge. A series of sensitivity analyses suggest that the estuarine convergence rate, sediment supply, and river discharge are the main controlling factors of sand bar formation. Similar to other large funnel-shaped, tide-dominated estuaries of the world, a sufficient supply of fine cohesionless sediment (derived from the adjacent Changjiang Estuary), a large river discharge, and a strong shoreline convergence rate have shaped the large sand bar in the Qiantangjiang Estuary.

6.1. Introduction

In association with the decelerating sea-level rise during the Holocene, numerous morphological features developed along coasts where the sediment-laden freshwater of rivers meet the salt water of the advancing sea (Stanley and Warne, 1994). The two most distinctive of these are deltas and estuaries. Deltas are recognized as discrete bulges in the shoreline where the associated rivers deliver more sediment than the rising sea can accommodate or marine processes can redistribute (Swift and Thorne, 1991; Bhattacharya, 2003). By contrast, where both fluvial and marine sediment supply are insufficient to fill the drowned river valleys, the river sections that experience marine influence are called estuaries (Dalrymple et al., 1992; Bhattacharya, 2003).

River discharge, tidal energy flux, and wave action are considered to be the three dominant processes controlling delta morphology (Galloway, 1975). This concept can also be applied to estuaries, among which tide-dominated estuaries are characterized by strong tidal currents transporting more sediment than either river currents or waves (Wells, 1995). Several large tide-dominated estuaries have been studied in detail, e.g., the Cobequid Bay—Salmon River Estuary in the Bay of Fundy (Amos, 1978; Dalrymple et al., 1990) and the Bristol Channel—Severn Estuary in western England (Harris and Collins, 1985; Harris, 1988; Allen, 1990), and today form the basis for the generalized tide-dominated estuarine morphological and faces model conceptually defined by Dalrymple et al. (1992) and Dalrymple and Choi (2007). However, as noted by Dalrymple and Choi (2007), individual cases must be examined critically within the generalized concept.

The Qiangtangjiang Estuary (QE) on the east coast of China is one of such cases. It is a large funnel-shaped, tide-dominated and well-mixed estuary located just south of the Changjiang (Yangtze) Estuary covering an area of about 2000 km² (Fig. 6.1 and 6.2). The most significant morphological aspect is the presence of a large sand bar within the estuary between the laterally averaged longitudinal bed profile and the straight, sloping bed trend (Fig. 6.3) (Chien et al., 1964). Because this large sand bar looks like

a doorsill connecting the interior of a house (land) with the outdoor area (sea), it is called “sandy doorsill” in Chinese.

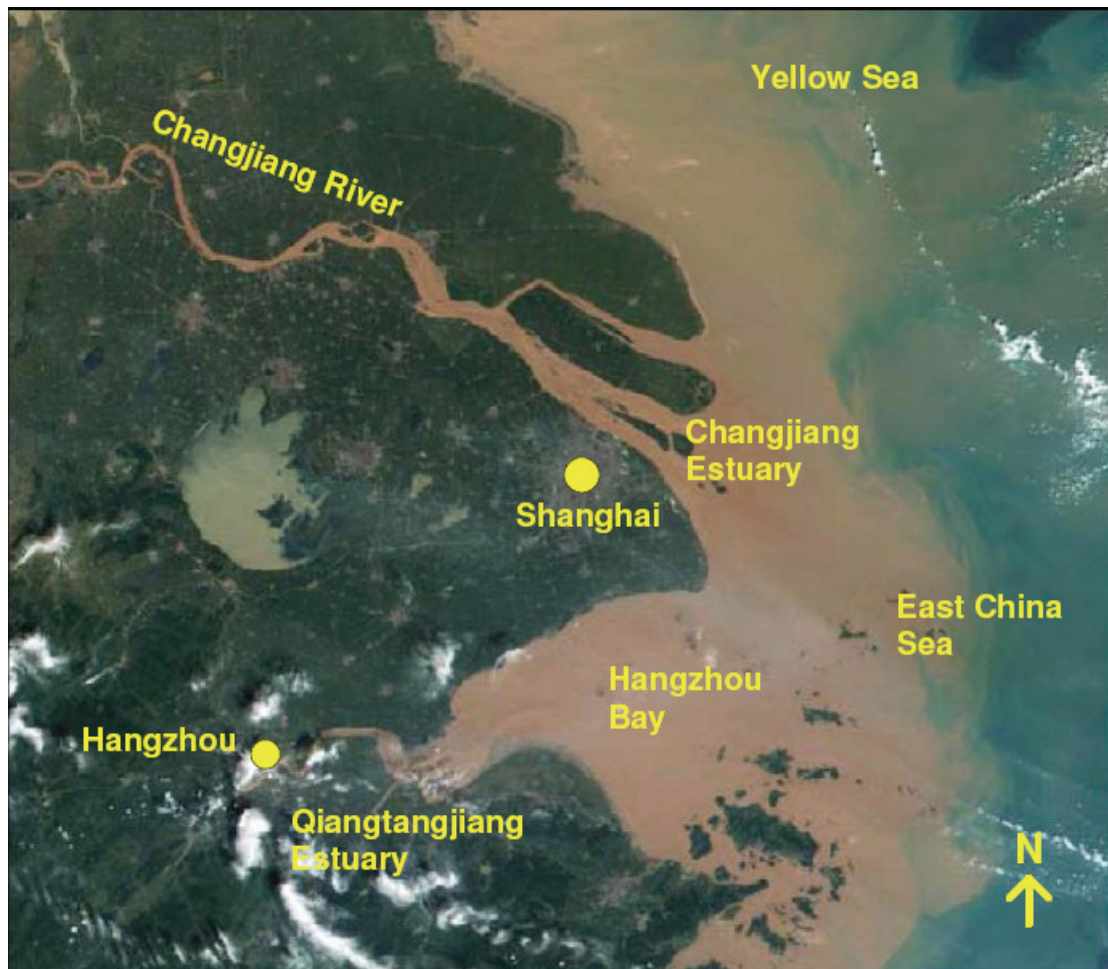


Fig. 6.1. Annotated satellite image showing the location of the Qiantangjiang Estuary, Hangzhou Bay, and the Changjiang (Yangtze) River and Estuary along the east coast of China.

The historical evolution and dynamic processes forming the large sand bar were studied in the early 1960s by the evaluation of historical documents, morphological and sedimentological surveys, and hydrodynamic and sediment transport observations (Chen et al., 1964; Chien et al., 1964). On the basis of this data it was suggested that, following the formation of the funnel-shaped estuary, a large amount of sediment originating from the Changjiang River was transported into the estuary by the strongflood-dominated tidal currents to form the large sand bar. However, this concept

has to date not been verified by more quantitative investigations of these processes in combination with the influence of associated forcing factors such as sediment supply, river discharge, and estuary shape.

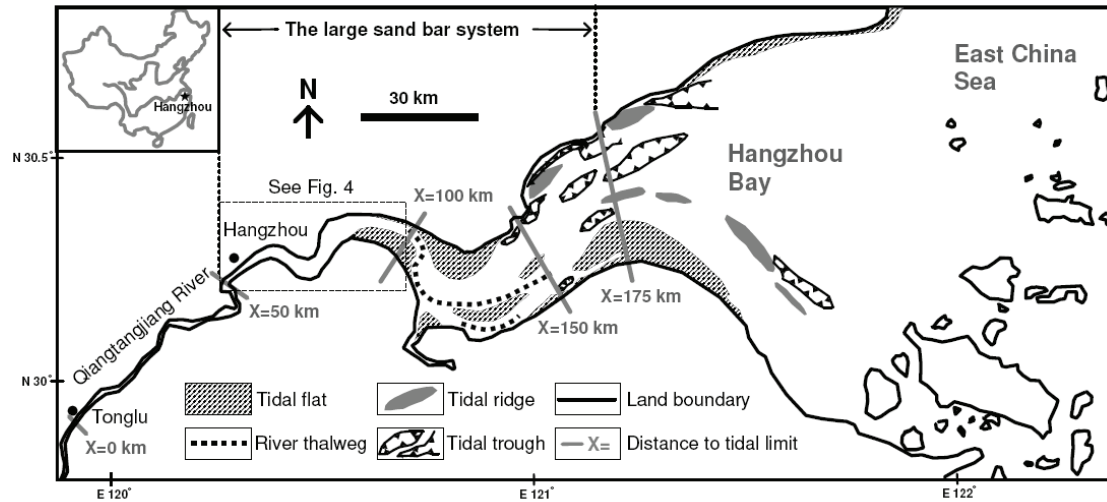


Fig. 6.2. Morphological map of the Hangzhou Bay-Qiantangjiang estuary (modified after Chen et al., 1964, and Feng et al., 1990).

This problem not only applies to the QE, but also to most other large tide-dominated estuaries and, in particular, also to the generalized estuarine facies model. Being one of the most striking features of the overall estuarine morphology, such bulges (i.e. the large bars) in the straight, sloping bed trends have received surprisingly little attention. Although it is well-known that the bars form naturally as a consequence of the decrease in river power and the concomitant increase in the strength of the tidal current, little work has been carried out on the quantification of how the bars scale with the different forcing factors in the estuaries (Bhattacharya, 2003).

In recent years, idealized analytical methods have been used to explain tide-dominated estuarine morphologies (e.g., Schuttelaars and de Swart, 2000; Prandle, 2004), but with increasing complexity, numerical models offer more information on system evolution, although they are generically not easily understood compared with analytical models (Dronkers, 2005). Due to the advantages in

interpreting field observations and analyzing the sensitivity to different parameters, numerical modeling is considered a useful tool to study the morphodynamics of coastal systems (Dronkers, 2005; de Swart and Zimmerman, 2009). In the recent past, one-dimensional (1D) models have been solved numerically in order to assess the long-term morphological evolution and equilibrium of tide-dominated, well-mixed estuaries (Lanzoni and Seminara, 2002; Hibma et al, 2003b; Todeschini et al., 2008), the results emphasizing the crucial role of the convergence rate of the opposing estuarine shorelines on the longitudinal bed profiles.

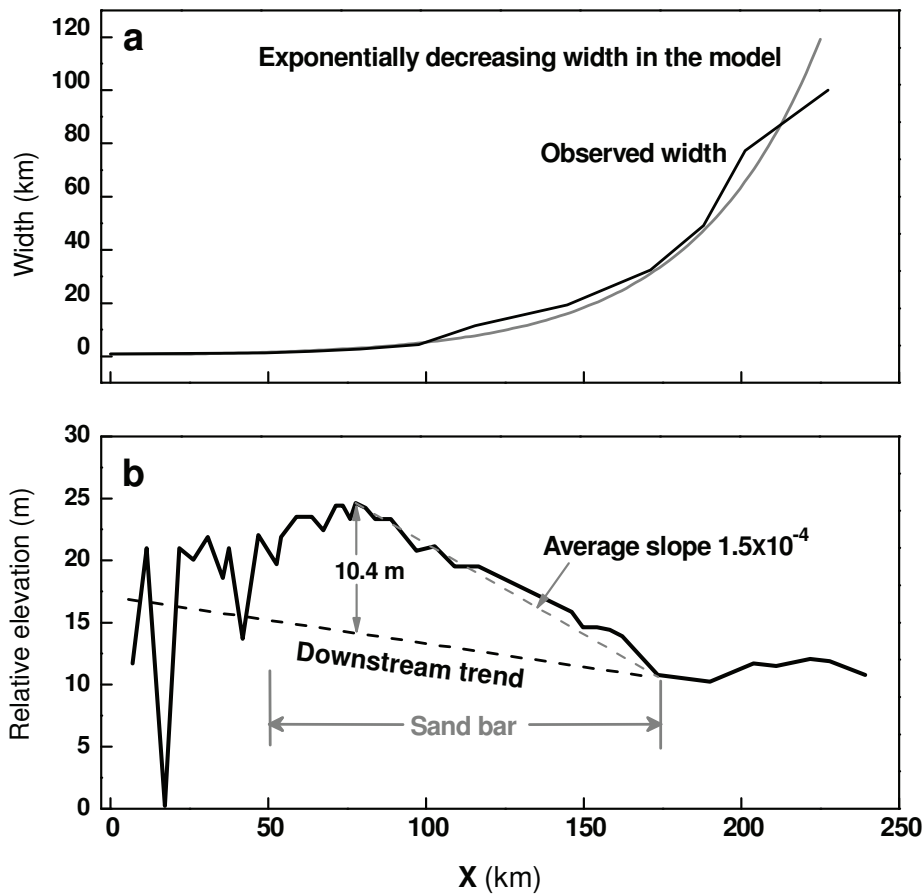


Fig. 6.3. (a) Comparison of the observed width of the Qiangtangjiang Estuary with the exponentially increasing width used in the numerical model as described by eq. (6.1). (b) Observed average longitudinal bed profile of the Qiangtangjiang Estuary (modified after Chien et al., 1964) showing the large sand bar elevated above the mean bed slope trend downstream of Tonglu (see Fig. 6.2).

Applying newly developed numerical modeling techniques (Lesser et al., 2004; Roelvink, 2006), it has become possible to study long-term estuarine morphodynamics by means of two-dimensional, depth-averaged (2DH) process-based models (Hibma et al., 2003a; Montano and Carbajal, 2008; van der Wegen and Roelvink, 2008; van der Wegen et al., 2008). In this way it has been possible to reconstruct morphological evolution histories and to simulate the formation of channel and shoal patterns.

However, two important factors are not incorporated in the above modeling approaches. The first factor is sediment supply, including the rate and the character (e.g., cohesive properties and grain size) of sediment input from both the river and the open sea. This aspect is particularly important as sediment supply has been suggested as one of the key factors controlling estuarine and delta morphology (Harris, 1988; Swift and Thorne, 1991; Orton and Reading, 1993; Gao, 2005). For example, the Bristol Channel—Severn Estuary is a typical sediment-starved estuary (Harris and Collins, 1985), whereas the sand composing the elongate tidal bar systems in the head section of the Cobequid Bay—Salmon River Estuary originated from the landward sorting of downstream glacial deposits (Dalrymple et al., 1990). In the case of the QE, a large contribution of cohesionless silt from the neighboring Changjiang River has been suggested by Chen et al. (1964) and Chien et al. (1964). However, most of the previously applied numerical models have merely assumed a fixed grain size and a sufficient sediment supply. Consequently, the morphological response of estuaries to different sediment supply conditions is still poorly understood.

River discharge is another important factor. Most of the previous models neglected variable river discharge at the landward boundary assuming that it was much less than the prevailing tidal discharge. However, although tides dominate over most of an estuary, river discharge and sediment supply may play an important role at the landward end where smaller channel cross-sections and tidal prisms prevail (Perillo, 1995; Todeschini et al., 2008). As a result, the question on whether and how river discharge influences the estuarine morphology remains problematical, even if it is

generally much smaller than the tidal discharge and the estuary remains well-mixed.

In view of this situation, the following questions may be raised in connection with the Qiantangjiang Estuary: Focusing on the estuarine longitudinal bed profile, (1) how can the formation process of the large sand bar in the QE be quantitatively reconstructed, and (2), in comparison with other large tide-dominated estuaries, how can the effects of estuarine convergence, sediment supply and river discharge in the generalized estuarine morphological model be evaluated?

In the present contribution, an attempt is made to answer the above questions by applying a physically-based numerical modeling technique. Owing to the complexity of tide-dominated estuaries associated with interactions of numerous physical, chemical and biological processes, and irregular and variable boundary conditions (Wells, 1995; Dalrymple and Choi, 2007), the numerical modeling approach has been simplified to the extent that only key processes and configurations were considered, from which the first-order dynamics could be extracted and anomalous and idiosyncratic situations could be identified (Paola, 2011). By this approach it was hoped to obtain an improved understanding of the morphodynamics and the resulting morphology of large tide-dominated estuaries. It is emphasized that the present study only concentrates on the large sand bar along the laterally averaged longitudinal bed profile, and not on the estuarine infilling history (e.g., Lin et al., 2005) or the development of lateral channel and ridge patterns (e.g., Hibma et al., 2003a; Xie et al., 2009).

6.2. Study area

The QE (the outer part being known as Hangzhou Bay) is located on the east coast of China, immediately south of the Changjiang Estuary (Fig. 6.1). It is the biggest estuary along the East China Sea coast of China, its typical funnel shape having formed around 3,000–4,000 years BP (Chen et al., 1964). The length of the estuary from the landward tidal limit to the estuarine mouth is around 250 km, and the width

decreases rapidly from 100 km at the mouth to around 1 km at the landward limit of tidal influence (Fig. 6.2 and 6.3a). The southern part of the wide mouth, which connects with the East China Sea, is protected by numerous small islands, while the northern shore converges on the southern tip of the outer Changjiang Estuary (Fig. 6.1 and 6.2).

The estuary can be divided into three morphological sections: an upper section from $x = 0$ to $x = 50$ km, a middle section from $x = 50$ to $x = 150$ km, and an outer section where $x > 150$ km, the origin of the x -coordinate being located near the landward tidal limit (see Fig. 6.2, Chien et al., 1964; Lin et al., 2005). The upper section of the estuary is a stable anabranching channel, which is dominated by fluvial processes. Due to the interaction of fluvial and tidal processes, the middle section is characterized by a shallow and wide estuarine bed with a laterally migrating channel thalweg lined by unstable intertidal flats. Figure 6.4 illustrates the position of the thalweg in the upper part of the middle section recorded between March 1953 and December 1958, illustrating the pronounced lateral migration across the whole estuary. The marine dominated outer section is also called Hangzhou Bay where the strong tidal currents have formed a ridge and swale topography. Seaward of this the bed is relatively flat.

The most striking morphological feature of the QE is the presence of a large sand bar. Figure 6.3b shows the laterally averaged longitudinal bed profile of the QE, along which the large sand bar can be clearly indentified as a bulge above the straight, uniformly sloping bed trend. The body of the large sand bar extends from $x = 50$ to $x = 175$ km, having a total length of around 125 km, and a peak crest height of 10.4 m above the base line. The front slope of the sand bar is $1.5 * 10^{-4}$, where the dimensionless slope is defined as the tangent of the angle of the slope.

The bed of the QE is quite unstable because of the intensive channel migration associated with erosion and deposition (Zhou and Gao, 2004), although the longitudinal profile has been relatively stable from the 1910s to the 1950s, suggesting that the large sand bar has attained an equilibrium state (Chien et al., 1964). Recent

observations indicate that, associated with intensified land reclamation over the past several decades, the estuary has generally experienced renewed infilling between 1981 and 2005 (Guo et al., 2009).

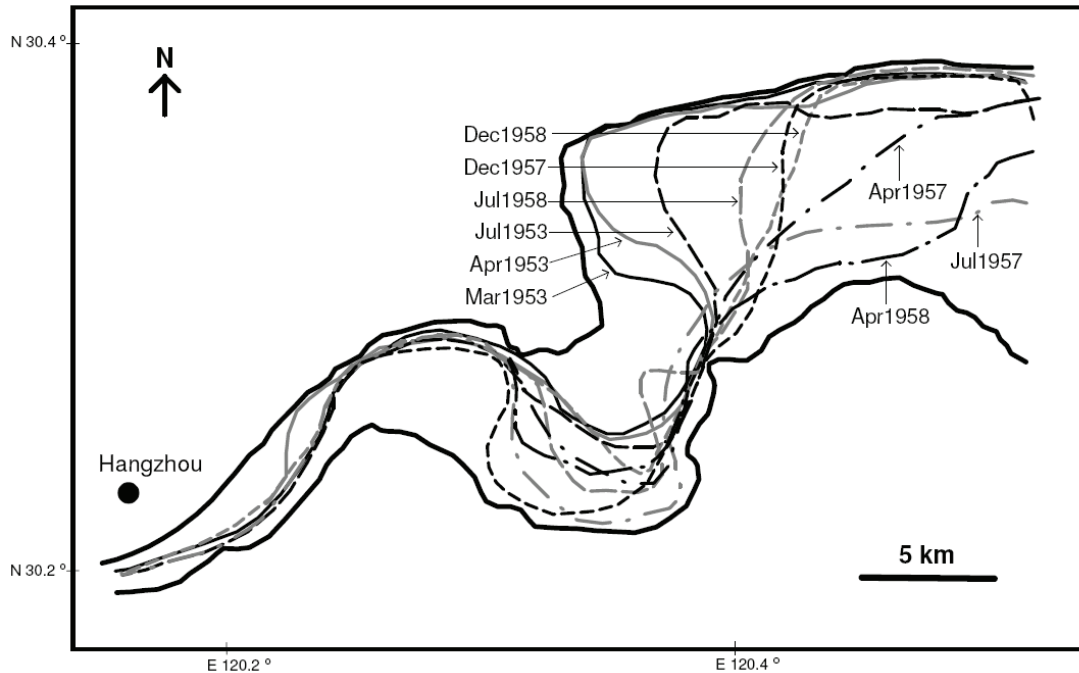


Fig. 6.4. Lateral migration of the channel thalweg recorded in the upper part of the middle section of the Qiantangjiang Estuary (the area in marked in Fig 2) between March 1953 and December 1958 (modified from Chien et al., 1964).

On a longer time scale, Chen et al. (1964) have suggested that the basic shape of the sand bar has evolved around 2,500 years BP, following the establishment of the funnel-shaped geometry of the QE some 1,000 years earlier. After initiation, the sand bar gradually prograded seaward while growing in height. During this period, sea-level has remained stable (Chen and Stanley, 1998; Hori et al., 2001).

The Qiantangjiang River is the main source of freshwater and sediment to the QE (Su and Wang, 1989). The average water discharge is $952 \text{ m}^3 \text{ s}^{-1}$, and the annual average river sediment flux is around 6 million tons, consisting mainly of coarse silt to fine sand (Chien et al., 1964; Su and Wang, 1989; Pan and Huang, 2010). Most of the

discharged sediment is trapped in the estuary and only the finest portion escapes into the East China Sea (Su and Wang, 1989). The adjacent Changjiang River, which has an average water discharge of $29,000 \text{ m}^3 \text{ s}^{-1}$ and an annual average sediment flux of 486 million tons, is another major sediment source that plays a key role in the morphological evolution of the QE (Chen et al., 1964; Su and Wang, 1989).

The entire estuary is mainly occupied by well sorted fine-grained cohesionless sediment having median grain sizes between 20 and 40 μm , the clay component (finer than 4 μm) contributing less than 3%, which explains the cohesionless dynamic nature (Chen et al., 1964; Dyer, 1986; Zhou and Gao, 2004). The sediment can be classified as sortable silt, which is predominantly transported as single grains and forms the cohesionless part of the mud fraction (size range $<63 \mu\text{m}$) (Bartholdy, 1985; McCave and Hall, 2006; Chang et al., 2007). The homogeneous distribution of the cohesionless silt is another principal feature of the QE.

The tide is the main driving force in the QE, the dominant tidal component being the M2 constituent (ECCHE, 1992; Xie et al., 2009). According to the definition of Dyer (1997), the QE is a typical hypersynchronic estuary. Because of the funnel-shaped geometry, the average tidal range increases from 2–3 m at the mouth to more than 4 m at $x = 125 \text{ km}$, after which the friction offsets the influence of convergence, causing the tidal range to progressively decrease to zero at the upper tidal limit (Zhou and Gao, 2004; Lin et al., 2005). The strong tidal influence destroys any vertical stratification to produce the well-mixed nature of the QE (Mao et al., 1964; ECICTZ, 1988). Because of the protection by islands at the mouth, the wave climate is dominated by local wind waves, mean annual wave heights decreasing from 0.5 m at around $x = 225 \text{ km}$ to 0.2 m at around $x = 175 \text{ km}$, and even less in the middle and inner sections (Han et al., 2003). As a consequence, wave action contributes very little to the morphology of the estuary.

6.3. Methods

6.3.1. Model description

In order to examine in detail how the large sand bar in the QE formed and what the influence of estuarine convergence, sediment supply and river discharge was on the longitudinal bed profile, a 2DH process-based morphodynamic model (Delft3D software package) was used. Delft3D has been utilized and validated widely in different coastal environments to simulate longterm morphodynamic changes on different time scales (e.g., Dastgheib et al., 2008; Edmonds and Slingerland, 2010), including tide-dominated well-mixed estuaries (Hibma et al., 2003a; van der Wegen and Roelvink, 2008; van der Wegen et al., 2008). Xie et al. (2009) applied Delft3D to the QE, obtaining a reasonable similarity in the channel pattern when comparing the observational data with the results of a 30-year modeling period.

In the model, and in accordance with the tide-dominated well-mixed characteristics, only tidal forcing and river discharge were considered, neglecting vertical velocities, density differences, as well as wind and waves (Dastgheib et al., 2008; van der Wegen and Roelvink, 2008; van der Wegen et al., 2008). On the other hand, the Coriolis force was taken into account in the model due to the large spatial scale. The 2DH continuity equation and nonlinear, shallow-water momentum equations for incompressible free surface flow are solved numerically with a constant seabed drag coefficient of $3 * 10^{-3}$ (Soulsby, 1997; de Swart and Zimmerman, 2009). The effects of flooding and drying are solved by a free slip assumption, in which, if the bed emerges above a critical flow depth (0.1 m in this study), this cell is set dry without current velocity. An alternate direction implicit time-integration method is used for the numerical solution. A detailed description of the Delft3D flow model can be found in Lesser et al. (2004) and van der Wegen and Roelvink (2008).

Sediment transport is calculated by the van Rijn approach for single-size cohesionless grains (Dissanayake et al., 2009). The standard advection-diffusion equation is adopted for suspended sediment transport and the Exner equation is employed for

both suspended load and bedload to simulate the morphological changes based on the sediment mass conservation law.

When using multi-sized sediments, the same van Rijn approach and advection-diffusion equation were applied, but the reference concentration, erosion rate and sediment transport rate of each sediment fraction were considered proportional to the availability of each fraction on the bed (Guillou et al., 2009; van der Molen et al., 2009). The bed composition model was changed from a uniformly mixed bed (one sediment layer) for a single-size sediment to a multi-layer concept for multi-sized grains (Edmonds and Slingerland, 2010; Geleynse et al., 2010). The model defines a transport layer with a fixed height of 0.1 m and a maximum number of 50 bookkeeping layers (each 0.2 m thick) to keep track of sedimentary stratigraphy (Edmonds and Slingerland, 2010; Geleynse et al., 2010). Net deposited sediment is initially added to and mixed into the top-most layer until the defined constant thickness of 0.2 m is exceeded, after which a new bookkeeping layer is created. When net erosion takes place, only sediment in the top-most layer is available. In this way, the bed armoring phenomenon can be simulated, which results in lag deposits composed of coarser sediment fractions that prevent the covered finer sediments from being eroded (Flemming et al., 1992; Wiberg et al., 1994; Reed et al., 1999). Further details can be found in the Delft3D flow manual.

As longterm modeling is demanded, the "online" approach is used to save calculation time. It speeds up bed adjustments by multiplying the bed sediment flux in each time step by a morphological scaling factor (MF). This method, which was originally invented by Roelvink (2006), was subsequently successfully applied in longterm morphological modeling with a typical MF in the order of 100, e.g., Dastgheib et al. (2008) used an MF of 300, van der Wegen and Roelvink (2008) and van der Wegen et al. (2008) an MF of 400, whereas Edmonds and Slingerland (2010) used an MF of 175. In the present model, an MF of 365 was chosen for saving simulation time.

6.3.2. Model setting

As outlined above, a physics-based 2DH longterm morphological numerical model with simplified setting was chosen for the present study. The philosophy is that, given that only principal characteristics of the QE are adopted and key processes of sediment transport are involved, the model is kept as simple as possible. Although certain details can not be reproduced for comparison with real world observations, the aim is to catch the first-order dynamics of large sand bar formation. The simplified model setting also allows the modeling results to be used in a more universal sense by providing a generalized understanding of estuarine morphology, instead of being limited to the special case of the QE only. In addition, with the help of the simplified setting, it is relatively convenient to study the contributions of different factors, including estuarine convergence, sediment supply and river discharge, which can then be compared with some other large estuaries. Furthermore, the simple setting meets the requirement of saving computational time for longterm morphological modeling.

The simplest model would be one-dimensional in the longitudinal direction, reasonable features of estuarine morphology having been obtained by 1D numerical modeling approaches in which river discharges were excluded (Lanzoni and Seminara, 2002; Hibma et al, 2003b; Todeschini et al., 2008). However, if river discharge at the landward end of the estuary is involved, our own numerical experiments show that continuously supplied river-borne sediment can not escape seaward with the result that continuous accumulation occurs in the low-energy transition zone between the river-dominated and the tide-dominated region. This continuous accumulation between the fixed side boundaries creates an unrealistically high sand bar that indicates the failure of the 1D model. For this reason a 2DH model was employed in this study. Adding the lateral dimension provides the opportunity of the river-borne sediment to be exported via channels fringed by shallow shoals or tidal flats, and which are commonly dominated by ebb tidal currents (Friedrichs and Aubrey, 1988).

Tide-dominated estuaries are usually characterized by a funnel-shaped geometry in plan view, the width of the estuarine section decreasing rapidly landward at an

exponential rate (Wells, 1995). The QE is not an exception in this respect. Figure 6.3a shows that the estuarine width at any particular point is well described by the following exponential equation:

$$W = \begin{cases} 120 \exp \frac{x-225}{40} & x \geq 25 \\ 0.8 & x < 25 \end{cases} \quad (6.1)$$

where W is the estuarine width in km, and x is the distance from the upper tidal limit in km. The numerator of 40 km in eq. (6.1) is called the convergence length and is a measure of the estuarine convergence rate, which means that the width is reduced by a factor of e (natural logarithm) for every 40 km in the landward direction (Lanzoni and Seminara, 2002). Therefore, the larger the convergence length is, the smaller the convergence rate becomes. The part landward of 25 km is mostly a fluvial channel with a constant width of 0.8 km. Consequently, the modeling geometry was schematized to correspond to the exponential convergence shape described by eq. (6.1) in order to resemble the QE (Fig. 6.5a). For the purpose of investigating the influence of estuarine convergence in general, this schematized plan shape can easily be modified by changing the convergence length, which is a suitable method for the study of the principle features of estuarine morphology.

The modeling grid is shown in Fig. 6.5a. The 225 km long longitudinal axis has 150 cells, each having a uniform length of 1.5 km. In the lateral direction, the grid is uniformly discretized into 6 aliquots, *i.e.* the width of each equals 1/6 of the total width of the estuary, increasing from the land to the sea. The high resolution of the longitudinal grid allows a detailed study of the large sand bar dynamics, which is the focus of the present contribution. The lower resolution of the lateral grid reduces the grid number and hence saves computational time. Because lateral morphological patterns can not be described by the limited lateral grid, the study concentrates on the longitudinal profile. To fulfill the stability requirement, a numerical calculating time step of 4 min is prescribed.

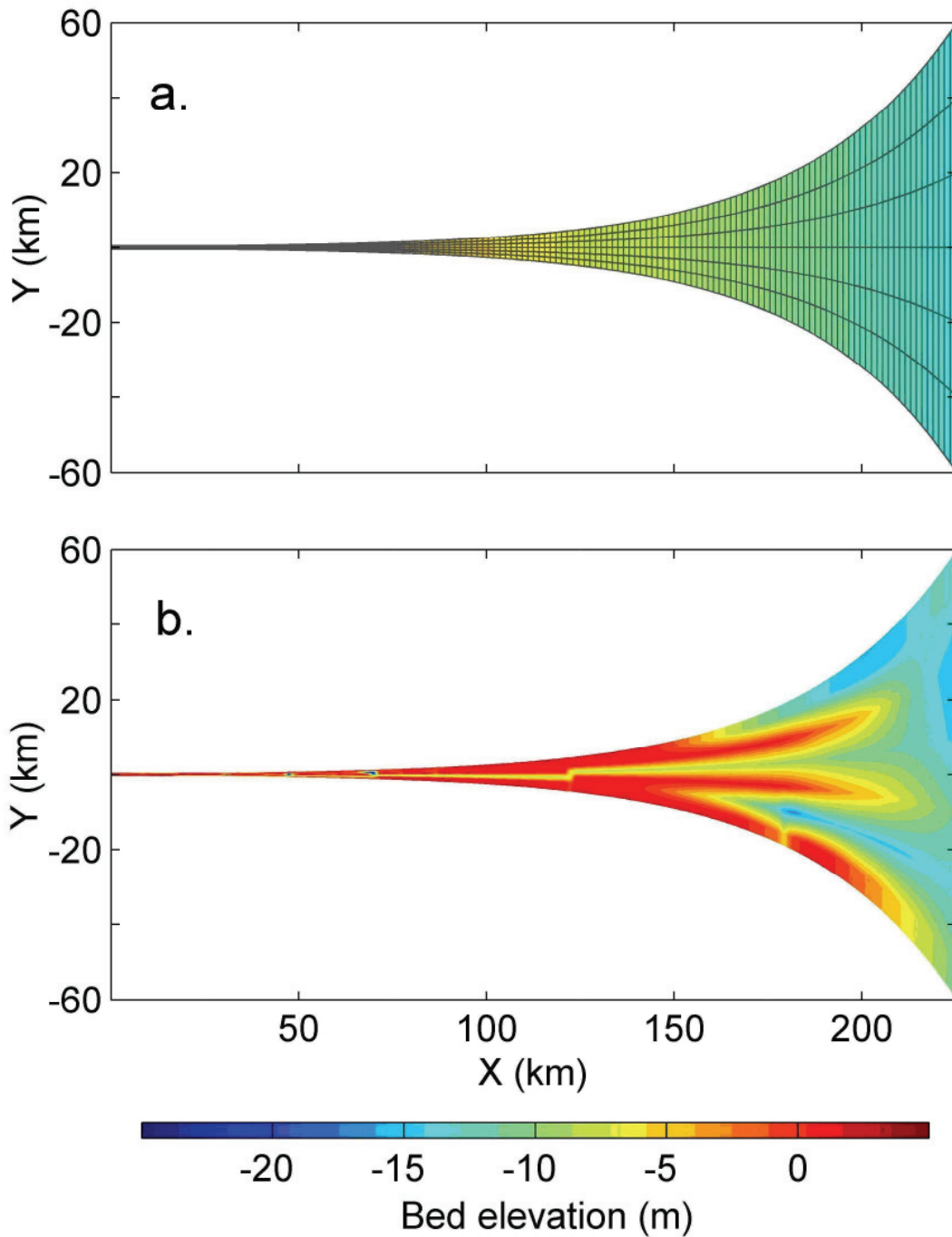


Fig. 6.5. (a) Modeling grid and initial bathymetry of the schematized Qiangtang estuary in the reference case R; (b) final bathymetry after a 6,000 year simulation. Color bar denotes the bed elevation relative to mean sea level (m).

Initially, a laterally uniform and longitudinally inclined bed with a constant slope of 0.6×10^{-4} was set from the land boundary to the seaward mouth, the elevation decreasing from 0 m above mean sea level (asl) at $x = 0$ km to -13.5 m asl at $x = 225$

km, according to the present bathymetry at the upper fluvial channel and at the QE mouth, respectively. This initial bathymetry is based on the consideration that this study aimed at elucidating the formation of the large sand bar from a constant slope, and not to reconstruct the infilling history of the estuary. It is for this reason that the ancient bathymetry of the QE was not adopted.

A single sediment grain size of 64 μm was uniformly distributed in the model domain and forms the smallest cohesionless grain size implemented in the Delft3D software. Although 64 μm is coarser than the observed median grain size of 20 to 40 μm in the QE, it was an obvious choice for two reasons. First, the fundamental dynamic property of the cohesionless sediment in the QE could be preserved if a larger than natural uniform grain size was chosen. Second, the prediction of cohesive sediment transport is more complex and highly sensitive to the input parameters such as the erosion constant, the critical erosion and deposition bed shear stresses, and the sediment bulk density (Whitehouse et al., 2000). Furthermore, due to the lack of field calibration of these parameters, a variety of results could be achieved by changing them artificially.

The land and sea boundaries were forced by tidal and river discharge. At the open sea boundary, only the main M2 tide was taken into account for simplification (Todeschini et al., 2008; van der Wegen and Roelvink, 2008; van der Wegen et al., 2008). According to the observations and the hydrodynamic modeling results of the QE by Xie et al. (2009), a uniform tidal range of 2.5 m across the whole mouth (the open sea boundary) was chosen in order to resemble the real situation. The inland open boundary was defined by a constant river discharge of $1000 \text{ m}^3 \text{ s}^{-1}$, which is in accordance with the hydrography of the Qiangtangjiang River. The lateral boundaries were closed. At the open boundaries of the sea and the inland, dynamic equilibrium concentrations were defined for sediment transport (Hibma et al., 2003b). This definition determines the sediment concentration in the water column at the open boundaries by the local pickup and deposition terms. The relatively shallow water depth at the seaward boundary (13.5 m) and the definition of equilibrium

concentrations implied an abundant sediment availability to be imported through the mouth, which is consistent with the condition of sufficient sediment supply from the Changjiang River into the QE.

Table 6.1. Settings for the sensitivity analysis

No.	Convergence length (km)	Sediment	River discharge (m ³ /s)
case R	40	one fraction of 64 μm	1000
case S	50	one fraction of 64 μm	1000
case G	40	3 fractions of 2000, 500, 125 μm	1000
case R1	40	one fraction of 64 μm	0
case R2	40	one fraction of 64 μm	250
case R3	40	one fraction of 64 μm	2000

NB: Case R is the reference case.

Because the large sand bar has a temporal formation scale of the order of 10³ years (Chen et al., 1964), the model was simulated for 6,000 years to make sure that the system was able to reached equilibrium.

6.3.3. Sensitivity analysis

A sensitivity analysis was carried out to evaluate the effects of estuarine convergence, sediment supply, and river discharge on the longitudinal profile, which may improve the understanding of the generalized estuarine morphological model. In addition, some of the results of the sensitivity analysis would be suitable to be compared with other large tide-dominated estuaries because they share similar key forcing factors. The settings of the sensitivity analysis are summarized in the Table 6.1.

At first, the estuarine convergence rate was modified. Based on eq. (6.1), which represents the geometry of the reference case (case R), the case S was designed with a slower convergence rate using the following equation:

$$W = 120 \exp \frac{x - 225}{50} \quad (6.2)$$

As can be seen, the convergence length was modified from 40 km in eq. (6.1) to 50 km in eq. (6.2), but the estuarine mouth width of 120 km was kept the same. One of the considerations to choose this design for the analysis was that, due to the completed and still planned land reclamations during the past several decades and in the future, respectively, the geometry of the QE tends to be changed, causing a stronger degree of convergence. A sensitivity analysis on the influence of convergence length is therefore useful to evaluate the impacts of these construction activities on the estuarine morphology.

In a second step, the influence of sediment supply was investigated. As outlined above, the QE is fed by a sufficient amount of fine cohesionless sediment both from the river and from the Changjiang Estuary through the estuary mouth, whereas the Bristol Channel—Severn Estuary and the Cobequid Bay—Salmon River Estuary are characterized by limited sediment supply. This contrast should result in a significant difference in the morphology. In the present study, the Cobequid Bay—Salmon River Estuary was taken as the prototype for the sensitivity analysis in the case G employing three typical grain sizes, namely -1ϕ (2000 μm), 1ϕ (500 μm), and 3ϕ (125 μm) representing a gravel/very coarse sand, a coarse/medium sand, and a fine/very fine sand fraction, respectively. Initially, the three fractions were equally weighted and well-mixed in the stratigraphy with a uniform distribution over the entire model domain. The multi-sized sediment transport model was then used to simulate the co-evolution of the morphology and the grain-size distribution.

The third series of sensitivity analysis was on the river discharge effect. The discharge of $1000 \text{ m}^3 \text{ s}^{-1}$ in the reference case R matches the situation of the QE but is substantially lower in the case of some other large tide-dominated estuaries. For example, the River Severn has an average annual discharge of $107 \text{ m}^3 \text{ s}^{-1}$ (Centre for Ecology and Hydrology, Natural Environment Research Council, UK), that of the Salmon River is approximately $10 \text{ m}^3 \text{ s}^{-1}$ (Dalrymple et al., 1990), while the Gulf of Kachchh, India, lies in a semi-arid region with small river discharge (Chauhan et al., 2006). In accordance, three test cases were designed with river discharges of 0, 250,

and $2000 \text{ m}^3 \text{ s}^{-1}$, respectively. This analysis was in addition considered useful for an assessment of potential estuarine response to variations in river discharge in the course of future climate change.

6.4. Results

6.4.1. Reference case R

The bathymetric map of the whole domain of reference case R after a 6,000-year modeling period is illustrated in Figure 6.5b. Although the lateral patterns are excluded from the present study because of the limited number of lateral cells, it is noted that the final bathymetric map indicates the formation of channels through which river water and sediment can be exported once the final morphological equilibrium is achieved. It also demonstrates the fundamental advantage of the 2DH model compared to the 1D model.

The longterm evolution of the longitudinal bed profile in the case R is shown in Fig. 6.6a. It can be seen that sediment accumulates in the middle part of the estuary and that the basic feature of the large sand bar emerges after 1,000 years. It then continues to gradually grow until, after 3,000 years, the shape of the sand bar approaches a stable form, suggesting that the equilibrium configuration is reached asymptotically. Compared to the 1,000 year situation, the height of the bar only increased by about 1 m, but the position of the maximum height moved seaward from $x = 100 \text{ km}$ to $x = 130 \text{ km}$, the final profile having a relatively flat top between these two positions. On the equilibrium bed profile, the large sand bar can be identified between $x = 50 \text{ km}$ and the estuary mouth, having a front slope of $1.5 * 10^{-4}$ and a peak crest height of 7.8 m above the initial bed level (Fig. 6.6b).

In Fig. 6.7, the hydrodynamics at the final equilibrium state are evaluated. Four features concerning the current velocities at $x = 45, 90, 135$ and 180 km can be distinguished in the time series. First, the tidal phase is delayed by 1 to 1.5 hour every 45 km from the estuary mouth toward the land. Second, the velocity amplitude

increases between $x = 180$ and $x = 135$ km, and then declines landward, indicating a hypersynchronous condition. Third, tidally induced currents dominate most of the estuary, as indicated by similar maximum flood and ebb current speeds, except that at $x = 45$ km the seaward current is substantially intensified, which suggests a contribution from river discharge. Fourth, because of bed friction the incoming temporally symmetrical tide is modified, the flood phase having a shorter period than the ebb phase.

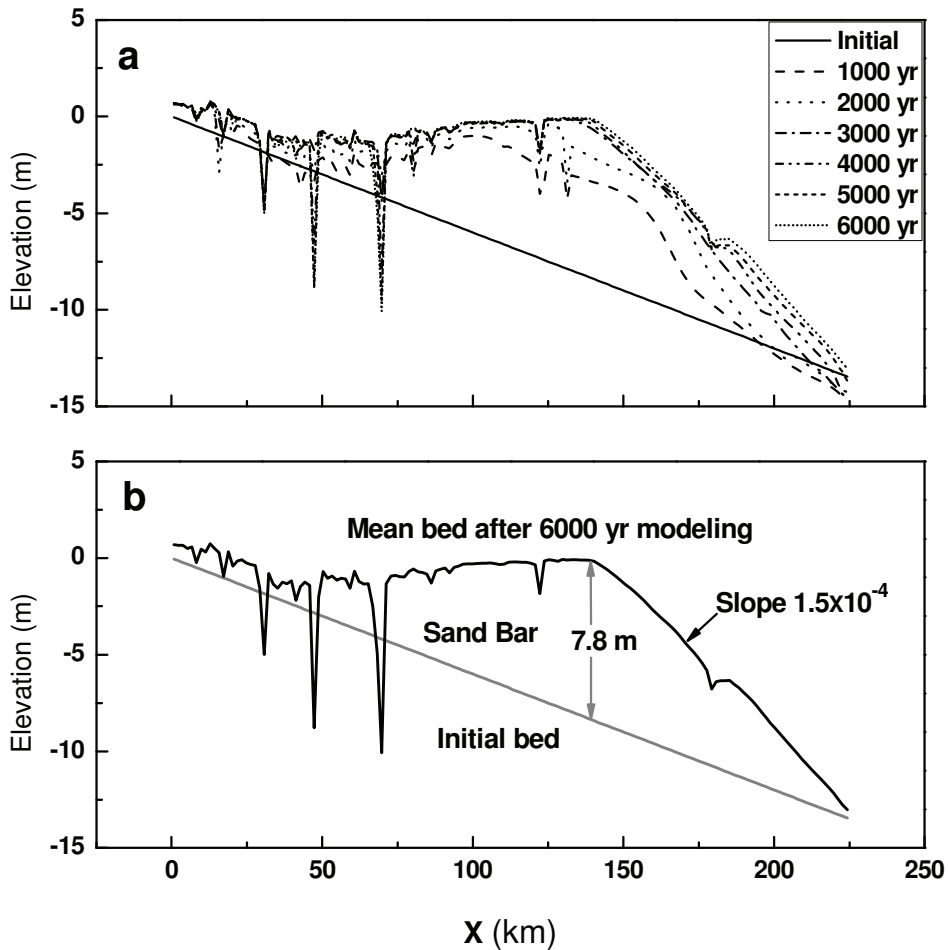


Fig. 6.6. (a) Longterm evolution of the longitudinal bed profile of the case R; (b) the final (6,000 years) equilibrium mean longitudinal bed profile outlining the large sand bar.

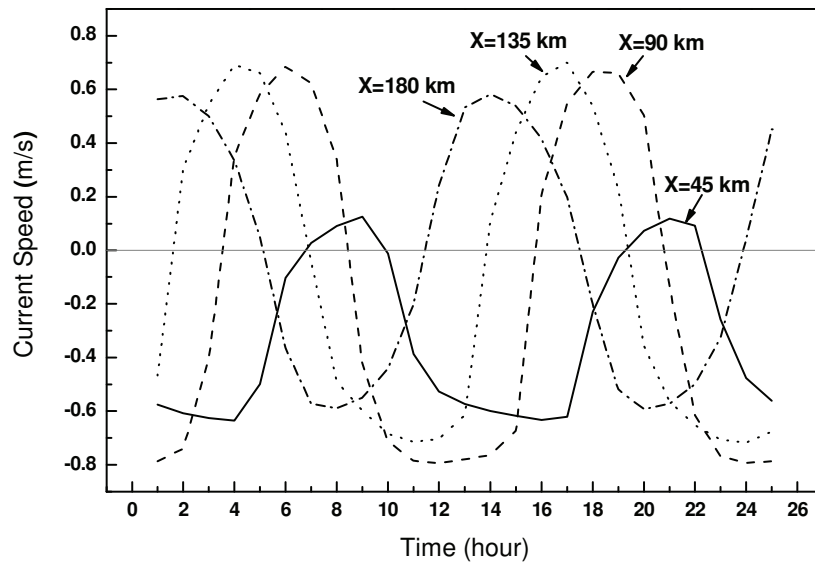


Fig. 6.7. Time series of the current velocities in the case R at the final state, positive values denoting the flood, negative values the ebb current.

The longitudinal hydrodynamic and sediment transport situations at the initial and final states of case R are illustrated in Fig. 6.8 and Fig. 6.9, respectively. At the initial state, the longitudinal profile shows the typical hypersynchronous character, the tidal range initially increasing from the mouth to the central estuary, from where it progressively decreases landward to finally peter out (Fig. 6.8a). The maximum flood speed is higher than the maximum ebb speed from $x = 225$ to $x = 50$ km, the difference increasing from the mouth. When approaching $x = 45$ km, this difference decreases to zero and then, along with the rapidly decreasing maximum flood speed, the system is overturned and now has a higher maximum ebb speed (Fig. 6.8b). In Fig. 6.8c, the intensity of river discharge is locally represented by the absolute value of the residual velocity, the tidal current speed being represented by half of the difference of the maximum (positive) and minimum (negative) current velocity, the total energy being estimated by the maximum current speed. It can be seen that, associated with the landward increase in river and decrease in tidal contribution, the total energy is

initially enhanced from the mouth landward due to the increase in the dominant tidal current, but then reaches a trough at a location close to the turning point between the dominance of the maximum flood and ebb speeds shown in Fig. 6.8b.

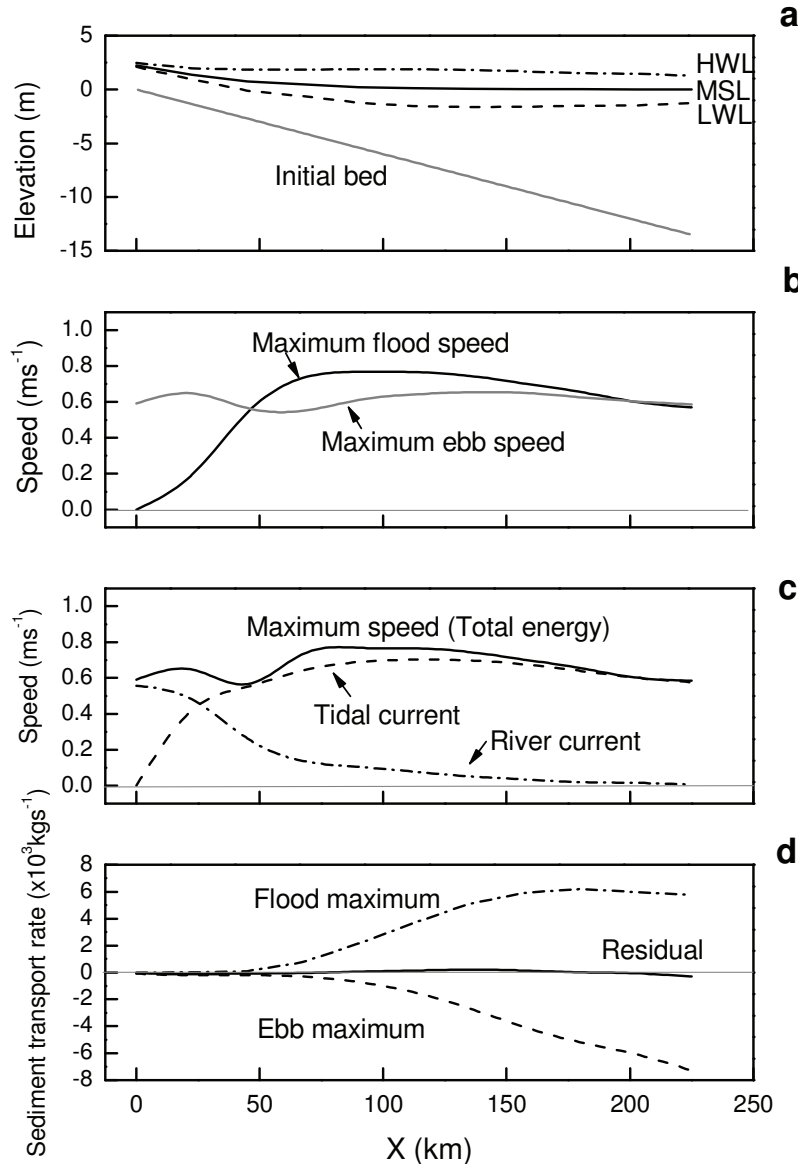


Fig. 6.8. The longitudinal distribution of hydrodynamics and sediment transport at the initial state of case R. (a) The high-water level (HWL), mean sea level (MSL) and low-water level (LWL). (b) Maximum current speeds during flood and ebb tides. (c) Intensity of the river current as represented by the absolute values of the residual velocity, the tidal current being represented by the half values of the difference between the maximum (positive) and minimum (negative) current velocities, and the total energy being defined by the maximum current speeds. (d) The maximum cross-sectional sediment transport rates during flood and ebb tides, and the residual sediment transport rates.

The maximum cross-sectional sediment transport rates during the flood and ebb tides are shown in Fig. 6.8d, indicating that, in the middle part of the estuary, sediment transport is significantly higher during the flood phase as compared to the ebb phase. As a consequence, the estuary has a large accommodation space, allowing sediment supplied from both the river and the sea to accumulate.

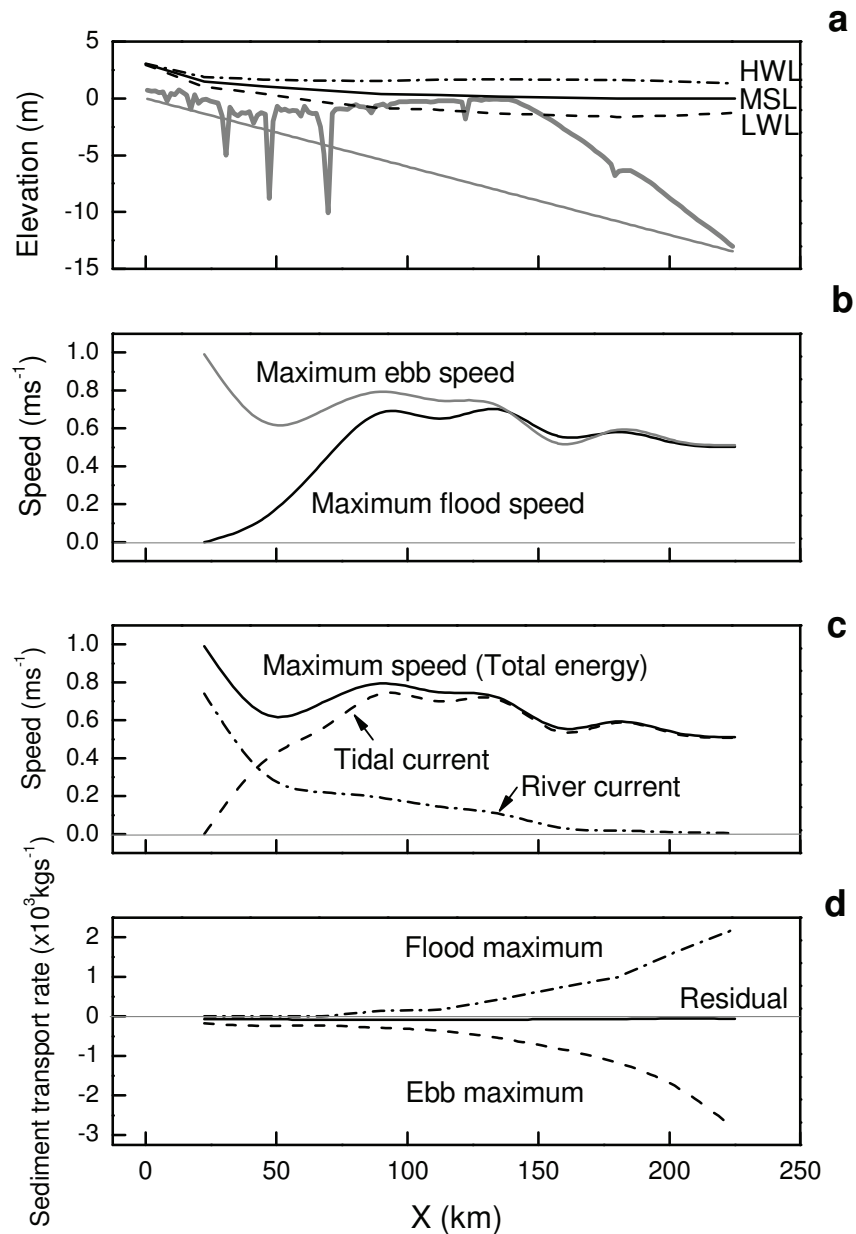


Fig. 6.9. Longitudinal distribution of hydrodynamics and sediment transport at the final equilibrium state of case R illustrated by the same panels as in Fig. 6.8.

The longitudinal variations of the same parameters at the final equilibrium state of the morphological evolution are illustrated in Fig. 6.9. As can be seen in Fig. 6.9a, a large sand bar has formed, the crest approaching the mean sea level. As a consequence, a complete change is observed with respect to current dominance (Fig. 6.9b), the maximum ebb speed now exceeding the maximum flood speed over most of the estuary. In Fig. 6.9c, the longitudinal patterns of river current, tidal current and total energy are almost the same as during the initial state, except that the peaks of the curves have shifted. The enhanced ebb current in Fig. 6.9b is responsible for the amplified ebb sediment transport shown in Fig. 6.9d. As a consequence, excess sediment supplied by the river can now be exported, causing net sediment accumulation to approach zero as morphological equilibrium is reached. The estuary is thus gradually transformed from a sink for sediment derived from both land and sea to a transit area that is bypassed by sediment supplied from the river, while sediment formerly entering the estuary from the seaward side is blocked because the accommodation space has disappeared. In this respect, the estuarine system is similar to the graded river concept, which describes the long-term equilibrium state of a river system subject to steady allogenic forcing (Mackin, 1948).

In Fig. 6.10, the initial and final states concerning the tidal range, cross-sectional residual sediment transport rate, and net accumulation for case R are compared. Because the evolution of the large sand bar induces a progressively stronger bottom friction, the initial state has an overall higher tidal range. The turning point where the initial increase in tidal range (hypersynchronous mode) reverses to a decreasing range (hyposynchronous mode), has shifted seaward in spite of the fact that the maximum tidal ranges are almost the same. At the initial state, sediment is on average transported landward in the middle part of the estuary, but seaward in both the upper part and at the estuary mouth. The convergence of sediment transport caused by net seaward transport in the upper estuary and net landward transport in the middle estuary produces net accumulation between the two areas as a result of which the large bar is formed. Figure 6.10 shows that the net depositional area, and hence the

location of incipient bar formation, is situated between $x = 25$ and $x = 135$ km. At the final state, the whole estuary has a nearly constant seaward transport rate for sediment supplied by the river, which results in an almost zero accumulation rate as required by the equilibrium state.

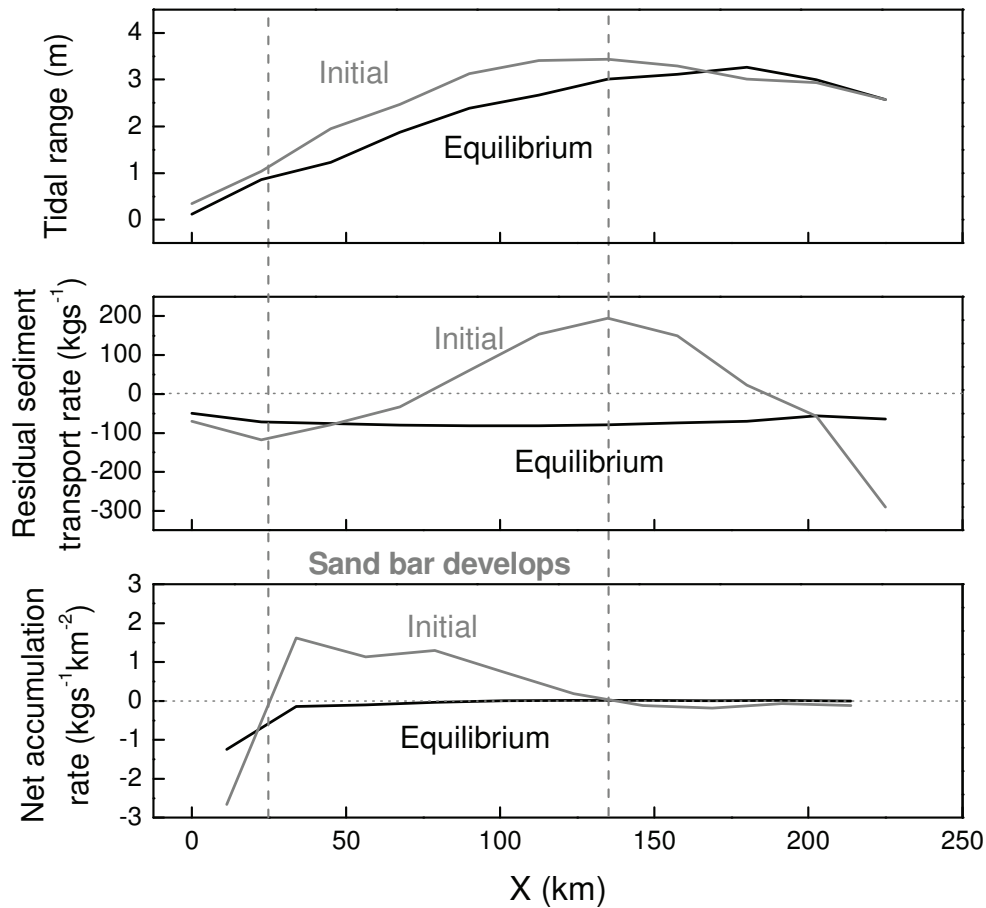


Fig. 6.10. Comparison between the initial and the final equilibrium states of case R: the longitudinal distributions of tidal range, cross-sectional residual sediment transport rate, and net accumulation rate, positive values denoting the flood direction or the net deposition, and negative values denoting the ebb direction or the net erosion. The net deposition area is located where the sand bar initially develops.

6.4.2. Sensitivity analysis

The influence of the estuarine convergence rate is demonstrated in Fig. 6.11. The widths of the reference case R and the test case S described by the eq. (6.1) and (6.2), respectively, are compared in the upper panel. Case S has a longer convergence length and hence a slower convergence rate, the modeled profile being associated with a smaller sand bar. The landward parts of the profiles are almost the same in both cases, whereas the head of the sand bar in case S is located around 20 km further landward. The crest has an elevation close to that of case R, but its position has shifted landward from $x = 130$ to $x = 90$ km. These results suggest that stronger convergence causes the sand bar to grow in the seaward direction. The 10 km increase in convergence length from case R to case S, as reflected in the reduced width distribution, causes a pronounced retreat of the sand bar head and crest. This documents the sensitive response of bar morphology to estuarine convergence.

The effect of sediment supply on the estuarine morphology is evaluated and illustrated in Fig. 6.12. Instead of using a single grain size of $64 \mu\text{m}$ (reference case R), test case G employs three size fractions of -1ϕ ($2000 \mu\text{m}$), 1ϕ ($500 \mu\text{m}$), and 3ϕ ($125 \mu\text{m}$). In the upper panel it can be seen how the initially mixed sediment (1ϕ) has become size-sorted longitudinally along the bar after 6,000 years. At the seaward end, bed armoring has taken place because the flood-dominated tidal currents have winnowed the fine fraction from the top layer. The armored bed has a mean size of 0ϕ ($1,000 \mu\text{m}$), being coarser than the largest grains that the currents can move. Due to the definition of the equilibrium sediment concentration at the boundary, the armored bed prevents further sediment import from the open sea, resulting in a starved sediment supply condition there. As a consequence, the lack of sediment produces a sand bar of reduced size. Compared with case R, the bar head is located 25 to 40 km further landward in case G, although the elevation of the bar crest is almost the same. As the finest sediment has accumulated around the point of sediment convergence, the sediment of the bar is finer than that in both the mouth area and the upper estuary.

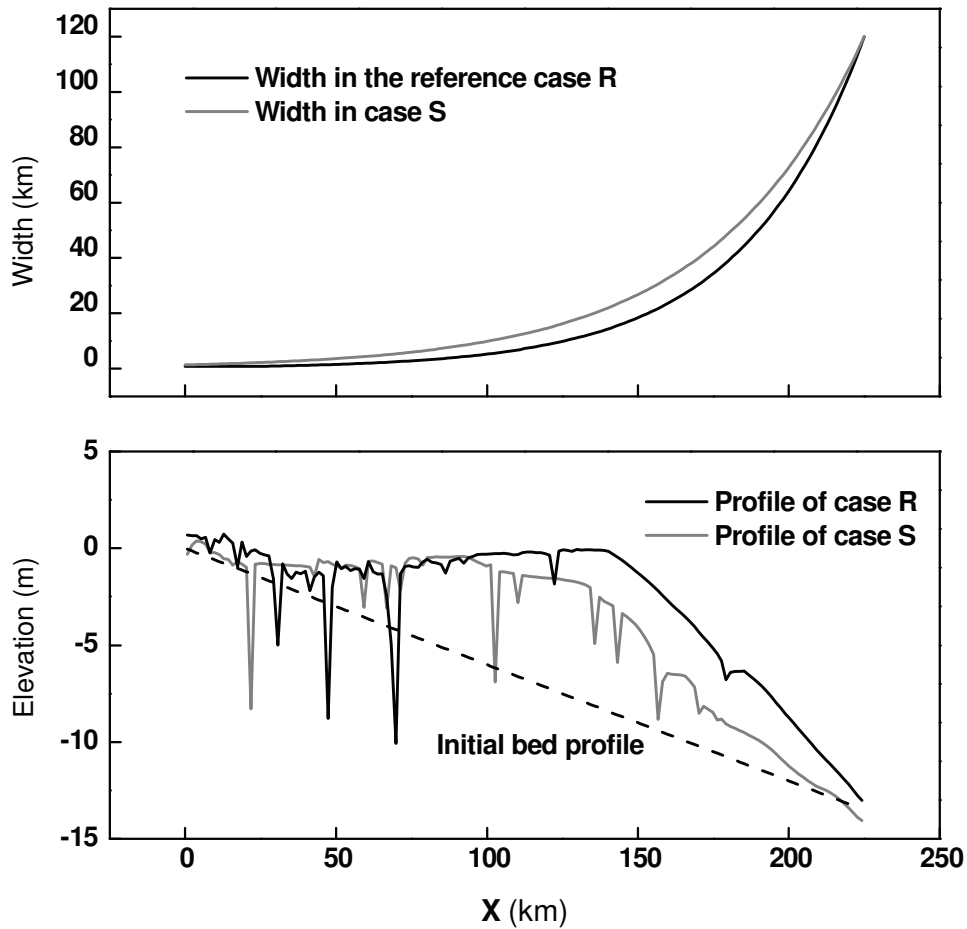


Fig. 6.11. Diagrams illustrating the effect of estuarine convergence. The upper panel shows the longitudinal distributions of the estuarine width, the lower panel the longitudinal bed profiles after the 6,000 year modeling period. Case R is the reference case and case S the test case (see Table 6.1 for details).

The results of the three test cases used to investigate the effect of river discharge are illustrated in Fig. 6.13. A twofold response of the longitudinal bed profiles to changing river discharge is observed. First, the bar head shifts seaward with increasing discharge. Second, with the exception of case R3 representing the largest discharge, lower discharge is associated with a higher elevation of the bar crest. It can also be seen that the crest elevations of case R1 and case R2 are above the mean sea level. Low discharge systems thus tend to have shorter but higher sand bars.

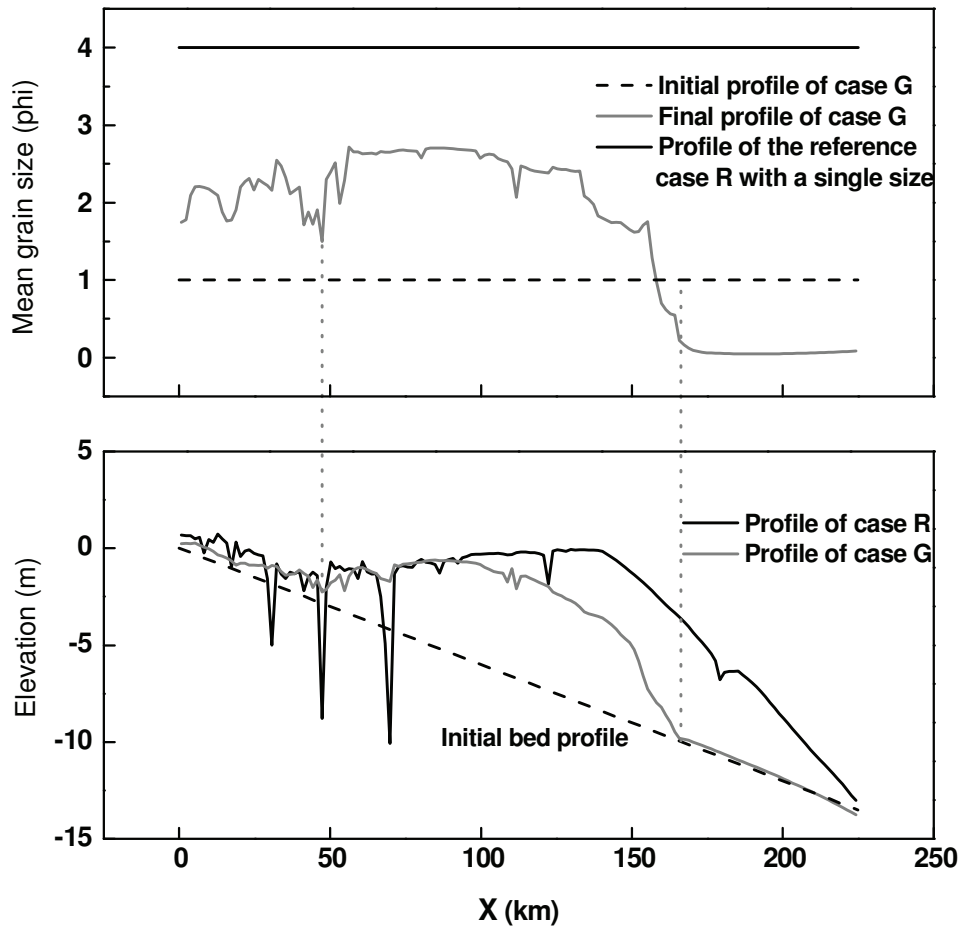


Fig. 6.12. Diagrams illustrating the effect of sediment supply. The upper panel shows the longitudinal distributions of the mean grain size, the lower panel the longitudinal bed profiles after the 6,000 year modeling period. The case R is the reference case, and case G the test case (see Table 6.1 for details).

6.5. Discussion

6.5.1. Comparison with the Qiangtangjiang Estuary

Comparing the modeling results with the modern QE reveals that the equilibrium large sand bar is successfully simulated by the numerical modeling, and that the shape, size and position of the modeled bar are reasonably similar to that of the modern QE, as can be seen by comparing Fig. 6.3 and Fig. 6.6. Both bars have the same front slope of 1.5×10^{-4} . The modeled bar begins at a position in the upper estuary close to

that of the observed one, but it extends 50 km further toward the mouth, resulting in a bar body having a total length of 175 km. The crest height of the modeled bar is 7.8 m above the initial bed compared with 10.4 m of the modern bar. The modeled bar has a flat top with the crest located further seaward in accordance with the larger bar body. Although there are some inconsistencies in detail, the overall similarity with the modern bar suggests that the schematized numerical model is able to reproduce the first-order characteristics of the large sand bar in the QE.

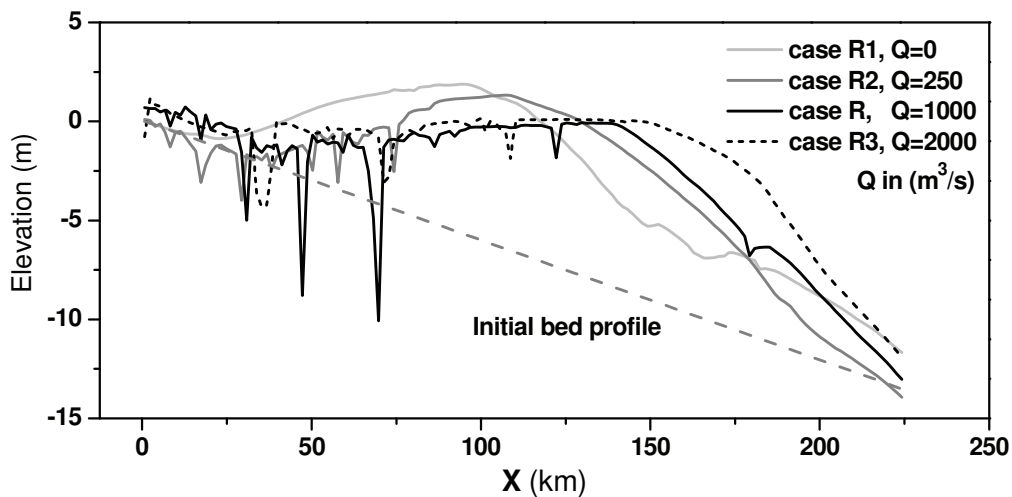


Fig. 6.13. Diagram illustrating the effect of river discharge. Case R is the reference case and cases R1, R2, and R3 are the test cases having river discharges (Q) of 0, 250, and 2,000 m^3/s , respectively (see Table 6.1 for details).

The lack of detailed information on the temporal evolution of the QE makes it currently impossible to fully verify the modeling results. The modeling results show that the basic feature of the large sand bar evolves within 1,000 years, which is consistent with the time period available for bar formation after the establishment of the funnel-shaped geometry of the QE (Chen et al., 1964). The seaward displacement of the bar crest, which was estimated on the basis of historical documents and sedimentological field data (Chen et al., 1964), is also predicted by the numerical modeling approach. Finally, the equilibrium bed profiles were obtained after about

3,000 years in both the observations and the modeling (Chien et al., 1964).

The net accumulation in the QE over the past several decades can be interpreted to be the result of estuarine geometry modifications induced by land reclamation activities. The sensitivity analysis shows that the growth of the sand bar is positively correlated with the degree of estuarine convergence (see Fig. 6.11b). The intensified land reclamation, especially in the upper part of the estuary, has resulted in stronger convergence (Han et al., 2003) and hence in renewed net accumulation and sand bar growth (Guo et al., 2009).

The differences between the observed and the modeled sand bar mainly concern the seaward extension of the bar head, a feature that can be explained by the simplified model settings. In terms of the sensitivity analysis, a reduced estuarine convergence rate should cause a pronounced retreat of the bar head (see Fig. 6.11b). Figure 6.3a shows that, in the mouth area, the measured longitudinal width has a much slower convergence rate than the schematized curve. Compared with the observed bed profile, the schematized modeling domain evidently allows the bar to become larger and to extend further seaward.

Another possible reason for the difference may be the presence of waves in the mouth region. Waves from the open sea will penetrate some distance into the estuary, although bed friction in shallow water will then rapidly dissipate the wave energy. The wide estuary mouth favors the initial growth of local wind waves. As a result, although tidal currents play the predominant role in sediment transport, wave action can not be entirely ignored in the mouth area (Dalrymple and Choi, 2007). Observed waves are on average 0.5 m high in the mouth and these may well interact with the tidal currents to prevent the seaward growth of the modern sand bar. In addition, the QE on average suffers three typhoon invasions every year (Guo et al., 2009). The associated strong wave activity may therefore induce intensive seabed erosion in the mouth area. Because the simplified model does not include wave processes, the modeled bar has a greater potential for seaward growth than the observed one.

6.5.2. Comparison with other numerical modeling results and other large funnel-shaped tide-dominated estuaries

The model case R1 can be compared with the 1D numerical model of Todeschini et al. (2008) because both have assumed zero river discharge. The modeled bed profiles in the two approaches show a high degree of similarity, in spite of the differences in the model dimensions and the initial bed profiles. Both sand bars have a crest elevation above the mean sea level and a concave-up front profile. Also the influence of convergence is identical in the two approaches, the strong degree of convergence producing a seaward extension of the large sand bars.

Three other large estuaries have been selected for comparison with the QE and the modeling results: the Cobequid Bay—Salmon River Estuary, Bay of Fundy, Canada, the Bristol Channel—Severn Estuary, UK, and the Gulf of Kachchh, India (Fig 14). All three share the same characteristics with the QE in that the domain is large (the length scale of 10^2 km), funnel-shaped, and tide-dominated.

The Cobequid Bay—Salmon River Estuary is located at the head of the eastern arm of the Bay of Fundy (Fig. 6.14a) and is associated with a limited river input (annual average discharge being approximately $10 \text{ m}^3 \text{ s}^{-1}$). It consists of four morphological zones between the seaward and landward tidal limits: zone 0 — the non-depositional subtidal floor of the Minas Basin and outer Cobequid Bay; zone 1 — tidal sand-bar complex; zone 2 — upper-flow-regime sand flats; zone 3 — the tidally influenced fluvial channel (Dalrymple et al., 1990). The spatial grain-size distribution is illustrated in Fig. 6.14a and Fig. 6.15. The outer part of the estuary is occupied by an armoring layer of coarse lag deposits that protect the underlying finer sediment from erosion, the winnowed material having been transported into the estuary to form the sand-bar complex and sand flats (Amos, 1978; Dalrymple et al., 1990). The estuary has a seaward-fining trend in the inner fluvial-dominated part, and a landward-fining trend in the seaward part as a result of which the finest grain sizes are found on the sand-bar complex and sand flats (Fig. 6.15).

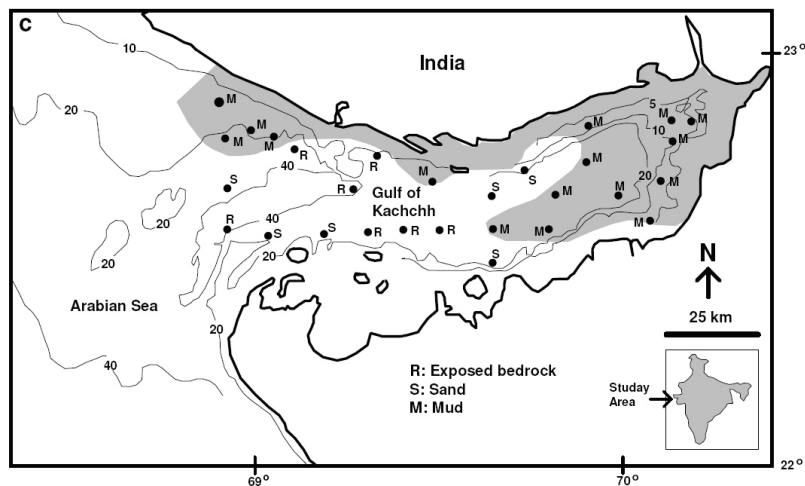
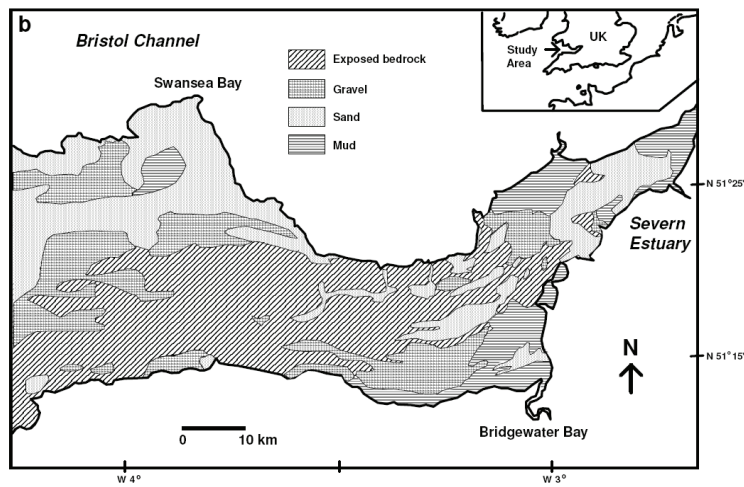
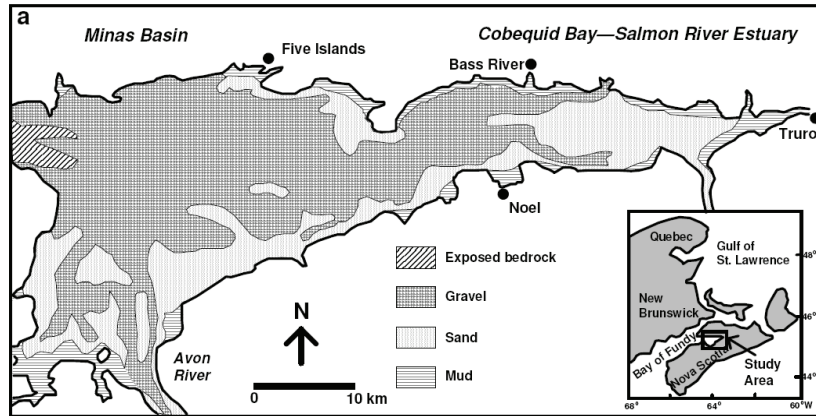


Fig. 6.14. (a) Distribution of surficial sediment types in the Cobequid Bay—Salmon River Estuary, Bay of Fundy, Canada (after Dalrymple et al., 1990). (b) Distribution of surficial sediment types in the Bristol Channel—Severn Estuary, UK (after Harris, 1988). (c) Distribution of surficial sediment types and bathymetry in the Gulf of Kachchh, India, the mud bed being highlighted by shadowing (after Kunte et al., 2005; Ramaswamy et al., 2007).

Compared with the QE, the Cobequid Bay—Salmon River Estuary differs in two respects. First, the sand bar and sand flats are located more landward. Second, the longitudinal coarse-fine-coarse trend of the surficial sediments and the armoring layer in the outer estuary. Both of them can be qualitatively interpreted by the results of the sensitivity analysis. The effect of river discharge illustrated in Fig. 6.13 shows that low river input causes a landward displacement of the large sand bar, while the limited sediment supply in case G leads to a retreat of the bar head (Fig. 6.12). The low river discharge ($10 \text{ m}^3 \text{ s}^{-1}$) and the limited sediment supply, which is associated with armoring in the outer part, prevent a seaward growth of the sand bar and sand flats. The spatial grain-size variations are due to the tidal sorting processes. The landward net transport winnows fine grains from the active surface layer, leaving behind the armoring lag deposits, the fine sediment accumulating in the upper part of the estuary to form the bulge in the longitudinal bed profile. The sensitivity analysis on the effect of sediment supply clearly reveals the importance of these processes, and the modeled grain-size profile of case G in Fig. 6.12 reasonably resembles the observed coarse-fine-coarse trend in Fig. 6.15.

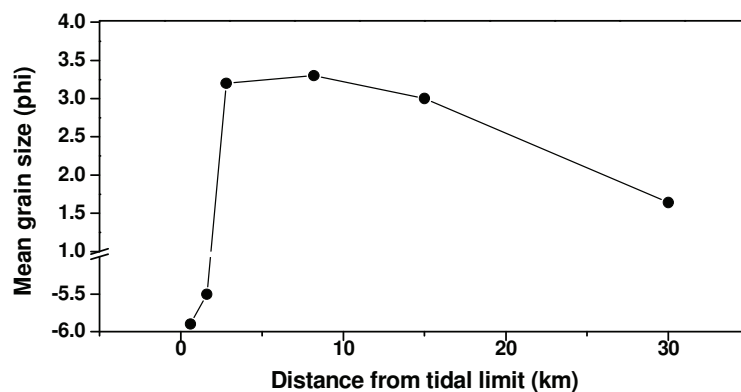


Fig. 6.15. The longitudinal mean grain-size distribution in the Cobequid Bay—Salmon River Estuary, Bay of Fundy, Canada (modified from Dalrymple and Choi, 2007).

The Bristol Channel—Severn Estuary is the largest estuary on the west coast of England (Fig. 6.14b). The main part of the Bristol Channel is scoured clear of bed sediments to expose the underlying bedrock or is covered by lag gravels (Harris, 1988). Sandy and muddy materials are deposited in the Severn Estuary and at the heads of smaller bays in the Bristol Channel, including Swansea Bay and Bridgewater Bay. Although the Severn is the longest river in Britain, its annual average discharge is only $107 \text{ m}^3 \text{ s}^{-1}$, being less than that of the Qiangtangjiang River by one order of magnitude. Allen (1991) suggested that the sand in the Severn Estuary originated from the Bristol Channel, and that the mud has a fluvial source. The sand accumulation in the Severn Estuary and sediment starvation in the Bristol Channel can be explained by the same reasoning as in the case of the Cobequid Bay—Salmon River Estuary: namely the combined effects of river discharge and sediment supply.

The Gulf of Kachchh, in turn, is a large coastal embayment along the northwest coast of India (Fig. 6.14c). Because of the semi-arid climate, river discharge is very small. The Indus River, one of the major rivers of the world, is located about 150 km to the northwest. The bathymetric map shows that, in the head part of the bay, the distance between the 20 m and 10 m contours is smaller than that between the 10 m and 5 m contours, implying a bar-shaped bulge in the longitudinal bed profile. Muddy sediments occur in a tie adjacent to the northern coastline and the bay head, the most probable source being the Indus River (Chauhan et al., 2006; Ramaswamy et al., 2007). The central and the southern parts of the bay are covered by sand or exposed bedrock, and a rough sequence of rock-sand-mud can be identified towards the bay head. Contrary to the Changjiang Estuary located close to the QE, the remote source of the Indus River can not provide sufficient sediment to form a large bar at the head and in the central part of the Gulf of Kachchh because of the relatively large distance between the bay and the Indus River. The small local river discharge, in turn, causes the bar to be located further headward in the Gulf of Kachchh, as intimated by the bathymetry in Fig. 6.13.

6.5.3. The unique position of the Qiangtangjiang Estuary within the general framework of estuarine morphology

In general, bottom friction induces flood-dominated tidal currents, causing a net landward sediment transport. In the upper parts of estuaries, river discharge pushes sediment seaward due to small channel cross-sectional areas and tidal prisms. The two converging transport processes meet at some point in the middle estuary, creating a bar along the longitudinal bed profile as a consequence. The new morphology then causes feedbacks to the hydrodynamics, which lead to a progressive decrease in tidal distortion (Lanzoni and Seminara, 2002). As a result, the point of sediment transport convergence gradually moves in the seaward direction. Eventually, the sediment supplied by the river begins to bypass the estuary and further import of sediment from the adjacent sea is blocked. Once net deposition and erosion are balanced, an equilibrium bed profile is established. Previous numerical modeling studies have established equilibrium morphological configurations without the contribution of water and sediment from the river (Lanzoni and Seminara, 2002; Hibma et al, 2003b; Todeschini et al., 2008). The present results indicate that estuaries are not always transient geomorphological features but that, in some cases, longterm interactions between fluvial and marine processes can keep an estuary in an equilibrium state, preventing it from being infilled by river-borne sediment to evolve into a delta.

The bars scale with the different forcing factors in the estuaries. The sensitivity analysis and the comparison with other estuaries demonstrate the importance of estuarine convergence, sediment supply and river discharge. Strong convergence causes the growth of the bars by seaward extension, while coarser sediments and reduced sediment supply cause the bar head to retreat landward, restricting it to the upper section of the estuary. While the position of the bar head extends seaward under large river discharge, the elevation of the bar crest is negatively correlated with river discharge. It can thus be expected that, with increasing freshwater discharge in the future, the equilibrium morphology will eventually change from estuarine to deltaic.

In this context, the QE is a unique example. The strong degree of the convergence, which can be measured by the convergence length of 40 km, a sufficient cohesionless fine sediment supply from the adjacent Changjiang River, and a river discharge of around $1000 \text{ m}^3 \text{ s}^{-1}$, have shaped a large sand bar with a total length of 125 km and a crest height of 10 m above the estuarine baseline. Variations of these forcing factors can modify the estuarine morphology, and the responding trends can be predicted by sensitivity analysis. For example, the recent accumulation of sediment is related to the enhanced convergence of the estuarine geometry caused by land reclamation. Furthermore, the decline in sediment flux from the Changjiang River, which has been reported by Yang et al. (2006), and possible variations in the Qiangtangjiang river discharge due to global climate change may influence the dynamics of the large sand bar in the QE in the future.

In the generalized morphological model of tide-dominated estuaries recently suggested by Dalrymple and Choi (2007) (Fig. 6.16), the schematic estuarine geometry is characterized by a funnel shape, elongate tidal sand bars in the seaward section, fringing muddy tidal flats and salt marshes, and straight-meandering-straight transitions in the channel pattern. It is important to note here that the elongate tidal bars (also called tidal ridges) representing a series of bedforms identified in estuarine cross-sections are fundamentally different from the large bar of the present study, which merely forms a pronounced bulge in the longitudinal bed profile. In fact, the elongate tidal bar area in the model of Dalrymple and Choi (2007) would be the front part of the large sand bar. Because of the seaward declining river current, significant wave action in the mouth area and the hypersynchronous mode of the tidal wave, the total energy profile between the landward limits of tidal influence and the seaward mouth has a high-low-high-low trend. The net landward sediment transport in the outer marine-dominated section and the net seaward transport in the upper river-dominated section result in bedload convergence in the middle section where a tightly meandering channel develops.

In spite of apparent differences, the fundamental morphological and hydrodynamic characteristics of the Dalrymple and Choi (2007) model are nevertheless comparable to the numerical modeling results presented here. The limited number of lateral grid cells prevents the development of lateral channel-ridge patterns in the model, although the estuarine bathymetry in Fig. 6.5b does show some reasonable similarity with the schematic morphological map in Fig. 6.16. The longitudinal distribution river and tidal currents, and the high-low-high-low trend of the total energy in Fig. 6.16 are consistent with the numerical results in Fig. 6.8 and Fig. 6.9, even though waves were not involved in the present numerical modeling study.

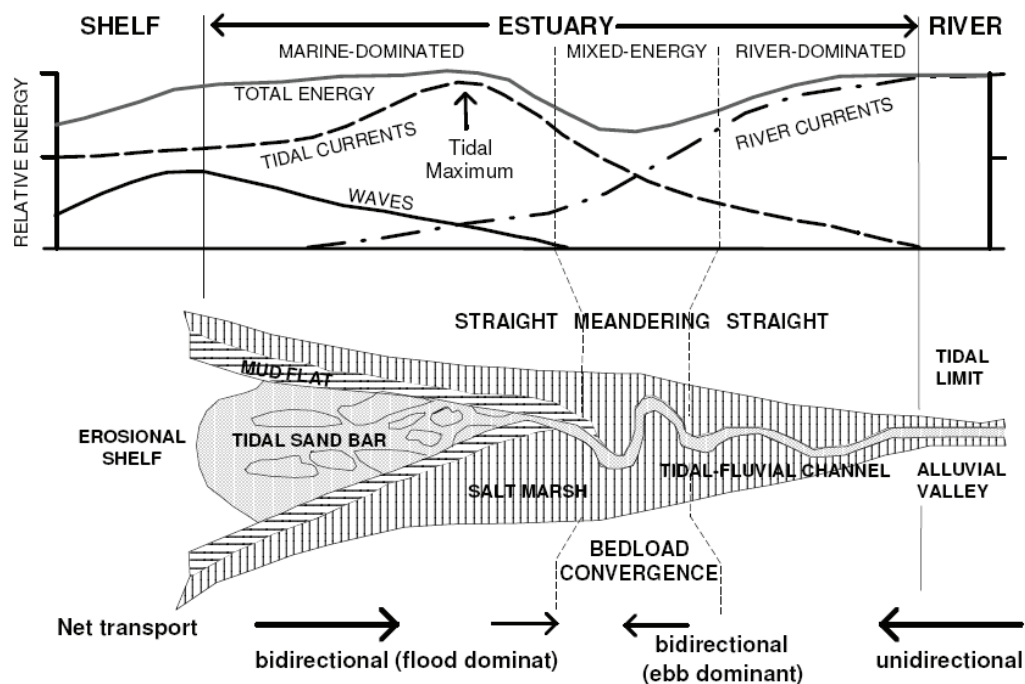


Fig. 6.16. Schematic geomorphological map of a tide-dominated estuary and the longitudinal variations in the intensity of the three main physical processes of river currents, tidal currents and wave action. The resulting directions of net bedload sediment transport are indicated by the arrows at the bottom. (after Dalrymple and Choi, 2007).

Comparing the QE morphology with the Dalrymple and Choi (2007) model, most of the features are similar, including the tidal sand ridge system and the fringing muddy

tidal flats (Fig. 6.2), only the straight-meandering-straight transitions of the channel pattern being an exception. Instead of the meandering channel, the fluvial to marine transition zone of the QE is characterized by a laterally migrating channel thalweg. This difference can be explained by the cohesionless character of the sediment in the QE. Sustainable channel meandering needs some form of bank stabilization (Chien, 1985). In this context, experimental studies have shown that the strength of the elevated bank, which can be provided by cohesive sediment and/or vegetation, is crucial for the development of meandering channels (Schumm and Khan, 1972; Peakall et al., 2007; Braudrick et al., 2009; Tal and Paola, 2010). The lack of cohesive sediment and vegetation in the QE thus prevents the development of a meandering channel and, instead, favors the formation of the lateral channel migration pattern (Chien, 1985).

6.6. Conclusions

It has been demonstrated that the evolution and the development of an equilibrium state of the large sand bar in the QE can be simulated by a 2DH numerical modeling approach. The basic feature of the large sand bar appears 1,000 years after formation of the modern estuarine plan geometry in the middle estuary where the net landward sediment transport caused by the flood-dominated tide meets the net seaward sediment transport induced by the prevailing river discharge. Feedbacks of the newly developing morphology to the hydrodynamics then reduce the tidal distortion, which results in a decreasing rate of sediment convergence. The sand bar gradually grows until 2,000 years later the net seaward transport occupies the whole estuary and the river supplied sediment bypasses the estuary to the sea. From this time onward, the bar morphology gradually approaches an equilibrium state.

It has also been demonstrated that three major forcing factors play an important role in estuarine morphology. A strong degree of convergence causes the growth of the bar by seaward extension of the bar head, whereas coarser sediment and a reduced

sediment supply cause the bar head to retreat landward, bar development being then restricted to the upper section of the estuary. The position of the bar head also shifts seaward with increasing river discharge, although the elevation of the bar crest is negatively correlated with river discharge. The strong degree of convergence, a sufficient supply of cohesionless fine sediment from the adjacent Changjiang River, and a river discharge of around $1000 \text{ m}^3 \text{ s}^{-1}$ thus control the shape of the unique large sand bar in the QE.

7. Concluding Remarks and Perspectives

7.1. Tide-induced suspended sediment transport

The tide-induced behavior of suspended sediment transport has been studied by individually solving the 1D vertical suspended sediment advection-diffusivity equation and the 1D depth-averaged suspended sediment transport equation. The solutions provide a good understanding of two aspects of the problem, namely that (1) the phase lag increases linearly with height above the bed, whereas the amplitude of the SSC variation decreases exponentially with height; and that (2) the relative contributions of local resuspension and advection to depth-averaged suspended sediment concentration can be determined and that the empirical decomposition terms of horizontal residual fluxes of suspended sediment have clear physical explanations.

However, beyond the first step of the 1D model, the 2D behavior of suspended sediment transport could be investigated in a second step. The combination of 1D vertical and 1D horizontal processes would help to understand the contribution of shear diffusion on suspended sediment transport caused by the nonlinear interaction of turbulence and advection in different water layers (e.g., Burchard and Baumert, 1998; Stanev et al., 2007). Another important potential improvement would be the involvement of vertical stratification effects induced by vertical density differences in suppressing the turbulence and then the suspended sediment diffusion (e.g., Geyer, 1993; Wang et al., 2005).

7.2. Tide-induced equilibrium morphology

The morphological modeling of back-barrier tidal basins in the Wadden Sea shows that, in equilibrium states, (1) the dimensional parameters of channel area and volume are proportional to the 1.5 power of the basin area and tidal prism, respectively, whereas the dimensionless parameters of relative channel area and the ratio between

channel volume and tidal prism are both proportional to the square root of basin area. The values of the coefficients before the power in these relations are of the order of 10^{-5} , and (2) large basin areas and low tidal ranges favor strong concave-up hypsometries, whereas small basin areas and high tidal ranges favor less concave-up hypsometries, which have been interpreted as a response to the relative area of intertidal areas or channels in the tidal basins.

However, the model only employed the tidal force. Although the tidal current is considered to be the major factor in controlling tidal basin morphology, wave action has also been suggested to play a substantial role (Friedrichs and Aubrey, 1996; Fagherazzi et al., 2006, 2007). The inclusion of wave contributions could therefore provide more realistic insights into the morphological evolution of barrier islands and their protected tidal basins. This topic is particularly important against the background of sea-level rise resulting from global warming (Flemming and Bartholomä, 1997).

The long-term (6,000 years) modeling results of the large funnel-shaped tide-dominated estuarine morphology shows the development of a sand bar that reached equilibrium within about 3,000 years as the leading order characteristics of the estuarine bed. Its general shape, size and position is consistent with historical observations in the Qiangtangjiang Estuary, China. A series of sensitivity analyses suggests that the estuarine convergence rate, sediment supply, and river discharge are the main controlling factors of sand bar formation.

However, due to the limited number of lateral grid cells, the detailed lateral morphological features characterizing the generalized estuarine morphological model of Dalrymple and Choi (2007), e.g., the channel and ridge systems, could not be reproduced in the present case. A more challenging future objective would therefore be to model the formation of channel patterns in the upper parts of estuaries, e.g., the laterally migrating channel thalweg in the Qiangtangjiang Estuary, or the meandering channel in the Salmon River Estuary, Canada.

In summary, no amount of modeling can produce a final picture because of the complexity of earth surface systems. This is nicely reflected in the anecdote that when H. A. Einstein told his famous father that he would like to investigate sediment transport, Albert Einstein tore his hair and asked his son ironically: can it not be something more complicated? This dissertation is hopefully only the first step in a long and challenging march into a more enlightened future.

References

- Allen, G.P., Salomon, J.C., Bassoullet, P., Du Penhoat, Y., De Grandpre, C. 1980. Effects of tides on mixing and suspended sediment transport in macrotidal estuaries. *Sedimentological Geology* 26, 69–90.
- Allen, J.R.L., 1974. Reaction, relaxation and lag in natural sedimentary systems: General principles, examples and lessons. *Earth-Science Reviews* 10, 263–342.
- Allen, J.R.L., 1990. The Severn Estuary in southwest Britain: its retreat under marine transgression, and fine-sediment regime. *Sedimentary Geology* 66, 13–28.
- Allen, J.R.L., 1991. Fine sediment and its sources, Severn Estuary and inner Bristol Channel, southwest Britain. *Sedimentary Geology* 75, 57–65.
- Allen, J.R.L., 2000. Morphodynamics of Holocene salt marshes: A review sketch from the Atlantic and southern North Sea coasts of Europe. *Quaternary Science Review* 19, 1155–1231.
- Amos, C.L., 1978. The post glacial evolution of the Minas Basin, N.S.: a sedimentological interpretation. *Journal of Sedimentary Petrology* 48, 965–982.
- Amos, C.L., Daborn, G.R., Christian, H.A., Atkinson, A., Robertson, A., 1992. In situ measurements on fine-grained sediments from the Bay of Fundy. *Marine Geology* 108, 175–196.
- Amos, C.L., Villatoro, M., Helsby, R., Thompson, C.E.L., Zaggia, L., Umgieser, G., Venturini, V., Are, D., Sutherland, T.F., Mazzoldi, A., Rizzetto, F., 2010. The measurements of sand transport in two inlets of Venice lagoon; towards understanding the estuarine budget. *Estuarine Coastal and Shelf Science* 87, 225–236.
- Anthony, E.J., Gardel, B., Gratiot, N., Proisy, C., Allison, M.A., Dolique, F., Fromard, F., 2010. The Amazon-influenced muddy coast of South America: A review of mud-bank-shoreline interactions. *Earth-Science Reviews* 103, 99–121.
- Bartholdy J., Aagard, T., 2001. Storm surge effects on a back-barrier tidal flat of the Danish Wadden Sea. *Geo-Marine Letters* 20, 113–141.
- Bartholdy, J., 1985. Dynamic interpretation of grain size relations in silt. *Geo-Marine Letters* 5, 67–70.
- Bartholomä, A., Kubicki, A., Badewien, T.H., Flemming, B.W., 2009. Suspended sediment transport in the German Wadden Sea – seasonal variations and extreme events. *Ocean Dynamics* 59, 213–225.
- Barua, D.K., Kuehl, S.A., Miller, R.L. and Moore, W.S., 1994. Suspended sediment distribution and residual transport in the coastal ocean off the Ganges-Brahmaputra river mouth. *Marine Geology* 120, 41–61.
- Bass, S.J., Aldridge, J.N., McCave, I.N., Vincent, C.E., 2002. Phase relationships between fine sediment suspensions and tidal currents in coastal seas. *Journal of Geophysical Research*

107(C10), 3146, doi: 10.1029/2001JC001269.

- Bhattacharya, J.P., 2003. Deltas and estuaries. In: Middleton, G.V. (Eds.), *Encyclopedia of Sediments and Sedimentary Rocks*, Kluwer, Dordrecht, pp. 195–203.
- Boon, J.D., 1975. Tidal discharge asymmetry in a salt marsh drainage system. *Limnology and Oceanography* 20, 71–80.
- Boon, J.D., Byrne, R.J., 1981. On basin hypsometry and the morphodynamic response of coastal inlet systems. *Marine Geology* 40, 27–48.
- Braudrick, C.A., Dietrich, W.E., Leverich, G.T. Sklar, L.S. 2009. Experimental evidence for the conditions necessary to sustain meandering in coarse-bedded rivers. *Proceedings of the National Academy of Sciences of the United States of America* 106, 16,936–41.
- Brenon, I., Le Hir, P., 1999. Modelling the turbidity maximum in the Seine Estuary (France): Identification of formation processes. *Estuarine, Coastal and Shelf Science* 49, 525–544.
- Bruun, P., 1978. *Stability of Tidal Inlets*. Elsevier, New York, 510 pp.
- Cayocca, F., 2001. Long-term morphological modeling of a tidal inlet: the Arcachon Basin, France. *Coastal Engineering* 42, 115–142.
- Chang, T.S., Flemming, B.W., Bartholomä, A., 2007. Distinction between sortable silts and aggregated particles in muddy intertidal sediments of the East Frisian Wadden Sea, southern North Sea. *Sedimentary Geology* 202, 453–463.
- Chauhan, O.S., Jayakumar, S., Menezes, A.A.A., Rajawat, A.S., Nayak, S.R., 2006. Anomalous inland influx of the River Indus, Gulf of Kachchh, India. *Marine Geology* 229, 91–100.
- Chen, J., Luo, Z., Chen, D., Xu, H., Qiao P., 1964. The forming and historical evolvement of the big sand bar inside the Qiantangjiang Estuary. *Acta Geographica Sinica* 30, 109–123 (in Chinese with Russian abstract).
- Chen, Z., Stanley, D.J., 1998. Sea-Level Rise on Eastern China's Yangtze Delta. *Journal of Coastal Research* 14, 360–366.
- Cheng, P., Wilson, R.E., 2008. Modeling sediment suspensions in an idealized tidal embayment: importance of tidal asymmetry and settling lag. *Estuaries and Coasts* 31, 828–842.
- Chien, N., 1985. On the classification and causes of formation of different channel patterns. *Acta Geographica Sinica* 40, 1–10 (in Chinese with English abstract).
- Chien, N., Sie, H., Chow, C., Lee, Q., 1964. The fluvial processes of the big sand bar inside the Chien Tang Chiang Estuary. *Acta Geographica Sinica* 30, 124–142 (in Chinese with English abstract).
- Cohen, S., Willgoose, G., Hancock, G., 2008. A methodology for calculating the spatial distribution of the area-slope equation and the hypsometric integral within a catchment. *Journal of Geophysical Research* 113, F03027, doi: 10.1029/2007JF000820.
- Dade, W.B., Friend, P.F., 1998. Grain-size, sediment-transport regime, and channel slope in

- alluvial rivers. *Journal of Geology* 106, 661–675.
- D'Alpaos, A., Lanzoni, S., Marani, M., Rinaldo, A., 2010. On the tidal prism–channel area relations. *Journal of Geophysical Research* 115, F01003, doi: 10.1029/2008JF001243.
- Dalrymple, R.W., Knight, R.J., Zaitlin, B.A., Middleton, G.V., 1990. Dynamics and facies model of a macrotidal sand-bar complex, Cobequid Bay—Salmon River Estuary (Bay of Fundy). *Sedimentology* 37, 577–612.
- Dalrymple, R.W., Zaitlin, B.A., Boyd, R., 1992. Estuarine facies models: conceptual basis and stratigraphic implications. *Journal of Sedimentary Petrology* 62, 1130–1146.
- Dastgheib, A., Roelvink, J.A., Wang, Z.B., 2008. Long-term process-based morphological modeling of the Marsdiep Tidal Basin. *Marine Geology* 256, 90–100.
- Davies, A.G., 1977. A mathematical model of sediment in suspension in a uniform reversing tidal flow. *Geophysical Journal of the Royal Astronomical Society* 51, 503–529.
- Davies, J.L., 1964. A morphogenetic approach to the world shorelines. *Zeitschrift für Geomorphologie* 8, 127–142.
- Davis Jr., R.A., Flemming, B.W., 1991. Time-series study of mesoscale tidal bedforms, Martens Plate, Wadden Sea, Germany. In: Smith, D.G., Reinson, G.E., Zaitlin, B.A., Rahmani, R.A. (Eds.), *Clastic Tidal Sedimentology*. Canadian Society of Petroleum Geologists Memoir, vol. 16, pp. 275–282.
- de Swart, H.E., Zimmerman, J.T.F., 2009. Morphodynamics of Tidal Inlet Systems. *Annual Review of Fluid Mechanics* 41, 203–229.
- Dieckmann, R., 1985. Geomorphologie, Stabilitäts- und Langzeitverhalten von Watteinzugsgebieten der Deutschen Bucht, Mitt. Franzius-Institut, Univ. Hannover, Heft 60, pp. 133–361.
- Dieckmann, R., Osterthun, M., Partenscky, H.-W., 1987. Influence of water-level elevation and tidal range on the sedimentation in a German tidal flat area. *Progress in Oceanography* 18, 151–166.
- Dissanayake, D.M.P.K., Roelvink, J.A., van der Wegen, M., 2009. Modelled channel patterns in a schematized tidal inlet. *Coastal Engineering* 56, 1069–1083.
- Dodds, P.S., Rothman, D.H., 2000. Scaling, universality, and geomorphology. *Annual Review of Earth and Planetary Sciences* 28, 571–610.
- Dou, S., ca. 762-779. On ocean tide. (in Chinese).
- Drake, D.E., Cacchione, D.A., 1989. Estimates of the suspended sediment reference concentration (C_a) and resuspension coefficient (γ_0) from near-bed observations on the California shelf. *Continental Shelf Research* 9, 51–64.
- Dronkers J. 1986. Tide-induced residual transport of fine sediment. In: *Physics of shallow bays and estuaries*, Miami 1984. Springer Verlag, p. 228–244.

- Dronkers, J., 1998. Morphodynamics of the Dutch Delta. In: Dronkers, J., Scheffers, M.B.A.M. (Ed.), *Physics of Estuaries and Coastal Seas*. A.A. Balkema, Rotterdam, Netherlands, pp. 297-304.
- Dronkers, J., 2005. *Dynamics of Coastal Systems*. Advanced Series on Ocean Engineering, vol. 25, World Scientific, Singapore, 520 pp.
- Dyer, K.R., 1974. The salt balance in stratified estuaries. *Estuarine and Coastal Marine Science* 2, 273–281.
- Dyer, K.R., 1986. *Coastal and estuarine sediment dynamics*. John Wiley and Sons, Chichester, 342p.
- Dyer, K.R., 1995. Sediment transport processes in estuaries. In: Perillo, G.M.E. (Ed.), *Geomorphology and Sedimentology of Estuaries*. Developments in Sedimentology 53, 2nd Edition. Elsevier Science, Amsterdam, pp. 423–449.
- Dyer, K.R., 1997. *Estuaries—Physical Introduction*, 2nd ed. John Wiley and Sons, Chichester, 195 pp.
- ECCHE (Editorial Committee for Chinese Harbors and Embayments), 1992. *Chinese Harbours and Embayments (Part V)*. China Ocean Press, Beijing, 357 pp (in Chinese).
- ECICTZ (Editorial Committee for Comprehensive Investigation of Coastal Zone and Tidal flat Resources, Zhejiang Province), 1988. *Comprehensive Investigation of Coastal Zone and Tidal flat Resources, Zhejiang Province*. China Ocean Press, Beijing, 485pp (in Chinese).
- Edmonds, D.A., Slingerland, R.L., 2010. Significant effect of sediment cohesion on delta morphology. *Nature Geosciences* 3, 105–109.
- Ehlers, J., 1988. *The morphodynamics of the Wadden Sea*. A. A. Balkema Publ., Rotterdam, 397 pp.
- Eiser, W.C., Kjerfve, B., 1986. Marsh topography and hypsometric characteristics of a South Carolina salt marsh basin. *Estuarine, Coastal and Shelf Science* 23, 595–605.
- Ellis, K.M., Bowers, D.G., Jones, S.E., 2004. A study of the temporal variability in particle size in a high-energy regime. *Estuarine, Coastal and Shelf Science* 61, 311–315.
- Emery, K.O., 1979. Hypsometry of the continental shelf off eastern North America. *Estuarine, Coastal and Shelf Science* 9, 653–658.
- Eysink, W.D., 1990. Morphologic response of tidal basins to changes. Proc. 22nd Coastal Engineering Conference, ASCE, Delft, Vol. 2, the Dutch coast, paper no. 8, pp. 1948–1961.
- Eysink, W.D., 1993. ISOS*2 Project: Impact of sea level rise on the morphology of the Wadden Sea within the scope of its ecological function, phase 4. Delft Hydraulic report H1300. Delft, The Netherlands, 95 pp.
- Fagherazzi, S., Carniello, L., D’Alpaos, L., Defina, A., 2006. Critical bifurcation of shallow microtidal landforms in tidal flats and salt marshes. *Proceedings of the National Academy*

of Sciences of the United States of America 103, 8337-8341.

- Fagherazzi, S., Palermo, C., Rulli, M.C., Carniello, L., Defina, A., 2007. Wind waves in shallow microtidal basins and the dynamic equilibrium of tidal flats. *Journal of Geophysical Research* 112, F02024, doi: 10.1029/2006JF000572.
- Feng, Y., Li, Y., Xie, Q., Zhang, L., 1990. The geomorphic features and interfacial activities in Hangzhou Bay. *Acta Oceanologica Sinica* 12, 213–223 (in Chinese).
- Fischer, H. B., 1976. Mixing and dispersion in estuaries. *Annual Review of Fluid Mechanics* 8:107–133.
- FitzGerald, D.M., Fenster, M.S., Argow, B.A., Buynevich, I.V., 2008. Coastal impacts due to sea-level rise. *Annual Review of Earth and Planetary Sciences* 36, 601–647.
- Flemming, B.W., Bartholomä, A., 1997. Response of the Wadden Sea to a rising sea level: a predictive empirical model. *German Journal of Hydrography* 49, 343-353.
- Flemming, B.W., Davis Jr., R.A., 1994. Holocene evolution, morphodynamics and sedimentology of the Spiekeroog barrier island system (southern North Sea). *Senckenbergiana maritima* 24, 117–155.
- Flemming, B.W., Nyandwi, N., 1994. Land reclamation as a cause of fine-grained sediment depletion in backbarrier tidal flats (southern North Sea). *Netherlands Journal of Aquatic Ecology* 28, 299–307.
- Flemming, B.W., Schubert, H., Hertweck, G., Müller, K., 1992. Bioclastic tidal-channel lag deposits: a genetic model. *Senckenbergiana Maritima* 22, 109–129.
- Flemming, B.W., Ziegler, K., 1995. High-resolution grain size distribution patterns and textural trends in the backbarrier tidal flats of Spiekeroog Island (southern North Sea). *Senckenbergiana maritima* 26, 1–24.
- Fortunato, A.B., Oliveira, A., 2004. A modeling system for tidally driven long-term morphodynamics. *Journal of Hydraulic Research* 42, 426–434.
- Friedrichs, C.T., 1995. Stability shear stress and equilibrium cross-sectional geometry of sheltered tidal channels. *Journal of Coastal Research* 11, 1062–1074.
- Friedrichs, C.T., Aubrey, D.G., 1988. Non-linear tidal distortion in shallow well mixed estuaries: A synthesis. *Estuarine, Coastal and Shelf Science* 27, 521–545.
- Friedrichs, C.T., Aubrey, D.G., 1996. Uniform bottom shear stress and equilibrium hypsometry of intertidal flats. In: Pattiaratchi, C. (Eds), *Mixing in Estuaries and Coastal Seas*, Coastal and Estuarine Stud., vol. 50, AGU, Washington, D. C., pp. 405–429.
- Galloway, W.E., 1975. Process framework for describing the morphologic and stratigraphic evolution of deltaic depositional systems. In: Broussard, M.L. (Ed.), *Deltas, Models for Exploration*. Houston Geological Society, Houston, pp. 87–98.
- Ganju, N.K., Schoellhamer, D.H., Bergamaschi, B.A., 2005. Suspended sediment fluxes in a tidal wetland: controlling factors, and error analysis. *Estuaries* 28, 812–822.

- Ganju, N.K., Schoellhamer, D.H., Jaffe, B.E., 2009. Hindcasting of decadal-timescale estuarine bathymetric change with a tidal-timescale model. *Journal of Geophysical Research* 114, F04019, doi: 10.1029/2008JF001191.
- Gao S., 2008. Morphodynamic processes of tidal inlets: a review. *Advances in Earth Science*, 23, 1237–1248 (in Chinese with English abstract).
- Gao, S., 2005. Modeling the growth limit of the Changjiang Delta. *Geomorphology* 85, 225–236.
- Gao, S., Collins, M.B., 1994. Tidal inlet equilibrium in relation to cross-sectional area and sediment transport patterns. *Estuarine, Coastal and Shelf Science* 38, 157–172.
- Geleynse, N., Storms, J. E. A., Stive, M.J.F., Jagers, H.R.A., Walstra, D.J.R., 2010. Modeling of a mixed-load fluvio-deltaic system. *Geophysical Research Letters* 37, L05402, doi: 10.1029/2009GL042000.
- Geyer, W.R., 1993. The importance of suppression of turbulence by stratification on the estuarine turbidity maximum. *Estuaries* 16, 113–125.
- Gordon, C.M., 1975. Sediment entrainment and suspension in a turbulent tidal flow. *Marine Geology* 18:M57–M64.
- Groen, P., 1967. On the residual transport of suspended matter by an alternating tidal current. *Netherlands Journal of Sea Research* 3-4, 564–574.
- Guezennec, L., Lafite, R., Dupont, J.-P., Meyer, R., Boust, D., 1999. Hydrodynamics of suspended particulate matter in the tidal freshwater zone of a macrotidal estuary (the Seine Estuary, France). *Estuaries* 22, 717–727.
- Guillou, N., Chapalain, G., Thais, L., 2009. Three-dimensional modeling of tide-induced suspended transport of seabed multicomponent sediments in the eastern English Channel. *Journal of Geophysical Research* 114, C07025, doi:10.1029/2008JC004791.
- Guo, Y., Zhang, J., Zhang, L., Shen Y., 2009. Computational investigation of typhoon-induced storm surge in Hangzhou Bay, China. *Estuarine, Coastal and Shelf Science* 85, 530–536.
- Hack, J. T., 1957. Studies of longitudinal stream profiles in Virginia and Maryland. U.S. Geology Survey Professional Paper, 294B, 45–97.
- Hamblin, P., 1989. Observations and model of sediment transport near the turbidity maximum of the upper Saint Lawrence Estuary. *Journal of Geophysical Research* 94(C10), 14419–14428.
- Han, Z.C., Dai, Z.H, Li, G.B., 2003. Regulation and Exploitation of Qiantang River Estuary. China Water Publication, Beijing, 554pp (in Chinese with an English abstract).
- Harris, P.T., 1988. Large scale bedforms as indicators of mutually evasive sand transport and the sequential infilling of wide-mouthed estuaries. *Sedimentary Geology* 57, 273–298.
- Harris, P.T., Collins, M.B., 1985. Bedform distributions and sediment transport paths in the Bristol Channel and Severn Estuary, U.K. *Marine Geology* 62, 153–166.

- Henderson, F.M., 1966. *Open Channel Flow*, New York, Macmillan, 522 pp.
- Hibma, A., De Vriend, H.J., Stive, M.J.F., 2003a. Numerical modelling of shoal pattern formation in well-mixed elongated estuaries. *Estuarine, Coastal and Shelf Science* 57, 981–991.
- Hibma, A., Schuttelaars, H.M., Wang, Z.B., 2003b. Comparison of longitudinal equilibrium profiles of estuaries in idealized and process-based models. *Ocean Dynamics* 53, 252–269.
- Hill, P.S., McCave, I.N., 2001. Suspended particle transport in benthic boundary layers. In: Boudreau, B.P. and Jorgensen, B.B. (Ed.), *The Benthic Boundary Layer: Transport Processes and Biogeochemistry*. Oxford Univ. Press, New York, pp. 78–103.
- Hill, P.S., Nowell, A.R.M., Jumars, P.A., 1988. Flume evaluation of the relationship between suspended sediment concentration and excess boundary shear stress. *Journal of Geophysical Research* 93, 12499–12509.
- Hofstede, J., 2002. Morphologic responses of Wadden Sea tidal basins to a rise in tidal water levels and tidal range. *Zeitschrift für Geomorphologie* 46, 93–108.
- Hoitink, A.J.F., Hoekstra, P., van Maren, D.S., 2003. Flow asymmetry associated with astronomical tides: Implications for the residual transport of sediment. *Journal of Geophysical Research* 108(C10), 3315, doi: 10.1029/2002JC001539.
- Holdaway, G.P., Thorne, P.D., Flatt, D., Jones, S.E., Prandle, D., 1999. Comparison between ADCP and transmissometer measurements of suspended sediment concentration. *Continental Shelf Research* 19, 421–441.
- Hood, W.G., 2007. Scaling tidal channel geometry with marsh island area: A tool for habitat restoration, linked to channel formation process. *Water Resources Research* 43, W03409, doi:10.1029/2006WR005083.
- Hori, K., Saito, Y., Zhao, Q., Cheng, C., Wang, P., Sato, Y., Li, C., 2001. Sedimentary facies of the tide-dominated paleo-Changjiang (Yangtze) estuary during the last transgression. *Marine Geology* 177, 331–351.
- Hurtrez, J.-E., Sol, C., Lucazeau, F., 1999. Effect of drainage area on hypsometry from an analysis of small-scale drainage basins in the Siwalik Hills (central Nepal). *Earth Surface Processes Landforms* 24, 799–808.
- IPCC (2007), *Climate change 2007: the physical science basis, summary for policymakers*, Contrib.Work. Group I Fourth Assess. Rep. Intergov. Panel Climate Change, Cambridge, UK.
- Jago, C.F., Jones, S.E., 1998. Observation and modelling of the dynamics of benthic fluff resuspended from a sandy bed in the southern North Sea. *Continental Shelf Research* 18, 1255–1282.
- Jago, C.F., Jones, S.E., Sykes, P., Rippeth, T., 2006. Temporal variation of suspended particulate matter and turbulence in a high energy, tide-stirred, coastal sea: Relative contributions of

- resuspension and disaggregation. *Continental Shelf Research* 26, 2019–2028.
- Jansen, J.D., Codilean, A.T., Bishop, P. and Hoey, T.B., 2010. Scale dependence of lithological control on topography: bedrock channel geometry and catchment morphometry in Western Scotland. *Journal of Geology* 118, 223–246.
- Jay, D.A., Geyer, W.R., Uncles, R.J., Vallino, J., Largier, J., Boynton, W.R., 1997. A review of recent developments in estuarine scalar flux estimation. *Estuaries* 20, 262–280.
- Joseph, J., 1954. Die Sinkstoffführung von Gezeitenströmen als Austauschproblem. *Arch Met Geophys Bioklin (A)* 7, 482–501.
- Jung, K.T., Jin, J.Y., Kang, H.-W., Lee, H.J., 2004. An analytical solution for the local suspended sediment concentration profile in tidal sea region. *Estuarine Coastal and Shelf Science* 61, 657–667.
- Kirby, R., 2000. Practical implications of tidal flat shape. *Continental Shelf Research* 20, 1061–1077.
- Kostaschuk, R.A., Luternauer, J.L., Church, M.A., 1989. Suspended sediment hysteresis in a salt-wedge estuary, Fraser River, Canada. *Marine Geology* 87, 273–285.
- Krivtsov, V., Gascoigne, J., Jones, S.E., 2008. Harmonic analysis of suspended particulate matter in the Menai Strait (UK). *Ecological Modelling* 21, 53–67.
- Krögel, F., Flemming, B.W., 1998. Evidence for temperature-adjusted sediment distributions in the back-barrier tidal flats of the Frisian Wadden sea (southern North Sea). In: Alexander, C.R., Davis, R.A., Henry, V.J. (Eds), *Tidalites: Processes and Products*, SEPM Special Publication No. 61, 31–41.
- Kunte, P.D., Zhao, C., Osawa, T., Sugimori, Y., 2005. Sediment distribution study in the Gulf of Kachchh, India, from 3D hydrodynamic model simulation and satellite data. *Journal of Marine Systems* 55, 139–153.
- Lanzoni, S., Seminara, G., 2002. Long-term evolution and morphodynamic equilibrium of tidal channels. *Journal of Geophysical Research* 107(C1), 3001, doi: 10.1029/2000JC000468.
- Latteux, B., 1995. Techniques for long-term morphological simulation under tidal action. *Marine Geology* 126, 129–141.
- Lavelle, J.W., Mofjeld, H.O., Barker, E.T., 1984. An in situ erosion rate for a fine-grained marine system. *Journal of Geophysical Research* 89 (C), 6543–6552.
- Lawrence, D.S.L., Allen, J.R.L., Havelock, G.M., 2004. Salt marsh morphodynamics: an investigation of tidal flows and marsh channel equilibrium. *Journal of Coastal Research* 20, 301–316.
- Le Hir, P., Ficht, A., Jacinto, R.S., Lesueur, P., Dupont, J.-P., Lafite, R., Brenon, I., Thouvenin, B., Cugier, P., 2001. Fine sediment transport and accumulations at the mouth of the Seine Estuary (France). *Estuaries* 24, 950–963.
- Lee, H.J., Chu, Y. S., Park, Y.A., 1999. Sedimentary processes of fine-grained material and the

- effect of seawall construction in the Daeho macrotidal flat–nearshore area, northern west coast of Korea. *Marine Geology* 157, 171–184.
- Lesser, G.R., Roelvink, J.A., van Kester, J.A.T.M., Stelling, G.S., 2004. Development and validation of a three-dimensional morphological model. *Coastal Engineering* 51, 883–915.
- Lettman K.A., Wolff, J-O., Badewien, T.H., 2009. Modeling the impact of wind and waves on suspended particulate matter fluxes in the East Frisian Wadden Sea (southern North Sea). *Ocean Dynamics* 59, 239–262.
- Li, J., Chen, Z., 1998. Sediment resuspension and implications for turbidity maximum in the Changjiang Estuary. *Marine Geology* 148, 117–124.
- Lin, C.-M., Zhuo, H.-C., Gao, S., 2005. Sedimentary facies and evolution in the Qiantang River incised valley, eastern China. *Marine Geology* 219, 235–259.
- Mackin, J.H., 1948. Concept of the graded river. *Geological Society of America Bulletin* 59, 463–512.
- Mai, S., Bartholomä, A., 2000. The missing mud flats of the Wadden Sea: a reconstruction of sediments and accommodation space lost in the wake of land reclamation. In Flemming, B.W., Delafontaine, M.T., Liebezeit, G. (Eds), *Muddy coast dynamics and resource management*. Elsevier Science, Amsterdam, pp. 257–272.
- Mao, H., Gan, Z., Shen, H., 1964. A preliminary study of the tidal flushing in Hangchow bay (I) Upper estuary. *Oceanologia et Limnologia Sinica* 6, 121–133 (in Chinese with an English abstract).
- Marani, M., Belluco, E., D’Alpaos, A., Defina, A., Lanzoni, S., Rinaldo, A., 2003. On the drainage density of tidal networks, *Water Resources Research* 39, 1040, doi: 10.1029/2001WR001051.
- Marciano, R., Wang, Z.B., Hibma, A., de Vriend, H.J., Defina, A., 2005. Modeling of channel patterns in short tidal basins. *Journal of Geophysical Research* 110, F01001, doi: 10.1029/2003JF000092.
- Masek, J.G., Isacks, B.L., Gubbels, T.L., Fielding, E.J., 1994. Erosion and tectonics at the margins of continental plateaus. *Journal of Geophysical Research* 99, 13,941-13,956, doi: 10.1029/94JB00461.
- McCave, I.N., Hall, I.R., 2006. Size sorting in marine muds: Processes, pitfalls, and prospects for paleoflow-speed proxies. *Geochemistry Geophysics Geosystem* 7, Q10N05, doi:10.1029/2006GC001284.
- Miller, M.C., McCave, I.N., Komar, P.D., 1977. Threshold of sediment motion under unidirectional currents. *Sedimentology* 24, 507–527.
- Montano, Y., Carbajal, N., 2008. Numerical experiments on the long-term morphodynamics of the Colorado River Delta. *Ocean Dynamics* 58, 19–29.
- Moore, R.D., Wolf, J., Souza, A.J., Flint, S.S., 2009. Morphological evolution of the Dee

- Estuary, Eastern Irish Sea, UK: A tidal asymmetry approach. *Geomorphology* 103, 588–596.
- Murphy, S., Voulgaris, G., 2006. Identifying the role of tides, rainfall and seasonality in marsh sedimentation using long-term suspended sediment concentration data. *Marine Geology* 227:31–50
- Novakowski, K.I., Torres, R., Gardner, L.R., Voulgaris, G., 2004. Geomorphic analysis of tidal creek networks. *Water Resources Research* 40, W05401, doi: 10.1029/2003WR002722.
- Nyandwi, N., Flemming, B.W., 1995. A hydraulic model for the shore-normal energy gradient in the East Frisian Wadden Sea (southern North Sea), *Senckenbergiana maritima* 25,163–171.
- O'Brien, M.P., 1969. Equilibrium flow areas of inlets in sandy coasts. *Journal of the Waterways, Harbors, and Coastal Engineering Division: proceedings of the American Society of Civil Engineers* 95, 43–52.
- Oertel, G.F., 2001. Hypsographic, hydro-hypsographic and hydrological analysis of coastal bay environments, Great Machipongo Bay, Virginia. *Journal of Coastal Research* 17, 775–783.
- Oost, A.P., Davis Jr., P.L., 1994. Sedimentology and development of barrier islands, ebb-tidal deltas, inlets and backbarrier areas of the Dutch Wadden Sea. *Senckenbergiana maritima*, 24, 65–115.
- Orton, G.J., Reading, H.G., 1993. Variability of deltaic processes in terms of sediment supply, with particular emphasis on grain size. *Sedimentology* 40, 475–512.
- Pan, C., Huang, W., 2010. Numerical modeling of suspended sediment transport in Qiantang River: an estuary affected by tidal bore. *Journal of Coastal Research* 26, 1123–1132.
- Paola, C., 2011. Simplicity versus complexity. *Nature* 469, 38–39.
- Parry, M.L., Canziani, O.F., Palutikof, J.P., van der Linden, P.J., Hanson, C.E. (eds.) Contribution of Working Group II to the Fourth Assessment Report of the Intergovernmental Panel on Climate Change. Cambridge University Press, Cambridge.
- Peakall, J., Ashworth, P., Best, J. 2007. Meander-bend evolution, alluvial architecture, and the role of cohesion in sinuous river channels: a flume study. *Journal of Sedimentary Research* 77, 197–212.
- Perez-Pena, J.V., Azanon, J.M., Booth-Rea, G., Azor, A., Delgado, J., 2009. Differentiating geology and tectonics using a spatial autocorrelation technique for the hypsometric integral. *Journal of Geophysical Research* 114 F02018, doi:10.1029/2008JF001092.
- Perillo, G.M.E., 1995. Definitions and geomorphologic classifications of estuaries. In: Perillo, G.M.E. (Ed.), *Geomorphology and Sedimentology of Estuaries*. Developments in Sedimentology 53, 2nd Edition. Elsevier Science, Amsterdam, pp. 17–47.
- Pernetta, J., 1994. *Atlas of the Oceans*. Octopus Publ. Group, London, 207 pp.
- Pino Q, M., Perillo, G.M.E., Santamarina, P., 1994. Residual fluxed in a cross-section of the

- Valdivia River Estuary, Chile. *Estuarine, Coastal and Shelf Science* 38, 491–505.
- Pliny the Elder, ca. 45 AD. *Historia naturalis*.
- Postma, H., 1961. Transport and accumulation of suspended matter in the Dutch Wadden Sea. *Netherlands Journal of Sea Research* 1, 148–190.
- Prandle, D., 1997. Tidal characteristics of suspended sediment concentrations. *Journal of Hydraulic Engineering* 123, 341–350.
- Prandle, D., 2004. How tides and river flows determine estuarine bathymetries. *Progress of Oceanography* 61, 1–26.
- Pritchard, D., 2005. Suspended sediment transport along an idealised tidal embayment: settling lag, residual transport and the interpretation of tidal signals. *Ocean Dynamics* 55, 124–136.
- Pritchard, D., Hogg, A.J., 2003. Cross-shore sediment transport and the equilibrium morphology of mudflats under tidal currents. *Journal of Geophysical Research* 108(C10), 3313, doi: 10.1029/2002JC001570.
- Pritchard, D., Hogg, A.J., Roberts, W., 2002. Morphological modelling of intertidal mudflats, the role of cross-shore tidal currents. *Continental Shelf Research* 22, 1887–1895.
- Ramaswamy, V., Nagender Nath, B., Vethamony, P., Illangovan, D., 2007. Source and dispersal of suspended sediment in the macro-tidal Gulf of Kachchh. *Marine Pollution Bulletin* 54, 708–719.
- Reed, C., Niedoroda, A.W., Swift, D.J.P., 1999. Modeling sediment entrainment and transport processes limited by bed armouring. *Marine Geology*, 154, 143–154.
- Reise, K., 2001. *Ecological Comparison of Sedimentary Shores*. Heidelberg, Berlin, Springer-Verlag, 384 pp.
- Renger, E., Partenscky, H.-W., 1974. Stabilitätsverhalten von Wattenzugsgebieten. *Die Küste* 25, 73–86.
- Rinaldo, A., Belluco, E., D'Alpaos, A., Feola, A., Lanzoni, S., Marani, A., 2004. Tidal networks: form and function. In Fagherazzi, S., Marani, A., Blum L.K. (Eds), *The Ecogeomorphology of Tidal Marshes*. American Geophysical Union, Washington, D.C., pp. 75–91.
- Roberts, W., Le Hir, P., Whitehouse, R.J.S., 2000. Investigation using simple mathematical models of the effect of tidal currents and waves on the profile shape of intertidal mudflats. *Continental Shelf Research* 20, 1079–1097.
- Roelvink, J.A., 2006. Coastal morphodynamic evolution techniques. *Coastal Engineering* 53, 177–187.
- Rouse, H., 1937. Modern conceptions of the mechanics of fluid turbulence. *Transactions American Society of Civil Engineers* 102:436–505

- Sanderson, B.G., Coade, G., 2010. Scaling the potential for eutrophication and ecosystem state in lagoons. *Environmental Modelling & Software* 25, 724-736.
- Sanford, L.P., Halka, J.P., 1993. Assessing the paradigm of mutually exclusive erosion and deposition of mud, with examples from upper Chesapeake Bay. *Marine Geology* 114, 37–57.
- Sanford, L.P., Maa, J.P.-Y., 2001. A unified erosion formulation for fine sediments. *Marine Geology* 179, 9–23.
- Schubel, J.R., 1968. Turbidity maximum of the northern Chesapeake Bay. *Science* 161, 1013–1015.
- Schumm, S.A., Khan, H.R., 1972. Experimental Study of Channel Patterns. *Geological Society of America Bulletin* 83, 1755–1770.
- Schuttelaars, H.M., de Swart, H.E., 2000. Multiple morphodynamic equilibrium in tidal embayment. *Journal of Geophysical Research* 105, 24105–24118.
- Simpson, J.H., Rippeth, T.P., Campbell, A.R., 2000. The phase lag of turbulent dissipation in tidal flow. In: Yanagi, T. (Eds), *Interactions between estuaries, coastal Seas and shelf Seas*. Terrapublish, Tokyo, pp 57–67
- Smith, J.D., 1977. Modeling of sediment transport on continental shelves. In: Goldberg ED, McCave IN, O'Brien JJ, Steele JH (Eds), *The Sea. Marine Modeling*, vol. 6. John Wiley and Sons, New York, pp 539–577.
- Smith, J.D., McLean, S.R., 1977. Spatially averaged flow over a wavy surface. *Journal of Geophysical Research* 82, 1735–1746.
- Soulsby, R.L., 1997. *Dynamics of marine sands*. Thomas Telford, Oxford, 249pp.
- Souza, A.J., Alvarez, L.G., Dickey, T.D., 2004. Tidally induced turbulence and suspended sediment. *Geophysical Research Letters* 31, L20309, doi: 10.1029/2004GL021186
- Stanev, E.V, Brink-Spalink, G., Wolff, J.-O., 2007. Sediment dynamics in tidally dominated environments controlled by transport and turbulence: A case study for the East Frisian Wadden Sea. *Journal of Geophysical Research* 112, C04018, doi: 10.1029/2005JC003045.
- Stanley, D.J., Warne, A.G., 1994. Worldwide initiation of Holocene marine deltas by deceleration of sea level rise. *Science* 265, 228–231.
- Sternberg, R.W., Larsen, L.H., Miao, Y.T., 1985. Tidally driven sediment transport on the East China Sea continental. *Continental Shelf Research* 4, 105–120.
- Strahler, A.N., 1952. Hypsometric (area-altitude) analysis of erosional topography. *Geological Society of America Bulletin* 63, 1117–1142.
- Straub, K.M., Jerolmack, D.J., Mohrig, D., Rothman, D.H., 2007. Channel network scaling laws in submarine basins. *Geophysical Research Letters* 34, L12613, doi: 10.1029/2007GL030089.

- Su J., Wang, K., 1989. Changjiang river plume and suspended sediment transport in Hangzhou Bay. *Continental Shelf Research* 9, 93–111.
- Swift, D.J.P., Thorne, J.A., 1991. Sedimentation on continental margins: I. A general model for shelf sedimentation. In: Swift, D.J.P., Tillman, R.W., Oertel, G.F., Thorne, J.A. (Eds.), *Shelf Sand and Sandstone Bodies, Geometry, Facies and Sequence Stratigraphy: International Association of Sedimentologists Special Publication*, vol. 14, pp. 3–31.
- Tal, M., Paola, C., 2010. Effects of vegetation on channel morphodynamics: results and insights from laboratory experiments. *Earth Surface Processes and Landforms*, 35, 1014–1028.
- Temmerman, S., Bouma, T.J., Govers, G., Wang, Z.B., De Vries, M.B., Herman, P.M.J., 2005. Impact of vegetation on flow routing and sedimentation patterns: Three-dimensional modeling for a tidal marsh. *Journal of Geophysical Research* 110, F04019, doi: 10.1029/2005JF000301.
- Thwaites, F.T., Williams, A.J., 2001. BASS measurements of currents, waves, stress, and turbulence in the North Sea bottom-boundary layer. *IEEE Journal of Oceanic Engineering* 26, 161–170.
- Tian, T., Merico, A., Su, J., Staneva, J., Wiltshire, K., Wirtz, K., 2009. Importance of resuspended sediment dynamics for the phytoplankton spring bloom in a coastal marine ecosystem. *Journal of Sea Research* 62, 214–228.
- Todeschini, I., Toffolon, M., Tubino, M., 2008. Long-term morphological evolution of funnel-shape tide-dominated estuaries. *Journal of Geophysical Research* 113, C05005, doi: 10.1029/2007JC004094.
- Toffolon, M., Crosato, A., 2007. Developing macroscale indicators for estuarine morphology: The case of the Scheldt estuary. *Journal of Coastal Research* 23, 195–212.
- Tonnon, P.K., van Rijn, L.C., Walstra, D.J.R., 2007. The morphodynamic modelling of tidal sand waves on the shoreface. *Coastal Engineering* 54, 279–296.
- Uncles, R.J., Elliott, R.C.A., Weston, S.A., 1985a. Dispersion of salt and suspended sediment in a partly mixed estuary. *Estuaries* 8, 256–269.
- Uncles, R.J., Elliott, R.C.A., Weston, S.A., 1985b. Observed fluxes of water, salt and suspended sediment in a partly mixed estuary. *Estuarine, Coastal and Shelf Science* 20, 147–167.
- Uncles, R.J., Stephens, J.A., 1989. Distributions of suspended sediment at high water in a macrotidal estuary. *Journal of Geophysical Research* 94, 14395–14405.
- Uncles, R.J., Stephens, J.A., 1993. Nature of the turbidity maximum in the Tamar Estuary, UK. *Estuarine, Coastal and Shelf Science* 36, 413–431.
- van de Kreeke, J., Day, C.M., Mulder, H.P.J., 1997. Tidal variations in suspended sediment concentration in the Ems estuary: origin and resulting sediment flux. *Journal of Sea Research* 38, 1–16.
- van de Kreeke, J., Hibma, A., 2005. Observations on silt and sand transport in the throat section

- of the Frisian Inlet. *Coastal Engineering* 52, 159–175.
- van de Kreeke, J., Robaczewska, K., 1993. Tide-induced residual transport of coarse sediment; application to the Ems estuary. *Netherlands Journal of Sea Research* 31, 209–220.
- van der Ham, R., Winterwerp, J.C., 2001. Turbulent exchange of fine sediments in a tidal channel in the Ems/Dollard estuary. Part II. Analysis with a 1DV numerical model. *Continental Shelf Research* 21, 1629–647.
- van der Molen, J., Bolding, K., Greenwood, N., Mills, D.K., 2009. A 1-D vertical multiple grain size model of suspended particulate matter in combined currents and waves in shelf seas. *Journal of Geophysical Research* 114, F01030, doi:10.1029/2008JF001150.
- van der Wegen, M., Dastgheib, A., Roelvink, J.A., 2010. Morphodynamic modeling of tidal channel evolution in comparison to empirical PA relationship. *Coastal Engineering* 57, 827–837.
- van der Wegen, M., Roelvink, J.A., 2008. Long-term morphodynamic evolution of a tidal embayment using a two-dimensional, process-based model. *Journal of Geophysical Research* 113, C03016, doi: 10.1029/2006JC003983.
- van der Wegen, M., Wang, Z.B., Savenije, H.H.G., Roelvink, J.A., 2008. Long-term morphodynamic evolution and energy dissipation in a coastal plain tidal embayment. *Journal of Geophysical Research* 113, F03001, doi: 10.1029/2007JF000898.
- van Dongeren, A.R., de Vriend, H.J., 1994. A model of morphological behavior of tidal basins. *Coastal Engineering* 22, 287–310.
- van Goor, M.A., Zitman, T.J., Wang, Z.B., Stive, M.J.F., 2003. Impact of rising sea level on the morphologic equilibrium state of tidal inlets. *Marine Geology* 202, 211–227.
- van Ledden, M., Wang, Z.B., Winterwerp, H., de Vriend, H., 2004. Sand-mud morphodynamics in a short tidal basin. *Ocean Dynamics* 54, 385–391.
- van Maren, D.S., Hoekstra, P., Hoitink, A.J.F., 2004. Tidal flow asymmetry in the diurnal regime: bed-load transport and morphologic changes around the Red River Delta. *Ocean Dynamics* 54, 424–434.
- van Straaten, L.M.J.U., Kuenen, P.H., 1958. Tidal action as a cause of clay accumulation. *Journal of Sedimentary Petrology* 28, 406–413.
- Velegrakis, A.F., Gao, S., Lafite, R., Dupont, J.P., Huault, M.F., Nash, L.A., Collins, M.B., 1997. Resuspension and advection processes affecting suspended particulate matter concentrations in the central English Channel. *Journal of Sea Research* 38, 17–34.
- Walcott, R.C., Summerfield, M.A., 2008. Scale dependence of hypsometric integrals: An analysis of southeast African basins. *Geomorphology*, 96, 174–186.
- Wang, X.H., Byun, D.S., Wang, X.L., Cho, Y.K., 2005. Modelling tidal currents in a sediment stratified idealized estuary. *Continental Shelf Research* 25, 655–665.
- Wang, Z.B., Jeuken, M.C.J.L., Gerritsen, H., de Vriend, H.J., Kornman, B.A., 2002.

- Morphology and asymmetry of the vertical tide in the Westerschelde estuary. *Continental Shelf Research* 22, 2599–2609.
- Wang, Z.B., Louters, T., de Vriend, H.J., 1995. Morphodynamic modeling of a tidal inlet in the Wadden Sea. *Marine Geology* 126, 289–300.
- Weeks, A.R., Simpson, J.H., Bowers, D.B., 1993. The relationship between concentrations of suspended particulate material and tidal processes in the Irish Sea. *Continental Shelf Research* 13, 1325–1334.
- Wells, J.T., 1995. Tide-dominated estuaries and tidal rivers. In: Perillo, G.M.E. (Ed.), *Geomorphology and Sedimentology of Estuaries. Developments in Sedimentology* 53, 2nd Edition. Elsevier Science, Amsterdam, pp. 179–205.
- West, J.R., Sangodoyin, A.Y.A., 1991. Depth-mean tidal current and sediment concentration relationships in three partially mixed estuaries. *Estuarine Coastal and Shelf Science* 32:141–159
- Whitehouse, R., 1995. Observations of the boundary layer characteristics and the suspension of sand at a tidal site. *Continental Shelf Research* 15, 1549–1567.
- Whitehouse, R., Soulsby, R., Roberts, W., Mitchener, H., 2000. *Dynamics of estuarine mud*. Thomas Telford, London, 210pp.
- Wiberg, P.L., Drake, D.E., Cacchione, D.A., 1994. Sediment suspension and bed armouring during high bottom stress events on the northern California inner continental shelf: measurements and predictions. *Continental Shelf Research* 14, 1191–1219.
- Willgoose, G., Hancock, G., 1998. Revisiting the hypsometric curve as an indicator of form and process in transport-limited catchment. *Earth Surface Processes and Landforms* 23, 611–623.
- Williams, P.B., Orr, M.K., Garrity, N.J., 2002. Hydraulic geometry: A geomorphic design tool for tidal marsh channel evolution in wetland restoration projects. *Restoration Ecology* 10, 577–590.
- Wu, J.-X., Shen, H.-T., Xiao, C.-Y., 2001. Sediment classification and estimation of suspended sediment fluxes in the Changjiang Estuary, China. *Water Resources Research* 37, 1969–1979.
- Xie, D., Wang, Z.B., Gao, S., de Vriend, H.J., 2009. Modeling the tidal channel morphodynamics in a macro-tidal embayment, Hangzhou Bay, China. *Continental Shelf Research* 29, 1757–1767.
- Xin, F., Wang, Y., Gao, J., Zou, X., 2010. Seasonal distributions of the concentrations of suspended sediment along Jiangsu Coastal Sea. *Oceanologica et Limnologia Sinica* 41, 459–468 (in Chinese with English abstract).
- Yang, Z., Hamrick, J.M., 2003. Variational inverse parameter estimation in a cohesive sediment transport model: An adjoint approach. *Journal of Geophysical Research* 108(C2), 3055, doi:10.1029/2002JC001423.

- Yang, Z., Wang, H., Saito, Y., Milliman, J.D., Xu, K., Qiao, S., Shi, G., 2006. Dam impacts on the Changjiang (Yangtze) River sediment discharge to the sea: The past 55 years and after the Three Gorges Dam. *Water Resources Research* 42, W04407, doi:10.1029/2005WR003970.
- You, Z.J., 2005. Estimation of bed roughness from mean velocities measured at two levels near the seabed. *Continental Shelf Research* 25, 1043–1051.
- Yu, Q., Flemming, B.W., Gao, S., 2011. Tide-induced vertical suspended sediment concentration profiles: phase lag and amplitude attenuation. *Ocean Dynamics* 61, 403–410.
- Zhou, X., Gao, S., 2004. Spatial variability and representation of seabed sediment grain sizes: An example from the Zhoushan - Jinshanwei transect, Hangzhou Bay, China. *Chinese Science Bulletin* 49, 2503–2507.
- Zimmerman, J.T.F., 1973. The influence of the subaqueous profile on wave-induced bottom stress. *Netherlands Journal of Sea Research* 6, 542–549.